In vivo Magnetic Resonance investigation of molecular diffusion and internal gradient coefficient to assess osteoporosis status in spongy bone

A thesis presented

by

Mauro Rebuzzi

to

The Interdepartmental Research Centre for Models and Information Analysis in Biomedical Systems

in fulfillment of the requirements for the degree of Doctor of Philosophy

in the subject of Biophysics

c. 685573

Thesis advisors   PhD Coordinator

Dr. Silvia Capuani   **Prof. Alfredo Colosimo**

Prof. Bruno Maraviglia

January 2011

Dedicated to my family.

Contents

Introduction

Osteoporosis is a highly diffuse disease that typically affects elderly individuals. It is a metabolic and systemic skeletal disease characterized by low bone mineral density (BMD), micro-architectural deterioration of the bone tissue and by an increase in bone porosity, leading to bone fragility and increased susceptibility to fracture. In recent years, substantial progress has been made in the identification, prevention, and treatment of osteoporosis, primarily with the aim of reducing fractures, the main cause of osteoporosis-related morbidity.

The World Health Organization suggests to use dual energy x-ray absorptiometry (DXA) to provide a quantitative definition of osteoporosis [1]. As a consequence it is the most widely used method of BMD assessment. The loss of bone mineral in the human skeleton, due to metabolic changes, affects primarily the micro-architectural structure of spongy bone. For this reason investigations on skeletal sites with high trabecular content such as spine, proximal femur and calcaneus are recommended for early diagnosis of osteoporosis. Although DXA examination is cheap, it is known to have a limited sensitivity. Quantitative computed tomography, or QCT, is a more accurate technique because it measures the true volumetric density, rather than providing an area-adjusted result as does DXA. As a consequence, QCT may be useful in assessing response to therapy in the cancellous bone and in the prediction of fracture risk. However, it involves appreciable radiation exposure, making QCT less suitable for regular treatment monitoring particularly in young patients, and deterring normal control subjects from participating in clinical trials. Nevertheless, only a poor correlation between BMD assessments and the relative risk of bone fracture has been reported [2,3], suggesting that other factors besides low BMD likely contribute to determine bone fragility. This lack of information on bone

fracture risk, which is critical for clinical purposes, has prompted intense research to identify new parameters with the ability to assess spongy-bone status and to provide reliable measures of bones resistance.

Magnetic resonance imaging (MRI) was initially appeared unsuitable for assessing bone, due to a rapidly decaying signal of the solid crystalline structure. Due to its peculiarity, MRI was right from the start widely used in functional and morphological clinical assessment of the brain tissue. For this reason, cerebral tissue is better characterized in terms of NMR parameters with respect to the musculoskeletal system. Although bone contains approximately 15% water at various binding stages (primarily interstitial and collagen-bound water), its relaxation properties (T_1 of 250-300 milliseconds and T_2 of 250 microseconds) yield it difficult to detect. However, marrow, whether it is hematopoietic or fatty, has the usual properties of water or fatty acid triglyceride protons characteristic of soft tissue and thus can easily be detected and imaged. Hence, the bone marrow signal, contrasting with the virtual background constituted by the bone, generates an ideal environment for imagebased assessment of trabecular architecture. At present, musculoskeletal imaging is the fastest growing field in MR imaging after neuro-radiological applications. This is mainly due to the demonstrated potentiality of NMR methods for the evaluation of osteoporosis [4, 5]. Although MRI provides no direct information on bone density, with the positive background given by all types of bone marrow, it provides a good resolution of the internal structure of cancellous bone without any radiation dose. Our choice to use NMR methods for osteoporosis assessment is due to their ability to analyze the bone in all its components and properties: by MR relaxometry of bone marrow, on the one hand, is possible to obtain quantitative information about trabecular bone density and spatial rearrangement of bone micro-architecture (this is the first effect of osteoporosis, so it is very useful to study it for the early osteoporosis diagnosis); by MR spectroscopy and water diffusion in bone marrow, on the other hand, is possible to obtain information on the physiological and functional changes joined in osteoporosis.

The absence in literature of a study on the best NMR osteoporosis index and the best heel spongy bone site to detect osteoporosis, induced us to develop this work. We analyzed two heel spongy bone sites, the

calcaneus and the talus. The choice of the heel was mainly due to three reasons: the established correlation between vertebral body fracture and poor trabecular bone density in calcaneus spongy bone [3,6,7], the high heterogeneity of the trabecular bone network in calcaneus [8] and talus and the negligible problems linked to claustrophobic symptoms.

We used a multiparametric approach to investigate heel spongy bone. Specifically $T_2^\star$, T_2, ADC and G_i parameters and marrow fat content by means of MRS were obtained and correlated each others.

The present thesis consists of three parts. In the first part (Chapters 1, 2) the osteoporosis disease with its related fractures are dealt by medical, biochemical and epidemiological knowledge, and the methods by which to diagnose it are described and compared. The second part (Chapter 3) proposes a review of the advanced NMR techniques used in this work. In the last part (Chapters 4, 5, 6, 7) the original experimental results, obtained *in vivo* in heel spongy bone of healthy, osteopenic and osteoporotic subjects were reported. The whole matter of this thesis is organized into seven chapters as follows.

Chapter 1 *The disease and related fractures.* This introductory chapter describes the bone characteristics related to its morphology, composition, physiology and marrow; it also explains the bone mass-sex-age relation, identifies the determinants of peak bone mass, the causes of bone loss and the risk factors for osteoporotic fracture.

Chapter 2 *Diagnosis of osteoporosis.* This chapter is a short review of the methods of measuring bone mass or density, of the BMD thresholds for the classification of the persons as proposed by a WHO Study Group, of the sites and techniques advised for the diagnosis of osteoporosis and of the assessment of fracture risk.

Chapter 3 *Used NMR techniques.* In this chapter the main theoretical concepts of MR spectroscopy and diffusion techniques and of few used pulse sequences are explained.

Chapter 4 ^1H *NMR Spectroscopy of bone marrow.* Here the marrow fat content (Mfc) and its correlation with $T\text{-}score$ parameter and age of the subjects is investigated in an anatomical region rich of yellow marrow, such as the calcaneus.

Chapter 5 *Bone marrow diffusion.* The bone marrow water MR Diffusion and its correlation with $T\text{-}score$, Mfc and Age of the subjects is investigated in calcaneus, in talus and in some their different regions.

Chapter 6 *Internal gradient.* The potential ability of the internal gradient (G_i) parameter to describe spongy bone status related to its trabecular bone density and quality, is assessed by *in vitro* and *in vivo* experiments in calf samples and in postmenopausal subjects respectively. G_i parameter, but also the $T_2^\star$ and T_2 parameters are investigated with their correlations with $T\text{-}score$, Mfc, ADC and Age of the subjects, in calcaneus, in talus and in some their different regions.

Chapter 7 *The best Site-Parameter.* Finally, the power of $T_2^\star$, T_2, ADC, G_i and Mfc NMR parameters to discriminate among normal, osteopenic and osteoporotic persons is underlined in this chapter. Indeed, the best parameter and the best heel spongy bone site, by which to obtain the best discrimination, are indicated. Moreover, the site-parameter couples which best classify the subjects in the same way of $T\text{-}score$, are identified.

Osteoporosis

Chapter 1

The disease and related fractures

Until recently, osteoporosis was an under-recognized disease and considered an inevitable consequence of ageing; perceptions have changed, as epidemiological studies have highlighted the high burden of the disease and its costs to society and health care systems and this trend will be worse in the future because of the mean age increases and so the elderly person number increases.

Osteoporosis is an established and well-defined disease that affects more than 75 million people in Europe, Japan and the USA, and causes more than 2.3 million fractures annually in Europe. It does not only cause fractures, it also causes people to become bedridden with secondary complications and also causes back pain and loss of height, so prevention of the disease and its associated fractures is essential for maintaining health, quality of life, and independence among the elderly.

This systemic skeletal disease is characterized by low bone density and microarchitectural deterioration of bone tissue with a consequent increase in bone fragility; early osteoporosis is not usually diagnosed and remains asymptomatic, it does not become clinically evident until fractures occur. Loss of bone density occurs with advancing age and rates of fracture increase markedly with age.

Osteoporosis is three times more common in women than in men, partly because women have a lower peak bone mass and partly because of the hormonal changes that occur at the menopause. In addition, women live longer than men and therefore have greater reductions in bone mass.

Men lose 15-45% of cancellous bone and 5-15% of cortical bone with advancing age, whereas women lose 35-50% of cancellous bone and 25-30% of cortical bone [9].

The most serious osteoporotic fracture is that of the hip which typically results from fall, but some occur spontaneously; women are more often affected than men and the incidence rates rise exponentially with age. Overall, 90% of hip fractures occur among people aged 50 years and over, and 80% occur in women. The average age at which osteoporotic hip fractures occur is about 80 years in developed countries but is less in countries with lower life expectancies. Hip fractures are usually painful and most of them heal, but with a high degree of morbidity and appreciable mortality, depending in part on the patient's age, the treatment given and associated morbidity; the mean hospital stay is 30 days.

Identifying the incidence of vertebral fractures may be difficult because many are asymptomatic or cause too few symptoms to provoke investigation, so rarely lead to hospitalization. They may occur with osteoporosis or with other diseases; the incidence is greater among women than among men and increase with age but less than that observed for hip fractures.

Forearm fractures are common among the middle-aged and elderly and are generally caused by a fall; the incidence in women increases markedly within 5 years of the menopause, reaches a peak between the ages of 60 and 70 years and levels off thereafter. They are rarely fatal and seldom require hospitalization [1].

1.1   Bone characteristics

1.1.1   Morphology

The bones of the adult skeleton comprise two types of tissue, *cortical or compact*, and *cancellous or spongy bone*. Most bones consist of an outer cortical sheath enclosing a porous trabecular network of cancellous bone that houses the marrow. The trabecular network consists of connecting rods and plates. An important characteristic of trabecular bone is the volume fraction of bone BVF that is the ratio of volume occupied by bone to the volume occupied by bone and marrow. Trabecular bone with a low BVF is typified by an open network

of rods with more isolated islands of trabeculae and more branches that terminate without connecting to another branch (rod-like structure); instead a high BVF means fewer open spaces (plate-like structure). The rods and plates are preferentially oriented along the lines of mechanical strain of the bone. This structure maximizes strength while minimizing weight. In the adults, 80% of the skeleton is cortical bone, however, the relative proportions of cortical and cancellous bone vary in different parts of the skeleton.

In the long bones, like femur and humerus, the *diaphysis* is a hollow
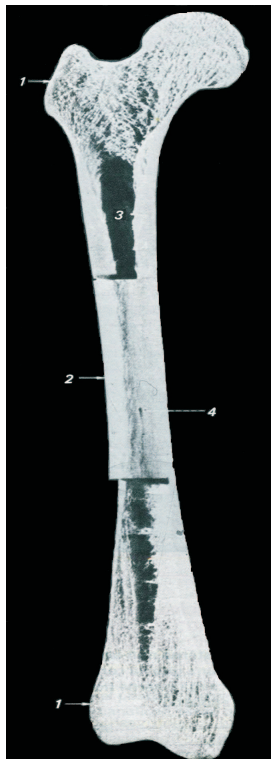
Figure 1.1: Longitudinal section of long bone [10]. 1, epiphysis (spongy bone); 2, diaphysis (compact bone); 3, morrow channel of diaphysis; 4, hole of a nutritive channel.

cylinder of compact bone which preserves the marrow channel (see Fig. 1.1); only the inner layer which borders the marrow is constituted by spongy bone. By means of *metaphysis*, diaphysis is connected in the extremities with *epiphysis*. Epiphysis and the most of short bones like
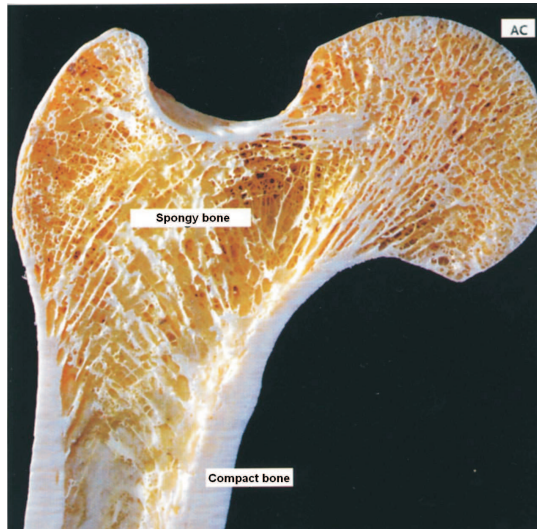
Figure 1.2: Section of dried femur which shows his compact and spongy tissue; the femur's head is covered by a thin layer of articular cartilage AC [11].

calcaneus, are constituted by spongy bone covered by a compact bone thin layer (see Fig. 1.2). In the growth, epiphysis and diaphysis are separated by the so called *conjugation cartilage* or *epiphysial disk*; the transition region between epiphysial disk and diaphysis is metaphysis which is the growth region, in fact when the conjugation cartilage ossifies, the longitudinal growth of the bone stops.

The long bones are covered by a vascularized connective fibrous-elastic thin layer, the *periosteum*. The morrow channel of diaphysis and those of spongy bone are covered by a thin layer of plate cells, the *endosteum*.

1.1.2   Composition

The bone tissue is composed by cells and by an organic and an inorganic intercellular matrix.

The mineral component of bone (*inorganic matrix*) accounts for about 65% of its total dry weight and it is predominantly hydroxyapatite ($Ca_{10}(OH)_2(PO_4)_6$) but also carbonates, citrate, magnesium, sodium, fluoride and strontium.

The *organic matrix* accounts for approximately 35% of the total dry

weight of bone; approximately 90% of this matrix consists of bone-specific collagen, the remainder consists of non-collagenous proteins. The matrix proteins are synthesized and laid down by osteoblasts. Collagen fibres are usually oriented in a preferential direction, giving rise to a typical *lamellar structure* (see Fig. 1.3). The lamellae are generally parallel to each other if deposited along a flat surface such as the surface of the trabecular network or the periosteum, or concentric if synthesized within cortical bone on a surface that borders a channel centered on a blood vessel like the longitudinal haversian channels. These concentric structures within cortical bone are known as *osteons* or *haversian systems* [12]. The cortical bone is also crossed by perpendicular and oblique *Volkmann's channels* which are joined with haversian channels, periosteum, endosteum and bone lacunae in which there are osteocytes. Among these, only bone lacunae are in trabeculae. This interconnected system allows the metabolic and gassy changes between the blood in Havers and Volkmann's channels (in compact bone) or in marrow channel (in spongy bone) and osteocytes.

The bone hardness and rigidity depend on the mineral component of
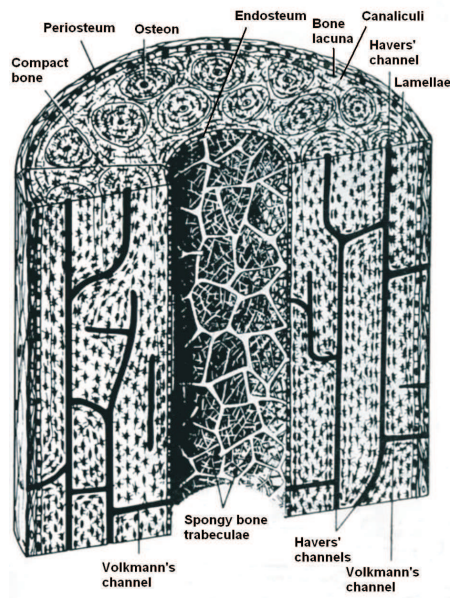

Figure 1.3: Three dimensional picture of diaphysis segment [10].

bone while the traction and pressure resistance on collagen fibres. The plasma concentration and/or the urinary excretion of collagen products and certain non-collagenous proteins reflect the rate of bone formation and resorption [13] and are used clinically as biochemical markers of bone turnover.

The *bone cells* are osteoblasts, osteocytes and osteoclasts.

- *Osteoblasts* are bone-forming cells. They originate from local mesenchymal stem cells (bone marrow stroma or connective tissue mesenchyme), which undergo proliferation and differentiate to pre-osteoblasts and then to mature osteoblasts [14]. Preosteoblasts tally on trabecular surface, in connective tissue of bone's marrow caves, in periosteum inner surface, in endosteum and they cover Havers and Volkmann's channels. The osteoblasts form a unidirectional epithelial-like structure at the surface of the organic matrix. The thickness of this layer, called *osteoid*, depends on the time between matrix formation and its subsequent calcification termed *primary mineralization*. Transport systems located in the plasma membrane of osteoblasts are responsible for the transfer of bone mineral ions, mainly calcium and phosphate, from the extracellular space of the bone marrow to the osteoid layer [15]. The plasma membrane of osteoblasts is rich in alkaline phosphatase, which enters the systemic circulation. The plasma concentration of this enzyme is used as a biochemical marker of bone formation. Towards the end of the production of the bone matrix and the deposition of mineral ions, the osteoblasts become either flat lining cells or osteocytes [16]. A slow process of mineral deposition, by means of other osteoids (*secondary mineralization*), completes the process of bone formation. At the end of the bone formation process, in periosteum and endosteum remain some cells of mesenchymal origin which can differentiate to osteoblasts in replay to appropriate stimulus as like as fractures.

- *Osteocytes* originate from osteoblasts embedded in the organic bone matrix, which subsequently become mineralized. They have numerous long cell processes forming a network of thin canaliculi that connects bone lacunae, in which they are, with active osteoblasts and flat lining cells. Fluid from the extracellular space

in the bone marrow circulates in this network. Osteocytes prob-
ably play a role in the homeostasis of this extracellular fluid and
in the local activation of bone formation and/or resorption in re-
sponse to mechanical loads.
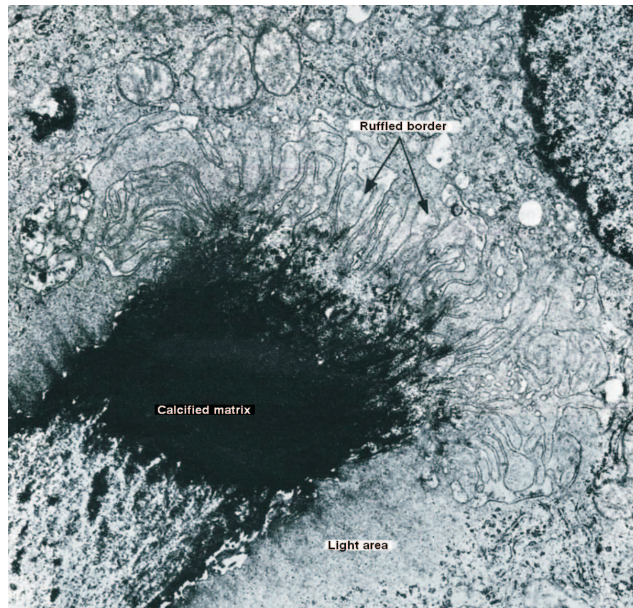
Figure 1.4: Electronic microphotography of an osteoclast. The ruffled
border and the light area of the cellular surface are observable. The
bone calcified matrix near the ruffled border appears erose, while that
near the light area appears normal [10].Magnification 14.000 X

- *Osteoclasts* are giant cells containing $4-20$ nuclei that resorb bone.
  They originate from haematopoietic stem cells, probably of the
  mononuclear/phagocytic lineage, and are found in contact with
  the calcified bone surface within cavities called *Howships lacunae*
  (also known as resorptive lacunae) that result from their resorptive
  activity. Osteoclastic resorption takes place at the cell/bone inter-
  face in a sealed-off microenvironment [17]. In this regard, the most
  prominent ultrastructural feature of osteoclasts is the deep folding
  of the plasma membrane, called the *ruffled border* (see Fig. 1.4), in
  the area apposed to the bone matrix. This structure is surrounded
  by a peripheral ring, called the *light area*, tightly adherent to the

bone matrix, which seals off the subosteoclastic resorbing compartment. The mechanism of bone resorption involves the secretion of hydrogen ions and proteolytic enzymes into the sub-osteoclastic resorbing compartment. The hydrogen ions acidify the extracellular space (pH 4.5) and dissolve the bone minerals, thereby exposing the organic matrix to the proteolytic enzymes [18]. These enzymes are responsible for the breakdown of the organic matrix. The process releases the minerals that contribute to calcium and phosphate homeostasis. Accordingly, biochemical markers of collagen degradation which are found in plasma and urine, can provide estimates of the bone resorption rate.

1.1.3 Physiology

Both the shape and structure of bone are continuously renovated and modified by the processes of modelling and remodelling.

- *Bone modelling* begins with the development of the skeleton during fetal life and continues until the end of the second decade, when the longitudinal growth of the skeleton is completed. In the modelling process, bone is formed at locations that differ from the sites of resorption, leading to a change in the shape or macroarchitecture of the skeleton. Bone modelling may continue, but to a lesser extent, during adult life when resorption at the end endosteal surface increases the mechanical strain on the remaining cortical bone, leading to the stimulation of periosteal bone apposition. This phenomenon, which increases with ageing and is somewhat more pronounced in men than in women, offsets in part the negative effects of bone resorption at the endosteal surface on mechanical strength.

  There are two kinds of osteogenesis: *intramembranous* (or *mesenchymal*) and *endochondral* (or *cartilagineal*). The first is a direct ossification in which bone directly forms on a primitive connective tissue by differentiation of mesenchymal cells in osteoblasts. The ossification process begins in so called *ossification centers* where connective tissue mesenchyme condenses, its cells proliferate and blood vessels form. At first, membranous bone is spongy and

it is constituted by irregular trabeculae which border the primitive spaces of marrow occupied by hematopoietic cells, osteogenic cells and blood vessels. Where bone must be spongy, trabeculae assume a more regular lamellar organization and the inserted connective tissue becomes hematopoietic tissue. Where bone must be compact, trabeculae continue to thicken, filling all or partly the vascular spaces forming the Havers and Volkmann's channels and connective tissue which rings bone condenses in periosteum.
In the endochondral ossification, a cartilagineal model is replaced all or partly by bone.
Osteogenesis of vertebral column, hip, limbs is a duplex process: membranous ossification of periosteum and endochondral ossification (see Fig. 1.5).

- *Bone remodelling* occurs simultaneously with modelling from fetal life through to skeletal maturity, when it becomes the predominant process that occurs throughout adult life. Remodelling maintains the mechanical integrity of the skeleton by replacing old bone with new. Bone resorption and bone formation occur at the same place, so that there is no change in the shape of the bone. In the adult skeleton, approximately $5-10\%$ of the existing bone is replaced every year through remodelling. This does not occur uniformly throughout the skeleton, but in focal or discrete sites.
In both cortical and cancellous bone, the remodelling process begins with bone resorption by osteoclasts. This phase is over within a few days and is followed by the departure of multinucleated osteoclasts. Subsequently, mononuclear cells line the resorption lacunae and deposit a cement line marking the limit of prior erosion and the newly formed bone. These mononuclear cells are subsequently replaced by osteoprogenitor cells, which differentiate into cuboidalshaped osteoblasts. Organic matrix is then laid down, followed by the deposition of minerals. The lacunae are gradually filled with new bone over several months. Thereafter, the osteoblasts change shape and eventually become flattened lining cells. In compact bone osteoclasts form resorption channels which filled with bone become new osteons. The remodelling process is controlled by systemic and locally produced cytokines [19]. The
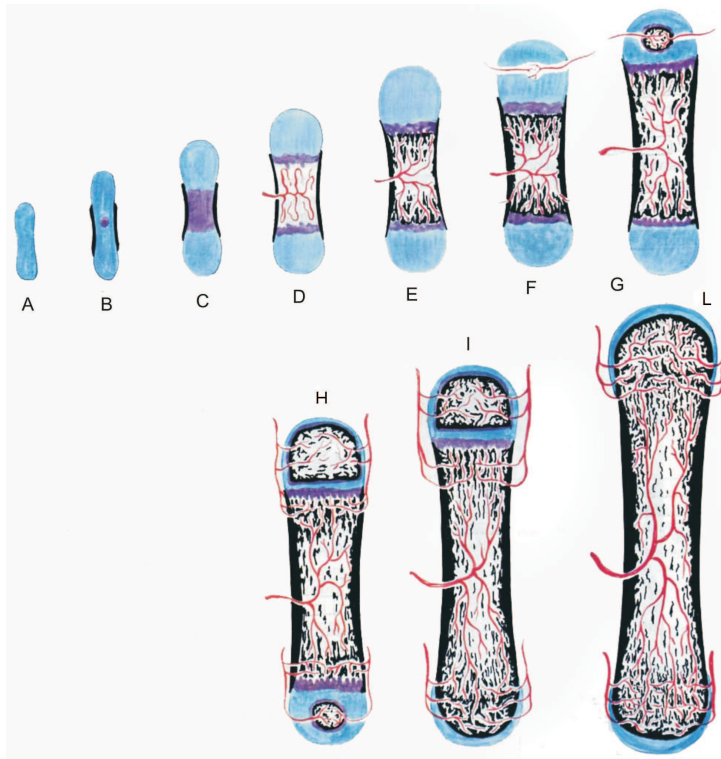
Figure 1.5: Schematization of the long bone growth [10]; cartilage is depicted in blue, calcified cartilage in violet, bone in black, blood vessels in red. **A**, cartilagineal draft; **B**, formation of the periosteal bone muff; **C**, beginning of the cartilage calcification in the center of diaphysis; **D**, **E**, calcified cartilage is partly reabsorbed by chondroclasts, like osteoblasts, with formation of cavities occupied by blood vessels and mesenchyme; **F**, blood vessels and mesenchyme penetrate into cartilage of epiphysis, trabeculae of calcified cartilage and their bone covering are reabsorbed by chondroclasts and osteoclasts to form the first marrow channel draft of diaphysis; **G**, **H**, ossification centers in superior and inferior epiphysis; **I**, **L**, closures of inferior and superior epiphysis by means of ossification of conjugation cartilage and presence of a thin layer of articular cartilage in the extremities.

maintenance of a normal, healthy, mechanically competent skeletal mass depends on keeping the process of bone resorption and formation in balance. Failure to match bone formation with bone resorption results in net bone loss. This is what occurs in osteoporosis.

Osteoclast formation is controlled by several circulating hormones, including parathyroid hormone (*calcitriol*, an active metabolite of vitamin D3), and the gonadal steroids, *estrogen* and *testosterone* [20]. The bone marrow also plays an essential role as a source of cytokines such as tumor necrosis factors (*TNFs*) [21], which also regulate osteoclast formation and activity. These systemic and local factors regulate osteoclast formation and activity in fact hormones and cytokines act on the osteoblastic cells, which possess a cell surface molecule known as RANK ligand (*RANKL*, formerly known as osteoclast differentiation factor), and a cell surface false receptor, osteoprotegerin (*OPG*) [22] (see Fig. 1.6). RANKL is a member of the TNF ligand family and interacts with osteoclast precursors from the haematopoietic lineage (macrophages). This interaction promotes the differentiation and fusion of the osteoclast precursor, thus leading to the formation of mature osteoclasts. Osteoprotegerin is a soluble member of the TNF receptor superfamily that is produced by osteoblast cells and inhibits osteoclast formation. Osteoblasts also secretes the macrophage colony stimulating factor (*M-CSF*), a cytokine which binds itself to c-fms receptor of the osteoclast precursor.

About the mechanisms of hormone action, parathyroid hormone (*PTH*) interacts with osteoblast and stimulates osteoclastogenesis increasing RANKL and M-CSF productions and decreasing OPG production, *calcitonin* inhibits bone resorption by acting directly on mature osteoclasts, *bisphosphonates*, which are used in treating osteoporosis, also inhibit osteoclasts, probably by interfering with the system of communication between osteoblasts and osteoclasts, but also reduce the number of osteoclasts by inhibiting either their recruitment or their survival, estrogen and probably testosterone exert their effects on the bone resorption by inhibiting the production of cytokines, particularly TNFs.

Several growth factors can stimulate the proliferation of osteoblasts in vitro [23]. Their respective importance in vivo is not yet clear.
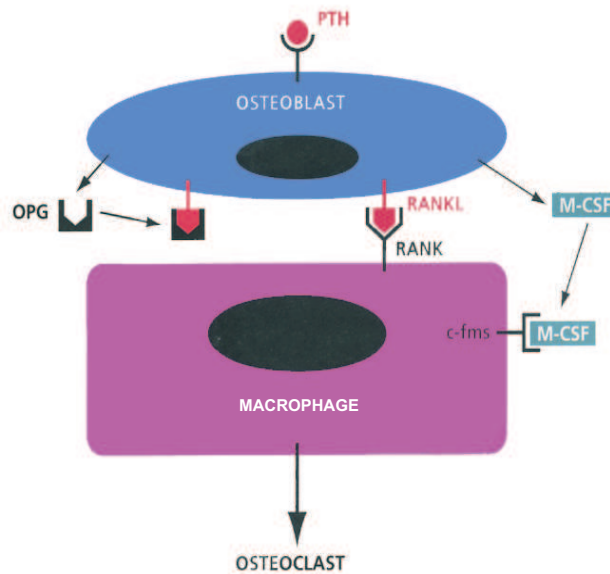
Figure 1.6: Osteoclastogenesis mechanism [10].

Nevertheless, it has been suggested that the production and action of growth factors are vital to the stimulation of bone formation in response to systemic hormones such as PTH, osteogenic agents and mechanical strain [24].

Virtually all (99%) of the bodys calcium is located in bone and teeth. Only 0.1% is in the extracellular compartment and the remainder is within cells. The maintenance of a constant extracellular concentration of ionized calcium (*calcium homeostasis*) is essential, because calcium influences many physiological functions and biochemical pathways. The extracellular concentration of calcium is regulated by a dynamic equilibrium between the levels calcium in the intestine, kidney and bone [25]. In young adults, the rates of calcium entering and leaving the extracellular compartment are equal. The urinary excretion of calcium represents the difference between the amount filtered and that reabsorbed. In a steady state, urinary calcium excretion corresponds roughly to the net calcium fluxes entering the extracellular compartment from the intestine and bone. In the kidney 98% of the calcium filtered by the glomerulus is reabsorbed in the renal tubule. The major regulator of the intestinal

absorption of calcium is calcitriol [26]. It is formed in the kidney, and its production is controlled by PTH and the extracellular concentrations of calcium and phosphate. The main regulator of the renal tubular reabsorption of calcium is PTH, secretion of which is controlled by the extracellular concentration of calcium [27].

1.1.4   The bone marrow

As one of the larger and more important organs in the human body, bone marrow plays important physiologic roles in both health and disease. In healthy individuals, its function is to provide a continual supply of red cells, platelets, and white cells to meet the body's demands for oxygenation, coagulation, and immunity. As such, bone marrow frequently becomes a target, either directly or indirectly, of many varied disease processes.

The basic microstructure of bone marrow consists of an osseous framework housing fat cells and hematopoietic cells both supported by a system of reticulum cells, nerves, and vascular sinusoids. Cellular constituents of marrow include all stages of erythrocytic and leukocytic development, as well as fat cells and reticulum cells [28]. *Erythrocytic*, *granulocytic*, and *megakaryocytic cell lines* replenish the body's supply of red cells, white cells and platelets. The role of *fat cells* in marrow function is unclear. Speculation suggests that fat cells provide surface and nutritional support and possibly growth factors for hematopoiesis. *Reticulum cells* consist of both phagocytic cells (macrophages) that play a role in immunity and undifferentiated nonphagocytic cells whose role is yet to be fully defined. In red marrow, these nonphagocytic reticulum cells occur in greater abundance in perivascular locations and form a reticular meshwork that provides nutritional and mechanical support to the hematopoietic cells. These reticular cells appear to have the capacity to accumulate lipid and transform into the fat cells of red and yellow marrow.

The various components of normal marrow may be simplified into a unifying concept-that of red and yellow marrow. That fraction of bone marrow actively involved in the production of blood cells is termed *hematopoietic or red marrow*. The remaining fraction, which is hematopoietically inactive, is termed *yellow marrow*. Important anatomic

and compositional differences exist between these two types of marrow. On average, the chemical composition of red marrow is approximately 40% water, 40% fat, and 20% protein. The cellular composition of red marrow is 60% hematopoietic cells and 40% fat cells. Red marrow has a rich, arborized vascular network. Yellow marrow's chemical composition is approximately 15% water, 80% fat, 5% protein. Its cellular composition is 95% fat cells and 5% nonfat cells. Physiologically, the fat cells in yellow marrow are relatively stable, while those in red marrow appear to be labile. Yellow marrow has a sparse vascular network.

At birth, virtually the entire marrow space contains red marrow. During growth and development, conversion of red to yellow marrow occurs throughout the skeleton. This conversion begins in the immediate postnatal period and is first evident in the terminal phalanges of the hands and feet [29]. The process then progresses from peripheral (appendicu-

Figure 1.7: Adult pattern of red/yellow marrow. Usually by 25 years of age, the primary conversion of red to yellow marrow has been accomplished and the adult distribution of red/yellow marrow established. Red marrow is concentrated in the axial and proximal appendicular skeleton while yellow marrow occupies the remainder of the appendicular skeleton.

lar) toward central (axial), with respect to the skeleton as a whole, and

from diaphyseal to metaphyseal in individual long bones. Flat bones and vertebral bodies show similar patterns. Although generally symmetric, the rate and extent of conversion is not uniform but varies according to site in a particular bone as well as among bones. Usually by 25 years of age, the process of primary red marrow conversion to yellow marrow is complete and a balanced distribution of red and yellow marrow has been achieved [30]. This balance will vary from person to person as it is influenced by at least age, gender, and health. Similarly, the balance between red and yellow marrow achieved in individual bones varies by location. Red marrow is predominately concentrated in the axial skeleton (skull, vertebrae, ribs, sternum, and pelvis) and the proximal appendicular skeleton (proximal femora and humeri) (see Fig. 1.7). Yellow marrow dominates the remaining portion of the appendicular skeleton and is variably admixed throughout the axial skeleton. Physiologic conversion of red to yellow marrow continues after 25 years of age, albeit at a slower pace and islands of hematopoietic tissue may be found in areas dominated by fatty marrow and vice versa. The process of red to yellow marrow conversion is, at times, halted or reversed as alterations in the body's demand for hematopoiesis provoke a reconversion of yellow marrow to red marrow. Thus, the process occurs first in the axial skeleton followed by the appendicular skeleton in a proximal to distal sequence.

1.2   Peak bone mass and loss of bone

The peak bone mass is the amount of bone tissue present at the end of skeletal maturation. It is a major determinant of the risk of fracture due to osteoporosis since the mass of bone tissue at any time during adult life is the difference between the amount accumulated at maturity and that lost with ageing. There is, therefore, considerable interest in exploring ways to increase peak bone mass.

1.2.1   Bone mass-sex-age relation

There is no evidence for sex differences in bone mass at birth. This absence of a substantial sex difference in bone mass is maintained until the onset of puberty [31]. The difference following puberty is characterized by a more prolonged period of bone maturation in males than

in females, resulting in a greater increase in bone size and cortical thickness but there is no significant sex difference in the volumetric trabecular density at the end of puberty. There is also an asynchrony between the gain in standing height and the growth of bone mineral mass during puberty. This phenomenon may be responsible for the transient fragility that may contribute to the higher incidence of fracture that occurs near puberty. In adolescent girls, the gain in bone mineral density *BMD* declines rapidly after menarche and is insignificant 2 years later. In adolescent boys, the gain is particularly rapid between the ages of 13 and 17 years but declines markedly thereafter in all sites except the lumbar spine and mid-femur, where growth continues until the age of 20 years. This suggests an important sex difference in the magnitude and/or duration of the phase that contributes to the ultimate peak bone mass. Bone mass does not change significantly between the third and fifth decades. At the beginning of the third decade, there is a large variability in the normal values of BMD [32], particularly at sites susceptible to osteoporotic fractures, such as the lumbar spine and femoral neck. This variance is not substantially reduced by correction for standing height, and does not appear to increase significantly during adult life.

1.2.2   Determinants of peak bone mass

Determinants of peak bone mass include heredity, sex, endocrine factors, dietary factors, mechanical forces and exposure to risk factors.

- *Heredity.*
  Studies suggest that genetic factors may account for up to 50% or more of the variance in BMD values in the population [33]. The contribution of genetic factors to bone mineral mass and density is slightly less at the proximal femur and the forearm than at the lumbar spine, suggesting that the impact of genetic (or genetic and environmental factors) varies according to the skeletal site. Genetic determinants appear to be expressed before puberty as shown by correlation in BMD and bone size between prepubertal daughters and their premenopausal mothers, a model in which half

of the genes are common. The heritability of peak bone mass is likely to be polygenic.

- *Endocrine factors.*
  Various endocrine factors influence bone growth. The production of these steroids increases before and during puberty, but the time-course of their production does not match the accelerated gain in bone mass. In contrast, calcitriol concentration and the tubular reabsorption of inorganic phosphate rise with the accrual of bone mass. This may be an adaptive response to the increased demand for calcium and phosphate.

- *External factors.*
  Modification of environmental factors can cause an individual to change the track of bone accrual. *Nutritional factors* are particularly important determinants of peak bone mass and rate of gain of bone mass. The amount of calcium and protein in the diet modulate the gain in bone mass and calcium supplementation significantly enhances the rate of BMD in children and adolescents.

Various disorders impair the optimal acquisition of bone mass during childhood and adolescence. In diseases such as anorexia nervosa and exercise-associated amenorrhoea, malnutrition, sex steroid deficiency and other factors combine to increase the risk of osteopenia or low bone mass. This is probably also the case for various chronic diseases, which in addition may require therapies that affect bone metabolism.

Delayed puberty is defined as the absence of any sign of puberty at the attainment of the upper normal limit of chronological age for its onset [34]. Epidemiological studies have provided indirect evidence that late menarche decreases peak bone mass and is a risk factor for osteoporosis. In addition, osteopenia has been reported in a cohort of men with a history of delayed puberty. The onset of puberty is a complex process involving the activation of endocrine systems of which the targets include factors influencing the bone mineral balance and the growth rate of the skeleton.

Significant deficits in both cancellous and cortical bone are observed in young adult women with chronic *anorexia nervosa*, and may be severe

enough to result in osteoporotic fractures.

The acquisition of bone mass may be impaired when women with hypogonadism and low body weight engage in intensive physical activity *exercise-associated amenorrhoea*. Intensive training during childhood may contribute to the later onset and completion of puberty.

1.2.3   Loss of bone

The onset of substantial bone loss is usually around age 65 years in men and 50 years in women. There is little variation in bone size throughout life, beyond continuous, slight expansion of the outer dimensions. The expansion of the periosteal surface is less than the increase in space occupied by the bone marrow which results from a greater resorption at the endosteal surface. Under these conditions, the bone cortex becomes thinner. This process, together with increasing porosity of cortical bone and destruction of trabeculae through thinning and perforation, accounts for age-dependent bone loss.

Estrogen is necessary, not only for maximizing peak bone mass in men and women, but also for maintaining it. It controls bone remodelling in reproductively active women and in ageing men. Estrogen deficiency accelerates the rate of bone turnover, thereby altering the balance between bone formation and bone resorption, and appears to be the main cause of osteoporosis in women after the fifth decade, and possibly in men.

Among the other endocrine causes of bone loss, *primary hyperparathyroidism* and *hyperthyroidism* increase the rate of bone turnover, thereby inducing bone loss [35]. In contrast, excess *glucocorticoids* reduce bone formation. In addition, administration of glucocorticoids in pharmacological excess may decrease the intestinal absorption of calcium and possibly also its reabsorption by the renal tubules. These latter two effects would lead to a negative calcium balance and result in increased bone resorption.

Among *nutritional factors* that cause bone loss, deficiencies in calcium, vitamin D [36], and protein [37] have been shown to be associated with deficient skeletal growth or accelerated bone loss. In the elderly, several factors contribute to negative calcium balance. With ageing, calcium intake decreases because of reduced consumption of dairy products, and

the absorptive capacity of the intestinal epithelium to adapt to low calcium intake is impaired. The capacity of the renal tubule to reabsorb calcium, and its responsiveness to PTH are impaired. Exposure to sunlight and the capacity of the skin to produce vitamin D are also reduced in the elderly; severe and prolonged deficiency of vitamin D results in rickets in children and osteomalacia in adults, conditions characterized by defective mineralization of bone, osteomalacia will aggravate osteoporosis, since both increase the risk of fracture. Vitamin D deficiency is rare in Europe and the USA, but is still common in the Middle East and the Asian subcontinent. Increasing calcium intake is certainly an important strategy which is relatively easier to implement than other possible preventive measures. Low protein intake is an important determinant of peak bone mass and therefore of the risk of osteoporosis in later life; protein replenishment in patients with hip fracture can improve not only BMD, but also muscle mass and strength. Dietary intake of phosphates may be increasing in some populations as a result of their use as food additives and the increase in intake of carbonated drinks. These drinks may have a deleterious effect on bone, because they have replaced milk in the diet of some young people, and because high intakes of phosphates stimulate the secretion of PTH, but there is no evidence so far that high phosphate intakes accelerate bone loss in humans.

1.2.4 Risk factors for osteoporotic fracture

Osteoporosis is characterized by low bone mass which may be the consequence of development of the skeleton during adolescence (low peak bone mass) and/or excessive bone loss thereafter. Its clinical and social consequences, however, are the result mainly of the associated fractures. Lifetime fracture risk depends both on fracture incidence of a kind of bone and life expectancy (see Table 1.1). These two factors are different among countries. Fracture rates is in fact highest in North America and Europe, particularly in Scandinavia [38]. The risk of osteoporotic fractures is instead lower in Africa and Asia. Any structural engineer knows that the static and dynamic strength of a structure is a function of the materials intrinsic properties, the amount of material per unit volume (apparent density), and its spatial arrangement. Bone is a composite material that must obey the same fundamental principles.

Fracture site	Lifetime risk of fracture (%) (95% CI)	
	Women	Men
Proximal femur	17.5 (16.8 − 18.2)	6.0 (5.6 − 6.5)
Vertebra (a)	15.6 (14.8 − 16.3)	5.0 (4.6 − 5.4)
Distal forearm	16.0 (15.7 − 16.7)	2.5 (2.2 − 3.1)
Any of the above	39.7 (38.7 − 40.6)	13.1 (12.4 − 13.7)

CI, confidence interval.

(a) Clinically diagnosed fractures.

Table 1.1: Estimated lifetime risk of fracture in Caucasian men and women at age 50 years in Rochester, MN, USA [9].

It is generally agreed that around 60% of the bones mechanical competence typically can be explained by variations in the apparent density (bone mass/tissue volume). The remainder is likely due to other parameters related to bone quality. So, in addition to bone mass, other *skeletal components* also influence bone strength, including both the macro- and microarchitecture of bone and the degree of mineralization of the matrix as well as the crystal characteristics [39]. In cortical bone, mechanical strength is affected by the histological structure, including the presence of primary versus osteonal bone, the orientation of the collagen fibres, the number and orientation of the cement lines, and the presence of microdamage. In cancellous bone, mechanical strength is affected by the microstructural arrangement of the trabeculae, including their orientation, connectivity, thickness, and numbers. The macro- and microarchitectural components of bone strength could explain, at least in part, clinical observations that variations in bone mineral mass are not closely correlated with changes in fracture rate. Throughout most of adult life, aging bones become more structurally efficient and retain their strength even though BMD declines. They get larger with thinner cortical walls, thus maintaining strength despite BMD loss. The homeostatic mechanism for strength maintenance depends on skeletal loading. Thus, to maintain bone strength, normal loading on the skeletal system must be maintained. Absence of loading during prolonged spaceflight can cause uncompensated loss of bone strength.

The risk of fragility fractures also depends on several *extraskeletal fac-*

tors. A fracture is a structural failure of the bone that occurs when the forces applied to it exceed its load-bearing capacity. Thus, independently of the size, geometry and physical properties of the bone, the direction and magnitude of the applied load will determine whether a bone will fracture in a given situation. Falls are the most common cause of traumatic osteoporotic fractures, but the mechanics of falling are such that only about 5% of falls lead to a fractures. The occurrence of one osteoporotic fracture may also increase the risk of future fractures [40]. About genetics, up to 50% of the variance in peak bone mass and some aspects of bone architecture and geometry relevant to bone strength may be determined genetically [41].

As previously said, dietary factors influence peak bone mass, age-related bone loss but also fracture risk. Calcium and vitamin D are particularly important since deficiencies are potentially correctable.

Immobility is an important cause of bone loss, in contrast, bone density increases in response to physical loading and mechanical stress.

Cigarette smoking reduces BMD as a result of the consequent earlier menopause, reduced body weight and enhanced metabolic breakdown of exogenous estrogen in women [42].

Studies of people dependent on alcohol have suggested that high levels of alcohol consumption may be detrimental to bone, however, moderate consumption of alcohol has not consistently been associated with increased risk of fracture or reduced bone density. In postmenopausal women, alcohol consumption appears to reduce both bone loss at the hip and the risk of vertebral fracture [42].

Low body mass index (BMI) is associated with lower peak bone mass, and an adverse influence on bone loss. This may be the consequence of reduced peripheral estrogen production by adipose tissue and metabolic influences on body composition. Accelerated weight loss is also an important determinant of the risk of hip fracture.

Primary hypogonadism in both sexes is associated with low bone mass, and decline in estrogen production at the menopause is the most important factor contributing to osteoporosis in later life. Late menarche may be associated with lower peak bone mass and higher fracture risk. The use of oral contraceptives may be associated with higher bone mass. A premature menopause is a strong determinant of bone density and in-

creased risk of fracture.

An increased risk of osteoporosis is associated with a host of other diseases and disorders, including endocrine and metabolic disorders, and malignant disease, and with the use of certain drugs.

So, hormonal therapy, physical exercise and calcium and vitamin D intakes can limit the bone loss but not necessarily bone returns to its previous condition.

Chapter 2

Diagnosis of osteoporosis

The internationally agreed description of osteoporosis is that it is a systemic skeletal disease characterized by low bone mass and microarchitectural deterioration of bone tissue, with a consequent increase in bone fragility and susceptibility to fracture. This view of osteoporosis embodies the concept that bone mass is an important factor in the risk of fracture, but that other skeletal abnormalities contribute to skeletal fragility, while some non-skeletal factors also affect fracture risk. The assessment of fracture risk should therefore encompass all these factors.

2.1 Methods of measuring bone mass or density

The bone mass of a particular part of the skeleton is directly dependent on both the volume or size of the part concerned and the content of the mineralized tissue contained within its periosteal envelope (*bone mineral content BMC* in gram of hydroxyapatite). The mean volumetric mineral density of bony tissue (*volumetric BMD* in gram of hydroxyapatite per cm^3) can be determined by quantitative computed tomography (QCT). The *areal or surface BMD* (in gram of hydroxyapatite per cm^2) can be determined by single- or dual-energy X-ray absorptiometry (SXA and DXA). There are also other methods of measuring bone mass or density like *quantitative ultrasound QUS*, *radiography* and *nuclear magnetic resonance NMR*. The last one it will discuss in the next chapters. The values generated by these techniques are directly dependent on both the size and integrated mineral density of the scanned skeletal tissue. The integrated mineral density is determined

by cortical thickness, the number and thickness of the trabeculae, and
the true mineral density corresponding to the amount of hydroxyapatite
per unit volume of the bone organic matrix.

- *Single- and dual-energy X-ray absorptiometry (SXA and DXA).*
  Single and dual X-ray absorptiometry (SXA, DXA) are methods
  of assessing the mineral content of the whole skeleton, as well as
  of specific sites, including those most vulnerable to fracture. The
  term *bone mineral content BMC* describes the amount of mineral
  in the specific bone site scanned, from which a value for BMD
  can be derived by dividing the bone mineral content by the area
  or volume measured. With both SXA and DXA this is an areal
  density rather than a true volumetric density, since the scan is
  two-dimensional, as illustrated in Fig. 2.1.

  In single-energy absorptiometry, bone mineral is measured at

Figure 2.1: Two-dimensional DXA scan of the lumbar spine and hip in
a young healthy adult [1].

  appendicular sites, such as the heel or wrist. Dual-energy absorp-
  tiometry measures bone mineral at sites such as the spine and hip
  and it can also measure total body bone mineral; SXA cannot be

used for these sites. DXA is also being increasingly used for measurements at appendicular sites.

Of the many techniques developed to assess bone mass, bone mineral or other related aspects of skeletal mass or structure, the most highly developed technically and the most thoroughly validated biologically is DXA, which is regarded as the gold standard and is used for the diagnosis of osteoporosis, prognosis (fracture prediction), monitoring the natural history of the disorder, and assessing response to treatment. The WHO classification of osteoporosis was based on DXA measurement of BMD at central sites and forearm. DXA scans are commonly used because of their high precision and accuracy, ability to measure bone density at clinically relevant sites (i.e., hip and vertebrae), and modest radiation exposure. The major disadvantages are that the machines are expensive, not portable, and no widely available. DXA uses two x-ray beams of different energy levels to scan the region of interest and measure the attenuation as the beam passes through the bone. Low-energy beams experience greater attenuation than high-energy beams, and bone attenuates x-rays more than soft tissue. Based on this discrepancy, corrections for soft tissue can be made, which are particularly important due to the individual variability in soft tissue content around the hip and spine.

The mathematical theory of DXA (referred to as basis set decomposition) holds that the X-ray transmission factor through any physical object can be decomposed into the equivalent areal densities of any two designed materials [43]. For DXA scans, the two materials chosen are hydroxyapatite and soft tissue. It follows that DXA scan results will only accurately reflect the true BMD if the object being examined is made up solely of the two chosen materials. In practice, for the purpose of describing the transmission of X-rays the human body is made up of not two but three types of tissue, namely bone, lean tissue and fat. Neglecting the difference between lean and fat can cause errors in DXA measurements with misrepresentation of the patient's true bone status when BMD results are interpreted in terms of T-scores (see section 2.2); Blake estimated that an increase in marrow fat content from 0 to 100%

caused the measured BMD to decrease by 0.14 g/cm^2 (1.3 T-score units) in women and 0.16 g/cm^2 (1.3 T-score units) in men [44].

- *Quantitative computed tomography (QCT).*
  QCT is based on the differential absorption of ionizing radiation by calcified tissue. Conventional whole body CT scanners, which typically generate density information in terms of Hounsfield units, need to be transformed to convert their results into units relevant to BMD, then attenuation measurements are compared with a standard reference to calculate bone mineral equivalents; for spine QCT, the patient is usually scanned simultaneously with a calibration phantom for automatic standardization. Quantitative computed tomography (QCT) has been applied both to the appendicular skeleton and to the spine (see Fig. 2.2). Dedicated equipment for assessing density at peripheral sites (pQCT) is widely used in Europe. The major advantage of QCT in the assessment of cancellous bone density, as compared with DXA, is that it measures true volumetric density, rather than providing an area-adjusted result as does DXA and this may be useful in assessing response to therapy in the cancellous bone and in the prediction of fracture risk. Its major disadvantages are high radiation exposure, difficulties with quality control, high cost and less precision compared with DXA, it is also less available than all the other methods. Recent advances in imaging technology, notably micro-computed tomography (μCT) and micro-magnetic resonance imaging (μMRI), offer an opportunity to test the hypothesis that architecture is an independent contributor to bone strength. They give complexity measurements that concern the bone three-dimensional structural composition like spatial dynamics, local inhomogeneities of trabecular network, structural complexity (interstratification), trabecular disorders and organization of marrow space for μCT. In vivo, however, dose limitations and point-spread function (PSF) blurring of x-ray based tomographic methods severely limit the achievable resolution even at peripheral anatomic sites; in fact it is possible to acquire images at a voxel size of 165 x 165 x 165 μm^3 although the width of the beam-size limited PSF is about 280 μm [5]. Unfortunately, this resolution is generally not sufficient to

Figure 2.2: QCT scan of the lumbar spine. Vertebrae L1, L2, L3 are indicated.

resolve trabecular elements without excessive partial volume blurring.

- *Radiography.*
  Osteoporosis can often be diagnosed by visual inspection (*radiographic morphometry*) of plain radiographs. In addition, some quantitative techniques may be useful in assessing risk. The most widely used is the estimate of the cortical width of the second, third and fourth metacarpals. Since the size of tubular bones increases with age, thinning of the cortex represents an increase in net endocortical bone resorption. The ratio of the cortical width to the total width is therefore commonly used indices. Another technique is *radiographic absorptiometry RA* using an aluminum step-wedge incorporated into the film, thus permitting an estimate of areal density to be made. Common sites of assessment include the metacarpals, the distal phalanges and the distal forearm. Both absorptiometry and morphometry have been used for many years, but their usefulness in assessing fracture risk is only now being

validated in prospective studies. In recent years it has become
apparent that vertebral deformity is a very strong risk factor for
subsequent fractures. There is, therefore, great interest in identi-
fying vertebral deformities due to osteoporosis that may not have
otherwise come to clinical attention.

- *Quantitative ultrasound (QUS).*
  Quantitative ultrasound (QUS) has recently been used to assess
  skeletal status in osteoporosis. The methods thoroughly evaluated
  are broad-band ultrasound attenuation (BUA), which results from
  scattering and absorption and speed of sound (SOS) (or ultrasound
  velocity), which depends on elasticity and density. Because bone
  (particularly cancellous bone) is inhomogeneous, ultrasound scat-
  tering is complex. Attenuation in bone is determined by plotting
  the linear relationship of the amplitude loss of the sound wave at
  various frequencies. The slope of this line is referred to as the
  broadband ultrasound attenuation (BUA). Attenuation is influ-
  enced by both bone density and microarchitecture. These methods
  have the advantage in that they do not involve ionizing radiation
  and may provide information on the structural organization of
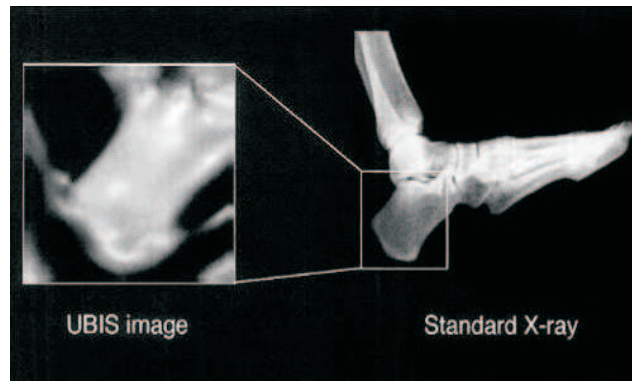 bone in addition to bone mass.

Figure 2.3: An ultrasound image using the UBIS 5000 and a standard
X-ray of the calcaneus [45].

QUS techniques cannot at the present time provide diagnostic criteria
for osteoporosis, but on current evidence they are suitable for the as-

sessment of fracture risk in elderly women. Their use has been best established for calcaneal systems. Its low cost and portability make QUS more attractive for use in assessing the risk of fractures in larger populations than may be appropriate for bone densitometry by X-ray absorptiometry. Therefore, ultrasound assessment of bone density is acceptable for screening at-risk individuals with confirmation of the diagnosis by DXA. Ultrasound densitometry is not recommended to monitor response to therapy because its sensitivity and confidence intervals are too wide.

2.2 BMD thresholds

The most straightforward approach to the diagnosis of osteoporosis by bone density measurements is to define a threshold for BMD that will encompass most patients with osteoporotic fractures. However, bone density measurements are also used to assess future risk of fracture, so that more than one threshold will be needed.

Skeletal mass and density remain relatively constant once growth has ceased, until approximately age 50 years in females and 65 years in males. For every age, the distribution of BMC or BMD in healthy women is approximately normal irrespective of the measurement technique used. Female individual bone density values are expressed in relation to the distribution of BMD of a young female reference population, aged 50 years, in standard deviation units from the peak of distribution. This reduces the effects of differences in calibration between instruments. Standard deviation units used in relation to the young healthy population of same ethnicity and sex are called *T-scores*. The following four general diagnostic categories for women have been proposed by a WHO Study Group based on measurements by DXA [9]:

- *Normal.*
  A value of BMD within 1 standard deviation of the young adult reference mean (T-score ≥ -1).

- *Low bone mass (osteopenia).*
  A value of BMD more than 1 standard deviation below the young adult mean, but less than 2 standard deviations below this value ($-2.5 <$ T-score < -1).

- *Osteoporosis.*
  A value of BMD 2.5 standard deviations or more below the young adult mean (T-score ≤ -2.5).

- *Severe osteoporosis (established osteoporosis).*
  A value of BMD 2.5 standard deviations or more below the young adult mean in the presence of one or more fragility fractures.
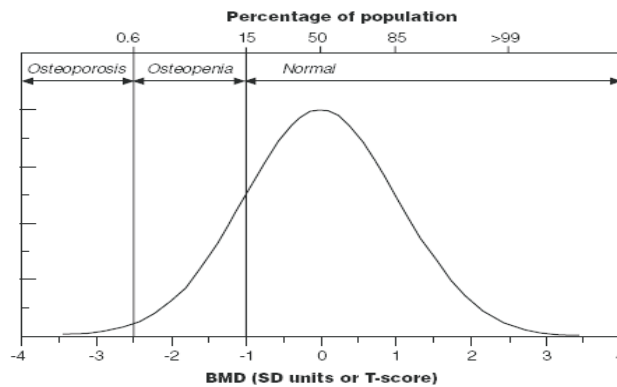
Figure 2.4: Distribution of BMD in young healthy women aged 50 years [1].

In women, bone loss occurs predominantly after the menopause. In the young healthy population, because the distribution of bone density is normal, approximately 15% of the population have a T-score of -1 or lower (low bone mass or osteopenia) and about 0.6% of the population have a T-score of -2.5 or less (osteoporosis)(see Fig. 2.4).
Since the distribution of BMD in the population is normal at all ages, the proportion of women affected by osteoporosis at any one site increases markedly with age in the same way as fracture risk increases with age (see Fig. 2.5). The proportion of patients with osteoporosis increases approximately exponentially with age and is in line with the increasing incidence of many osteoporotic fractures among ageing women.

The *Z-score* is the number of standard deviations above or below what's normally expected for someone of same age, sex and ethnic or racial origin (see Fig. 2.6). This is helpful because it may suggest have a secondary form of osteoporosis through which something other than aging is causing abnormal bone loss. A Z-score less than -1.5 might
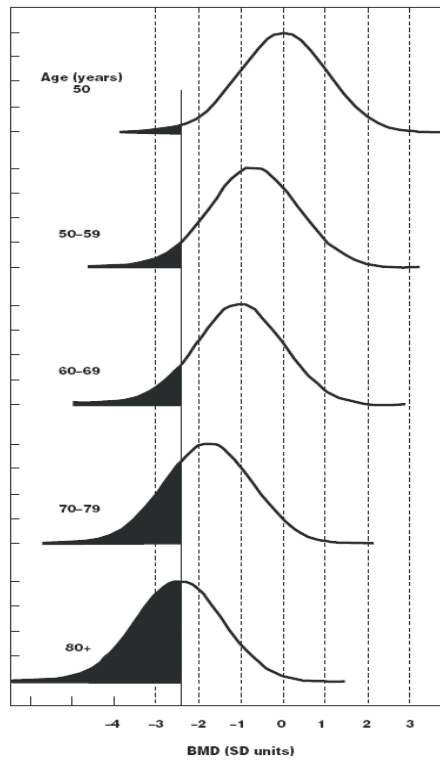
Figure 2.5: Distribution of BMD in women at different ages, and the prevalence of osteoporosis [1].
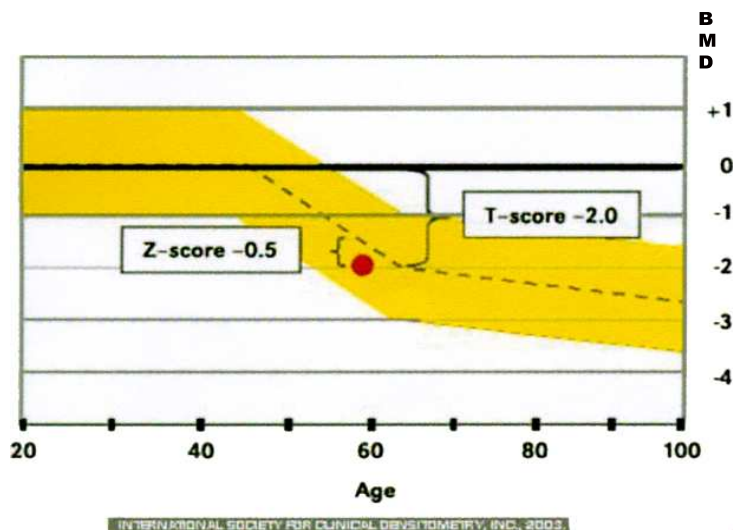
Figure 2.6: Interpreting T-scores and Z-scores. The T-score compares
bone density of a skeletal site of a patient with that of an average healthy
young adult of same ethnicity and sex. So if T-score is -2.0, bone den-
sity is lower than average by two standard deviations. The Z-score, on
the other hand, tells us how bone mass of a patient compares with that
of someone age, ethnicity and sex. So if Z-score is -0.5, bone density
is less than the norm for people same age by one-half of a standard
deviation.

indicate these other factors are to blame.

Diagnostic cut-off values for men are not well established. However, population studies and a prospective study have both suggested that the cut-off value for spine or hip BMD used in women, i.e. 2.5 standard deviations or more below the average, can be used for the diagnosis of osteoporosis in men since the risks of hip and vertebral fractures are similar in men and women for any given BMD [46]. This threshold value may require adjustment for body size in some populations.

2.3 Sites and techniques

T-scores obtained by different techniques and at different sites cannot be used interchangeably. A gold standard for diagnosis should therefore be based on a particular site and technology. Measurements of T-scores at the hip are the best predictors of hip fracture and the hip is the site of greatest biological and clinical relevance, since hip fracture is the dominant complication of osteoporosis in terms of morbidity and cost. The T-score measured at the hip with DXA therefore provides the best diagnostic criteria. The selection of a standardized site and technology for diagnosis does not preclude a valuable role for other techniques in the assessment of fracture risk.

The ability of DXA and of other techniques to provide a diagnosis of osteoporosis depends critically on their performance characteristics (see Table 2.1). In the diagnostic use of these techniques, precision or reproducibility is the degree to which further measurements will show the same or similar results, accuracy is the degree to which a given test measures BMD correctly; the accuracy of DXA at the hip exceeds 90%. Residual errors arise for a variety of reasons, related to the technique itself and the manner in which the technique is applied. For example, standard DXA techniques use a two-dimensional projection and do not, therefore, measure BMD (g/cm^3), but rather areal density (g/cm^2). Thus, the size of the bone affects the apparent density since the relationship between area and volume is non-linear. Systematic inaccuracies with DXA occur particularly at the spine since the vertebrae are irregular in shape and apparent density. This systematic error in measured BMD when different machines are used can be partially avoided by us-

ing T-scores. Non-systematic errors of accuracy also occur, the largest
source of error arises because of variable soft tissue density. The sources
of error in the diagnosis of osteoporosis by means of DXA are multi-
plex. Thus osteomalacia, a complication of poor nutrition in the elderly,
causes bone mass to be underestimated, extreme obesity and overlying
metal objects cause bone mass to be overestimated; osteoarthritis at the
spine or the hip is common in the elderly, and contributes to the density
measurement but not necessarily to skeletal strength; heterogeneity of
density due to osteoarthrosis or previous fracture can often be detected
on the scan and sometimes excluded from the analysis. Some of these
problems can be overcome with adequately trained staff and rigorous
quality control.

The WHO diagnostic classification cannot be applied to T-scores from
measurements other than DXA at the femur neck, total femur, lum-
bar spine, or one-third distal (33%) radius because those T-scores are
not equivalent to T-scores derived by DXA. The exclusive applicability
of the WHO diagnostic classification to DXA is inherent in the defini-
tion. Thus, the absence of an equivalent classification for techniques
other than DXA does not indicate problems of these techniques but
a deficiency of the WHO classification. This limitation is historically
understandable, since at the time of the formation of the WHO classi-
fication appropriate epidemiological data were only available for DXA.
At the spine, for example, T-scores measured with QCT are lower than
those measured with DXA. Equivalent values of T-score thresholds may
be defined for spinal QCT using the concept of comparable sensitivity
and specificity to discriminate vertebral fractures: a DXA T-score of
-2.5 would correspond to an equivalent QCT T-score of -3.3 [47].

2.4   Assessment of fracture risk

Osteoporosis is clinically significant as a predictor of fractures,
and it is for this reason that BMD measurements are of such great inter-
est. Studies with DXA indicate that the age-adjusted relative increase
in risk of fracture (the gradient of risk) approximately doubles for each
standard deviation decrease in BMD [48]. The diagnosis of osteoporosis
is based on a value for BMD below a cut-off threshold, but there is no

Technique	Site	Cancellous bone (%)	Precision error in vivo (%)	Accuracy error in vivo (%)	Effective dose equivalent (μSv)
SXA	Forearm - distal	5	$1-2$	$2-5$	<1
	Forearm ultradistal	40	$1-2$	$2-5$	<1
	Heel	95	$1-2$	$2-5$	<1
DXA	Lumbar - AP	50	$1-1.5$	$5-8$	1
	Lumbar - lateral	90	$2-3$	$5-10$	3
	Proximal - femur	40	$1.5-3$	$5-8$	1
	Forearm	5	1	5	<1
	Total body	20	1	3	3
pDXA	Forearm	5	$1-2$	$4-6$	?
	Calcaneus	95	$1-2$	$4-6$	?
QCT	Spine - trabecular	100	$2-4$	$5-15$	50
	Spine - integral	75	$2-4$	$4-8$	50
pQCT	Radius - trabecular	100	$1-2$	?	1
	Radius - total	40	$1-2$	$2-8$	1
QUS: SOS	Calcaneus/tibia	95/0	$0.3-1.2$	?	0
QUS: BUA	Calcaneus	95	$1.3-3.8$	?	0

Table 2.1: Performance characteristics of various techniques of bone mass measurement at various sites [9]. SXA, single x-ray absorptiometry; DXA, dual x-ray absorptiometry; QCT, quantitative computed tomography; QUS, quantitative ultrasound; BUA, broad-band ultrasound attenuation; SOS, speed of sound; p, dedicated equipment for assessing density at peripheral sites.

absolute threshold of BMD that discriminates absolutely between those who will or will not fracture. Normal BMD does not in itself guarantee that fracture will not occur, only that the risk is decreased.

The gradient of risk depends on the used technique, on the measured site and on the fracture typology. In general, site-specific measurements show the higher gradients of risk for their respective sites. For example, measurements at the hip predict hip fracture with greater power than do measurements at the heel, lumbar spine or forearm [48]. However, measurement of BMD by absorptiometric techniques at more than one site improves the prediction of fractures. Gradients of risk range from 1.5 to 3.0 for each standard deviation decrease BMD. The choice of site for assessment will depend both on the reason for the assessment and on the age of the patient. Since hip fracture is the major concern in the elderly, measurement at that site is preferable since such measurements predict hip fractures most accurately. Thus, measurements made at the wrist, heel, spine or hip may be useful in younger individuals.

Biochemical markers of bone turnover may be divided into two groups, namely markers of bone resorption and markers of bone formation. Fasting urinary calcium excretion (calcium/creatinine ratio) provides a net index of the balance between bone resorption and formation. While breakdown markers may change within 1 or 2 months of starting a bone treatment, several months of treatment are required before any significant change in formation markers becomes apparent. Since BMD changes even more slowly, the rapid changes in markers induced by treatment may be useful in selecting treatment, motivating patients, and monitoring response to treatment (after four to six weeks of therapy). These changes are insufficiently discriminatory, however, to provide a diagnostic test for osteoporosis but are of great value in assessing fracture risk.

Nuclear Magnetic Resonance

Chapter 3

Used NMR techniques

Nuclear magnetic resonance (NMR) provides chemical and physical peculiarities of a system, analyzing its response to a perturbation. In NMR this perturbation is constituted by electromagnetic waves with frequency corresponding to the separation among energy levels of the magnetic system (resonance).

Unlike the other techniques, NMR is able to get information from an under-ensemble of a complex system, tuning in to a select nucleus, provided with spin angular momentum. It determines the total density of a molecule of interest, its structure and dynamics, its interaction with environment, the nature of chemical bonds, etc.. In NMR we can distinguish two important branches of study, *magnetic resonance imaging (MRI)*, it is able to provide NMR parameters for any select volume and, for example in medicine, to point out pathological tissues, while to diagnose their pathological nature it needs *magnetic resonance spectroscopy (MRS)* in vivo which analyzes the structural and biochemical aspects of tissues. MRI is an *emission* rather than a transmission technique where the signal arises from the sample or patient. Problems such as parallax and focus that can and do occur in optical and X-ray methods are inherently small in MRI. A Unlike other emission approaches, such as positron emission tomography or single photon emission computed tomography, the MR signal is intrinsic to the sample or tissue. A MR contrast is based on tissue properties largely at the chemical and biochemical level. The human eye is a remarkable instrument, capable of resolving separations of 0.1 *mm*; like X-ray tomography, conventional MRI has a spatial resolution coarser than that of the human eye with

volume elements of order $(1\ mm)^3$; unlike X-ray CT however, where resolution is limited by the beam collimation, MRI can also achieve a resolution considerably finer than of 0.1 mm (MRI microscopy) by using magnetic fields with frequencies in the interval of Ultra High Frequencies, $(300 - 3000)$ MHz instead of High Frequencies, (3-30) MHz. While it has yet to achieve the resolving power of the optical microscope (about 10 μm), it is non invasive, allowing slices of sample to be examined without physical cutting and without use ionizing radiations.

On the other hand, the magnetic resonance signal from biological samples is relatively weak, resulting in three major consequences: relatively powerful magnets are needed to achieve adequate signal, therefore, the cost of the MR instrument, particularly the magnet, is high; MR instruments are large and difficult to site, due to the large fringe magnetic fields they are potentially hazardous; imaging times are generally long, as the signal must be integrated over long periods to compensate for its small amplitude. Furthermore, the MR signal from tissue is both transient, lasting only a few tens of milliseconds, and refractory, tenths of seconds to seconds are required for the signal to recover adequately for repeated sampling.

Among the various and useful advanced NMR techniques, in this chapter the attention will be focused on two branches evermore objects of study for their considerable investigative potentialities and applied in our experiments, the spectroscopy and diffusion.

By a fast description, the main theoretic concepts of these techniques and of few used pulse sequences will be explained, to understand our work that it will be discussed in the last chapters.

3.1   In vivo magnetic resonance spectroscopy MRS

Magnetic resonance spectroscopy has been applied *in vivo* from the early beginnings of NMR, although dedicated techniques for *in vivo* MRS were not developed until the 1970. *In vivo* MRS has provided a wealth of non-invasive, spectroscopic information on, for instance, energy metabolism, amino acids, intracellular pH and reaction fluxes. It has been used both as a fundamental research technique, as well as a diagnostic tool in medical research.

Following a RF pulse which is calibrated to rotate the equilibrium magnetization $\vec{M}_0$ by 90°, the magnetization precesses about the applied external magnetic field $\vec{B}_0$ and induces an electromotive force (emf) in a receiving coil positioned in the transverse plane. Because of $T_2^\star$ relaxation, the transverse magnetization and consequently the emf will decrease as a function of time. The time-dependence of the emf (or signal intensity) is called the *free induction decay (FID)*. NMR spectrometers separately detect the $x\prime$ and $y\prime$ components of the complex motion of the transverse magnetization (see Fig. 3.1):

$$
\begin{aligned}
\vec{M}_x(t) &= \vec{M}_0 \sin[(\omega_0 - \omega)t + \phi]e^{-t/T_2^\star}, \\
\vec{M}_y(t) &= \vec{M}_0 \cos[(\omega_0 - \omega)t + \phi]e^{-t/T_2^\star},
\end{aligned}
\tag{3.1}
$$

where ϕ is the phase at $t = 0$.
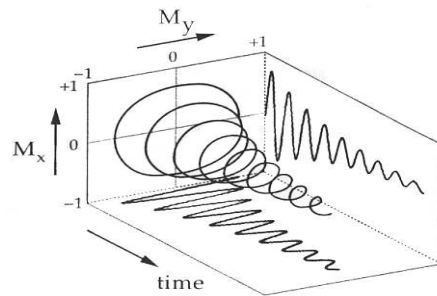
Figure 3.1: The free induction decay of nuclear magnetization following an excitation pulse. The complex three-dimensional FID can be described completely by two projections on the (M_x, t) and (M_y, t) planes, corresponding to the imaginary and real components of the FID, respectively.

$\vec{M}_x(t)$ and $\vec{M}_y(t)$ are normally referred to as the imaginary and real FIDs, respectively. Although the FIDs hold all the relevant information about the nuclear spins, like their resonance frequencies and relative abundance, they are seldom used directly. Normally the time-domain data (i.e. the FID) is converted to frequency-domain (i.e. the spectrum) by a Fourier transformation [49]. In principle it is possible to construct a spectrum from one of the components of the complex FID, therefore, both components are measured, using so-called *quadrature detection* [50]. Fourier transformation of the time domain signals yields

the real and imaginary frequency domain signals given by:

$$R(\omega) = A(\omega)\cos\phi - D(\omega)\sin\phi$$
$$I(\omega) = A(\omega)\sin\phi + D(\omega)\cos\phi,$$

(3.2)

where

$$A(\omega) = \frac{M_0 T_2^\star}{1 + (\omega_0 - \omega)^2 (T_2^\star)^2}$$
$$D(\omega) = \frac{M_0 T_2^\star (\omega_0 - \omega)}{1 + (\omega_0 - \omega)^2 (T_2^\star)^2}.$$

(3.3)

$A(\omega)$ and $D(\omega)$ describe the absorption and dispersion components of a Lorentzian lineshape and are drawn in Fig. 3.2A. The width at half height, $\Delta\nu_{\frac{1}{2}}$, of the absorption component of a Lorentzian lineshape equals $(\pi T_2^\star)^{-1}$. The dispersive component is broader, with a net integrated intensity of zero. Therefore, for the best separation (or resolution) of multiple lines in a NMR spectrum, absorption mode spectra are desired. Pure absorption mode spectra can be obtained by *phasing* the observed, mixed $R(\omega)$ and $I(\omega)$ spectra according to

$$A(\omega) = R(\omega)\cos(\phi - \phi_c) + I(\omega)\sin(\phi - \phi_c)$$
$$D(\omega) = -R(\omega)\sin(\phi - \phi_c) + I(\omega)\cos(\phi - \phi_c).$$

(3.4)

By interactive adjustment of the phase ϕ_c, absorption mode spectra are obtained when $\phi_c = \phi$ (see Fig. 3.2C). When the phase of the signal is not relevant, or if the phase cannot be adjusted, the signal can be presented in absolute value (or magnitude) mode (see Fig. 3.2D):

$$M(\omega) = \sqrt{(R(\omega)^2 + I(\omega)^2}.$$

(3.5)

The resonance frequency of a nucleus not only depends on the gyromagnetic ratio and the external magnetic field, but is also highly sensitive to its chemical environment; this is commonly referred to as the *chemical shift*. The phenomenon of chemical shift is caused by shielding of nuclei from the external magnetic field by electrons surrounding them. When placed in an external magnetic field, the electrons will rotate about $\vec{B}_0$ in an opposite sense to the proton spin precession. Since this precession of electrons involves motion of charge, there will be an associated electron magnetic moment which opposes the primary applied magnetic
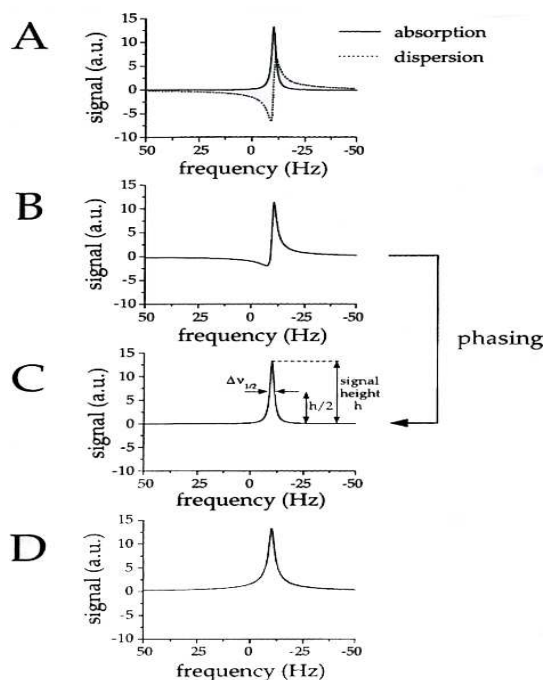
Figure 3.2: Principal components of a NMR spectrum. (A) Complex Fourier transformation of a FID gives rise to Lorentzian absorption and dispersion lineshapes. (B) In general, the initial phase of the FID is non-zero, such that a mixture of absorption and dispersion lineshapes is obtained. The dispersive component can be eliminated by *phasing* the spectrum, such that only the absorption component remains as shown in (C). From the phased spectrum, the frequency ν, the signal height h and linewidth at half height $\Delta\nu_{\frac{1}{2}}$ can be accurately measured. (D) Phase information is completely eliminated when presenting the spectrum in magnitude mode; because the dispersive component is included, the resonance is broader than the pure absorption lineshape.

field $\vec{B}_0$, therefore the electrons will reduce the magnetic field that is sensed by the nucleus, in electronic diamagnetism condition. This effect can be expressed in terms of an effective magnetic field $\vec{B}$ at the nucleus,

$$\vec{B} = \vec{B}_0(1 - \sigma) \tag{3.6}$$

where σ is the shielding constant, a dimensionless number which depends on the chemical environment of the nucleus, in fact, it increases if electronegativity of the bound atom decreases. So, the resonance condition will be:

$$\nu = (\frac{\gamma}{2\pi})B_0(1 - \sigma). \tag{3.7}$$

NMR is, in principle, a quantitative technique, i.e. the signal intensity generated by a certain class of nuclei is linearly proportional to their number in the sample (and consequently the concentration). From equations 3.1 it can be seen that the first point of the FID ($t = 0$), is proportional to the total number of spins M_0. However, after Fourier transformation this quantity is convolved with the $T_2^\star$. Therefore, the peak height cannot be directly used for quantification (only in the rare case when the $T_2^\star$ of all the resonances in the spectrum are identical). However, the total peak area of a particular chemical bond is an accurate measure for the spin density with that kind of bond and can be obtained by (numerical) integration.

Most often chemical shifts are not expressed in units of Hertz but in terms of (dimensionless) parts per million (ppm). According to convention, the chemical shift δ is defined as

$$\delta = \frac{\nu_s - \nu_{ref}}{\nu_{ref}} \times 10^6 \tag{3.8}$$

where ν_s and ν_{ref} are the frequencies of the compound under investigation and a reference compound, respectively. The reference compound should ideally be chemically inert and its chemical shift should be independent of external variables and should produce a strong (singlet) resonance signal well separated from all other resonances. A widely accepted reference compound for ^{1}H and ^{13}C NMR is *tetramethylsilane (TMS)* to which $\delta = 0$ has been assigned. However, the use of TMS is restricted to NMR on compound in organic solvents, it is not found in *in vivo* systems and can therefore never be an internal reference compound. Commonly used internal references are the methyl resonance of

N-acetyl aspartate for ^{1}H MRS of the brain and the phosphocreatine resonance for ^{31}P MRS of brain and muscle.

Apart from resonance frequencies and signal amplitudes, additional features characterize NMR spectra, of which the splitting of resonance lines into several smaller lines is the most pronounced. This phenomenon originates from the fact that nuclei with magnetic moments influence each other either through space (*dipolar coupling*) or through chemical bounds (*scalar coupling*). In a liquid the dipolar interactions normally average out to zero due to rapid tumbling, so that no net interaction between the nuclei remains. However, interactions through chemical bounds (i.e. interaction of nuclear magnetic moment with the electronic magnetic moment of the electrons in the bonds) do not average to zero and give rise to the described features. This interaction is called *indirect nuclear spin-spin (or J) coupling* because it is mediated by electron spins. Consider the spin-spin coupling between a proton and a ^{13}C nucleus. For the ^{1}H nucleus, there are in principle two distinct situations, i.e. the magnetic moment of the scalar coupled ^{13}C nucleus is either parallel or anti-parallel to the applied main magnetic field. The ^{1}H nucleus senses these different states through the spin of electrons, polarized by nuclear spin, in the covalent ^{1}H-^{13}C chemical bond. In general, the spectrum of two coupled spins consists of two doublets, each split by the same amount, one centered at the chemical shift of the first spin and one at the shift of the second. The splitting of the doublets is the scalar coupling, J_{12}, quoted in Hz; the subscripts indicate which spins are involved. The shifts of the two spins are δ_1 and δ_2, and the corresponding Larmor frequencies are:

$$\nu_{0,1} = -\frac{1}{2\pi}\gamma_1(1+\delta_1)B_0$$
$$\nu_{0,2} = -\frac{1}{2\pi}\gamma_2(1+\delta_2)B_0. \tag{3.9}$$

If the two nuclei are of the same type, such a proton, then the two gyromagnetic ratios are equal and so $\nu_{0,1} \approx \nu_{0,2}$; such a two spin system would be described as homonuclear. The opposite case is where the two nuclei are of different types, such as proton and carbon-13; such a spin system is described as heteronuclear. There are four possible combinations of the spin states of two spins and these combinations correspond to four energy levels. Their energies are given in the table

3.1. It is easy to see that these energies have the general form:

number	spin states	M	energy
1	$\alpha\alpha$	1	$+\frac{1}{2}\nu_{0,1}+\frac{1}{2}\nu_{0,2}+\frac{1}{4}J_{12}$
2	$\alpha\beta$	0	$+\frac{1}{2}\nu_{0,1}-\frac{1}{2}\nu_{0,2}-\frac{1}{4}J_{12}$
3	$\beta\alpha$	0	$-\frac{1}{2}\nu_{0,1}+\frac{1}{2}\nu_{0,2}-\frac{1}{4}J_{12}$
4	$\beta\beta$	-1	$-\frac{1}{2}\nu_{0,1}-\frac{1}{2}\nu_{0,2}+\frac{1}{4}J_{12}$

Table 3.1: Energy levels for the possible combinations of the spin states of two spins.

$$E_{m_1 m_2} = m_1 \nu_{0,1} + m_2 \nu_{0,2} + m_1 m_2 J_{12} \qquad (3.10)$$

where m_1 and m_2 are the angular momentum values along the direction of the applied magnetic field I_z for spins 1 and 2, respectively. The selection rule is that $\Delta M = \pm 1$, with $M = m_1 + m_2$. The allowed transitions and their frequencies are given in the table 3.2 and in Fig. 3.3. *In vivo* proton MRS spectra hold information on a considerable

transition	spin states	frequency
$1 \to 2$	$\alpha\alpha \to \alpha\beta$	$-\nu_{0,2} - \frac{1}{2}J_{12}$
$3 \to 4$	$\beta\alpha \to \beta\beta$	$-\nu_{0,2} + \frac{1}{2}J_{12}$
$1 \to 3$	$\alpha\alpha \to \beta\alpha$	$-\nu_{0,1} - \frac{1}{2}J_{12}$
$2 \to 4$	$\alpha\beta \to \beta\beta$	$-\nu_{0,1} + \frac{1}{2}J_{12}$

Table 3.2: Complete set of transitions and their frequencies ($\nu_{ij} = E_j - E_i$) for a two spin system.

amount of metabolites. Even though the MRS spectrum is extremely simplified by a detection limit of concentrations above ~ 1 mM, a typical *in vivo* (short *TE*) proton MRS spectrum still appears complicated by the great diversity of atoms weakly and strongly coupled with ^1H, by many overlapping peaks resonating in a small chemical shift range, by the low spectral resolution of the low field clinical magnets and by the base noise. This complicates unambiguous peaks assignment and quantification. Variation of the echo time is one method to further simply the spectrum at the expense of a reduced signal to noise ratio and
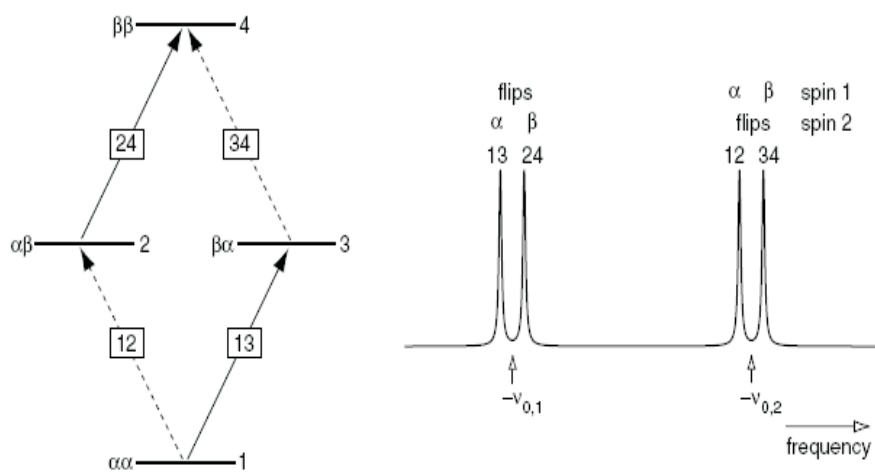
Figure 3.3: On the left, the energy levels of a two-spin system; the arrows show the allowed transitions: solid lines for transitions in which spin 1 flips and dotted for those in which spin 2 flips. On the right, the corresponding spectrum; it is assumed that the Larmor frequency of spin 2 is greater in magnitude than that of spin 1 and that the coupling J_{12}, the splitting of the doublets, is positive but not very great (weakly coupled spins).

loss of many metabolite signals. A more time-efficient alternative can often be provided by spectral editing techniques.

3.2   Diffusion MRI

At microscopic resolutions the water molecules are in constant random motion. The random motion of the molecules in a liquid or gas is a phenomenon termed *Brownian motion* after the Scottish naturalist who first observed the phenomenon in pollen grains suspended in water. Microscopically, these molecules move along arbitrary directions, but macroscopically they flow from a high to low concentration region. With Albert Einstein it became clear that Brownian motion is due to the thermal agitation of the water molecules and that the diffusion is proportional to the temperature and inversely to viscosity of the solution and size of the suspended particle:

$$D = \frac{KT}{6\pi\mu\sigma} \tag{3.11}$$

with K the Boltzmann's constant, T the absolute temperature, μ the viscosity of the solution and σ the radius of the particle [51].

While we are familiar with the diffusion of a substance in another host substance, the physics of diffusion makes no essential distinction between the two. Hence, the theory of diffusion can be applied to the diffusion of a substance in its own medium, for example the diffusion of water in water. This phenomenon is referred to as *self-diffusion* or, with some abuse of terminology, simply diffusion.

Supposing an isotropic medium in which molecules flow, from an macroscopic observation *Adolph Fick* deduced his *first law* that rules the diffusion process [52]:

$$\vec{J} = -D\nabla C \tag{3.12}$$

This equation suggests that the flow density $\vec{J}$ (the number of particles which flow in time and area units) is proportional to the concentration gradient ∇C of the particles by the diffusion coefficient D (m^2/s), supposed constant in the time; the negative sign is to indicate that the flow is from a high to low concentration region. By using the *mass conservation law*

$$\frac{\partial C}{\partial t} + \nabla \cdot \vec{J} = 0 \tag{3.13}$$

it is possible to obtain the *diffusion equation* in an *isotropic* medium and with *time independent* diffusion:

$$\frac{\partial C}{\partial t} = D(\frac{\partial^2 C}{\partial x^2} + \frac{\partial^2 C}{\partial y^2} + \frac{\partial^2 C}{\partial z^2}) \qquad (3.14)$$

Furthermore, in *Einstein's relation*

$$\lambda = \sqrt{2Dt} \qquad (3.15)$$

is possible to notice that, in these conditions, the average displacement λ of the particle is proportional to the square root of diffusion time (*free diffusion regime*).

The diffusion is a tridimensional process. The medium structure or the presence of obstacles, like in biological tissues which have a heterogeneous structure, can produce fluxes with different peculiarities along the various directions; thus, in anisotropic structures is suitable to consider the *diffusion tensor* $\underline{D}$, a symmetric matrix $3x3$:

$$\underline{D} = \left(\begin{array}{ccc} D_{xx} & D_{xy} & D_{xz} \\ D_{yx} & D_{yy} & D_{yz} \\ D_{zx} & D_{zy} & D_{zz} \end{array} \right)$$

The geometric representation of this matrix is the *diffusion ellipsoid* which symbolizes the tridimensional distance covered from the particle in diffusion time t. With a coordinate transformation, it is possible to obtain a diagonal matrix with the D coefficients along the three principal axes of diffusion (D_1, D_2, D_3).

In heterogeneous materials in which restricting, impermeable, or relaxing walls impede the free motion of the particles, like water trapped in a porous system, there is a *restricted diffusion regime* where the average displacement λ of the particle is not more proportional to the square root of diffusion time and $D(t)$ depends also on time [53]. The generic diffusion equation, sometimes referred to as Fick's second law for diffusion is so:

$$\frac{\partial C}{\partial t} = \nabla \cdot (\underline{D}\nabla C). \qquad (3.16)$$

In the common use, two diffusion based techniques are utilized: *diffusion weighted imaging* (*DWI*) is a one-dimensional technique which measures the projection of all molecular motions along one direction,

giving the *apparent diffusion coefficient* (*ADC*); *diffusion tensor imaging* (*DTI*) allows to monitor the diffusion process in the tridimensional space, by measuring DWI in, at least, six directions of the space and then obtaining the *apparent diffusion tensor* $\underline{D}$. The term *apparent* is added because *in vivo* there are other incoherent motions, like blood circulation or respiration, which contribute to the signal attenuation together with molecular diffusion and that MRI techniques are not able to distinguish them.

The basic idea of magnetic resonance diffusion imaging is to measure the diffusion of water molecules and use these measurements to probe the underlying structure of the tissue. Owing to the microscopic length scale of diffusion in biological tissues, diffusion imaging can reveal histological architecture irresolvable by conventional magnetic resonance imaging methods. In clinical diagnostics are ever more realized imagines contrasted in diffusion, by the *b-factor*, along one direction and *parametric maps* where every pixel is proportional to a parameter connected to tensor $\underline{D}$ of the corresponding voxel, like the *fractional anisotropy* (*FA*)

$$FA = \frac{\sqrt{3[(D_1 - \overline{D})^2 + (D_2 - \overline{D})^2 + (D_3 - \overline{D})^2]}}{\sqrt{2(D_1^2 + D_2^2 + D_3^2)}}, \tag{3.17}$$

where $\overline{D} = (D_1 + D_2 + D_3)/3$, which measures the eccentricity of the diffusion ellipsoid and is zero for an isotropic system and 1 for maximum anisotropy, the *mean diffusivity* (equal to $\frac{Tr(\underline{D})}{3}$) which allows to monitor the mean displacement in the t time, and the D coefficient along the principal axis of higher diffusion to identify oriented structures like muscular fibers or nervous beams (*fiber-tract mapping* and *field mapping*, see Fig. 3.4).

3.3   Used sequences

        In this section will be discussed three sequences used in the experiments, as described in the last chapter.

- *The Spin Echo.*
  Magnetic field inhomogeneities in samples arise from several factors: imperfections in the uniformity of the imaging magnet, variations in tissue magnetization, and molecular scale magnetic field
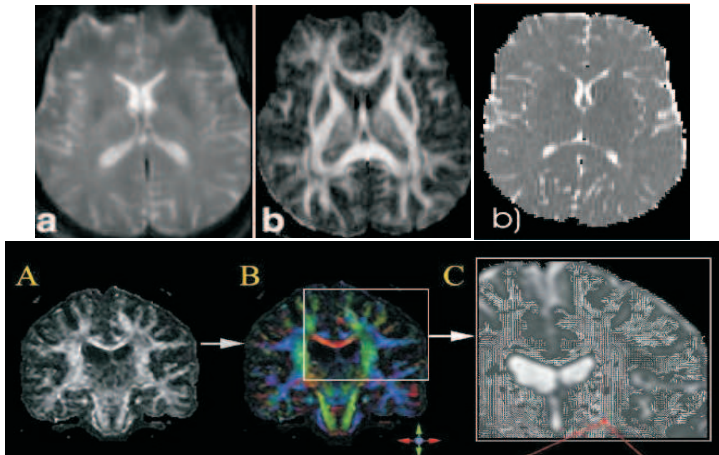
Figure 3.4: The picture **a** is an image of an adult brain section, obtained with MRI techniques and contrasted with T_2 parameter; the pictures **b** and b) are the corresponding fractional and mean diffusivity maps. The picture A is the fractional map of another brain section, in this the strongly anisotropic white matter is discriminated from the isotropic grey matter; by use a colored codex with red corresponding to right-left direction, green to down-up and blue to forward-backward, is possible to characterize the directions of the white matter (B, fiber-tract mapping); it is possible also to visualize the local orientations by vectors (C, field mapping).

variations. The first is, of course, an issue of instrumentation and is largely a source of artifactual signal intensity-much effort has been extended to minimizing its impact, both by improving the magnet technology and by devising data acquisition schemes to reduce its effects on MR images, thus, variations in main magnetic field are no longer a dominant source of transverse decay; 1 or 2 ppm is a typical homogeneity over a 24-cm (head size) volume in an empty magnet. The second factor is related more strongly to the tissue sample and is, thus, of more clinical interest. Any object, when subjected to a magnetic field, will magnetize to a degree slightly more than (paramagnetic) or less than (diamagnetic) the applied field. The relationship between the field experienced within a sample and the applied field is known as the *magnetic susceptibility*, denoted by χ. Susceptibility is calculated as the ratio of the internal magnetic field to the applied field. Most body tissues are slightly diamagnetic, thus, at the interface between tissues, a relatively large gradient in the magnet field may exist and, as a consequence, proton spins in this region will dephase very rapidly as compared to spins within homogeneous tissue. The final major factor determining transverse relaxation rates is magnetic field variation on the molecular, or atomic, size scale. The magnetic field experienced by a proton (and thus its resonant frequency) is strongly influenced by the presence of other diamagnetic or paramagnetic nuclei, such as other protons. Generally, it is the transverse decay rate from these interactions that yields the greatest clinical information, as it relates strongly to changes in intracellular structure chemical environment. However, biological tissues such as human heads do not necessarily magnetize evenly and therefore introduce field inhomogeneity to a greater or lesser degree. All of this would render MRI a relatively limited modality, but Erwin Hahn discovered in 1950 a trick, the spin echo. Not taking into account the spin diffusion effects (see the subsection 3.3.1), this trick effectively eliminates the effects of the local magnetic field heterogeneities due to the static field and to the susceptibility mismatch between tissues ($\gamma\Delta B$) dephasing on the signal intensity.

Although spin echoes are formed with virtually any combination of RF pulse amplitudes, they are largest and easiest to understand as the combination of a 90° excitation pulse followed by a 180° echo-forming pulse. Imagining the combined signal from a sample in a spatially inhomogeneous magnetic field, initially, following a 90° excitation pulse, the spins are in-phase and their summed magnetization results in a macroscopically observable MR signal (see Fig. 3.5A). Because the spin frequency may differ with location (because of magnetic field inhomogeneities) the MR signal from the summed effects of all spins will decay rapidly (at the rate $T_2^\star$) as the spins acquire a phase difference. Application of a 180°y RF pulse reverses the relative phases of the spins so that those in a higher magnetic field have a phase lag compared to those in a lower field. Because the spin frequency has not changed (it is primarily a function of spin location) the spins come back into phase and the MR signal is reformed as a *spin echo.*

Figure 3.6 shows the MR signal as a function of time for spin echo sequences. As can be seen readily, the spin echo occurs at a time TE equals to twice the time that elapses between 90° and 180° pulses.

The most important feature of the spin echo is, therefore, that its amplitude does not depend directly on the field homogeneity, i.e., the echo envelope decay is dominated by T_2 relaxation. As TE is increased, the T_2 differences in tissues will become apparent as the signal from a tissue with a short T_2 will be less than that of a tissue with a long T_2.

The imaging spin echo sequence is illustrated in the Figure 3.7. It is possible to acquire, with one sequence, two echoes at two different TEs adding another 180° soft pulse and acquiring also the relative signal.

- *Fast low angle shot (FLASH).*
  MRI was not, until recently, an effective technique for the study of dynamic processes, the normal physiological motion from respiration, vascular pulsation, peristalsis, or simply gross subject motion results in severe degradation of the MR images; artifacts from moving tissues degrade the signal even from nonmoving tissues. This
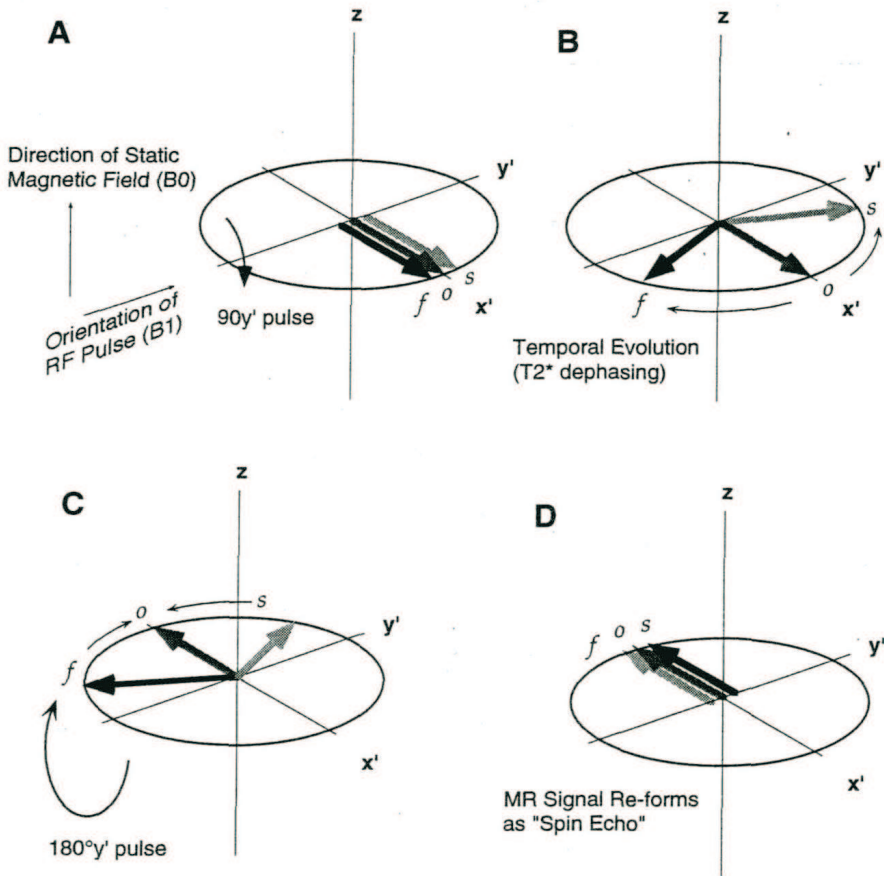
Figure 3.5: Rotating frame depiction of the spin echo. (**A**) After an initial excitation pulse, all spins are precessing in phase. (**B**) Variations in magnetic field strength, however, cause the angular velocity to differ with position in the field. With respect to a reference location (o) precessing at the same rate as the reference frame, some spins may precess faster (f) or slower (s). With respect to the rotating reference frame they appear to advance or fall behind spins precessing at the reference rate. Over time, the difference in frequency causes the phases of the spins to disperse and the total MR signal from all spins to decay at the rate $T_2^\star$. (**C**) To form a spin echo, a second RF pulse is applied with a duration and intensity sufficient to impart a $180°$ spin flip. As a result, the relative phases of the spins are reversed. (**D**) With time, the faster precessing spins catch up, whereas the slower precessing spins fail in phase. The result is that the signal is reformed as a *spin echo*.

Figure 3.6: The MR signal in a spin echo sequence.

Figure 3.7: Imaging SE sequence. The selection gradients are applied during the 90° and 180° soft pulses, the phase and frequency encoding gradients between the 90° and 180° pulses and another frequency encoding gradient is applied during the signal acquisition to phase the spins.
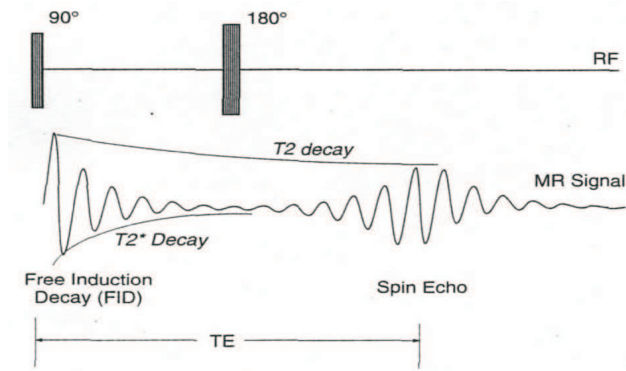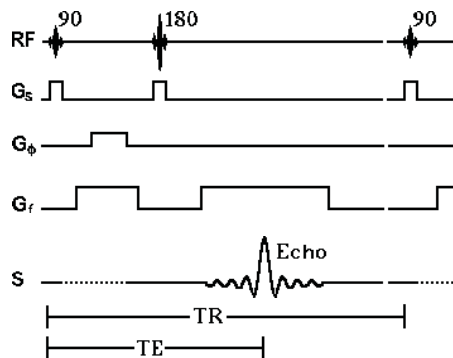
limitation was recognized by MR investigators and many of the early papers on reductions in imaging time specifically addressed the use of fast MRI to observe organ function. A general approach to imaging speed is called *low flip angle* or FLASH (fast low angle shot) imaging, which allows the use of shorter TRs by using the longitudinal magnetization more efficiently.

Decreasing the TR is an obvious means of reducing the overall scan time, and doing so has a variety of consequences, both positive and negative. If the excitation pulse is repeated before complete longitudinal remagnetization (i.e., with a TR short compared to T_1 which is relatively long), the strength of the MR signal following the next pulse will be reduced. Tissues differ greatly in their T_1 recovery times and will therefore produce differing signal intensities: tissues with shorter T_1 times will yield signals stronger than those with long T_1's. This principle, in fact, forms the basis of T_1 contrast in MR imaging. The T_1 contrast is minimized when TR is long compared to T_1. The T_1 contrast is not always desirable; in particular, it compromises the usable contrast of T_2-weighted images. Beyond the shorter imaging time, and the increase in T_1 contrast, decreasing the TR also results in an overall loss in signal and thus in the signal to noise ratio (SNR). There will also be a decrease in volume coverage: multislice MR uses the time available between repetitions on a single slice to collect data from other slices. As the TR is reduced, the time available for multislice imaging is also decreased and fewer slices may be collected.

The RF flip angle is defined by the extent to which longitudinal magnetization becomes rotated into the transverse plane. FLASH is representative of the *gradient echo* family of scanning methods, which use a carefully timed activity in the imaging gradients, instead of a 180° pulse, in order to recover the MR signal (see Fig. 3.8). It uses also RF flip angles of less than 90° as excitation pulses. Remembering that the strength of the MR signal is reflected in the extent of the total magnetization in the transverse planet, as the RF flip angle α increases, so does the signal strength according to the simple formula: $SI = A\sin(\alpha)$, where A is simply an arbitrary constant reflecting all other factors. However, with small flip an-
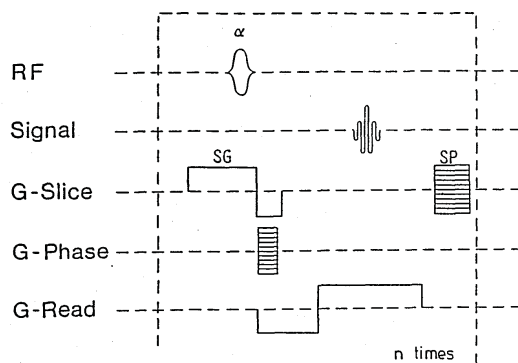
Figure 3.8: FLASH sequence. This method avoids image artifacts which may be caused by transverse magnetization remaining at the end of a TR period of a partial experiment by applying an additional spoiler slice gradient pulse (SP) after the detection of a gradient echo (Signal) and before the application of the radio frequency pulse (RF) of the following partial experiment.

gles, less time is required for the protons to remagnetize after the excitation pulse. This allows for adequate longitudinal recovery, and therefore adequate signal, at shorter TR (see Fig. 3.9 and 3.10). Differences in longitudinal recovery between tissues represent a T_1 contrast. As a consequence, in FLASH imaging, shorter TRs may be used to achieve images without a T_1 contrast. In the very short TR regime, with TR less than one-tenth of T_1, a 20° flip angle yields several times the signal intensity of a 90° flip angle. It is also to note, on the other hand, that the maximum signal strengths can be achieved only with a 90° flip angle and at long TR. The effect of TE is here to control the $T_2^\star$ contrast.

The advantages of shallow flip angle excitation cannot be realized when 180° RF pulses are used to form spin echoes. The FLASH method works, in part, because the longitudinal magnetization is relatively undisturbed by a shallow excitation pulse. In contrast, one effect of a 180° pulse is to invert the longitudinal magnetization. So, the use of a shallow excitation flip angle in combination with 180° pulses actually prolongs the time required for signal recovery because the longitudinal magnetization must now recover,
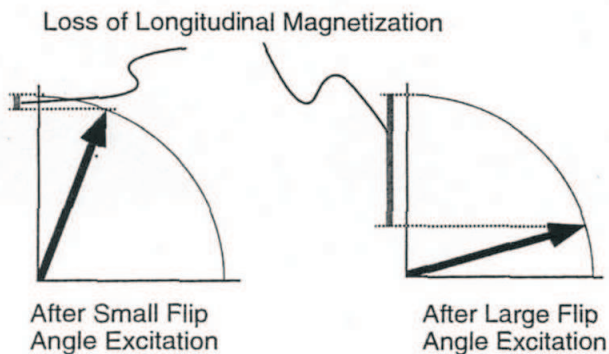
Figure 3.9: When small flip angles are used for excitation, there is relatively little loss of longitudinal magnetization (shown vertically) and only this small amount must be recovered during the TR period, as a result the tissue remagnetize more rapidly.
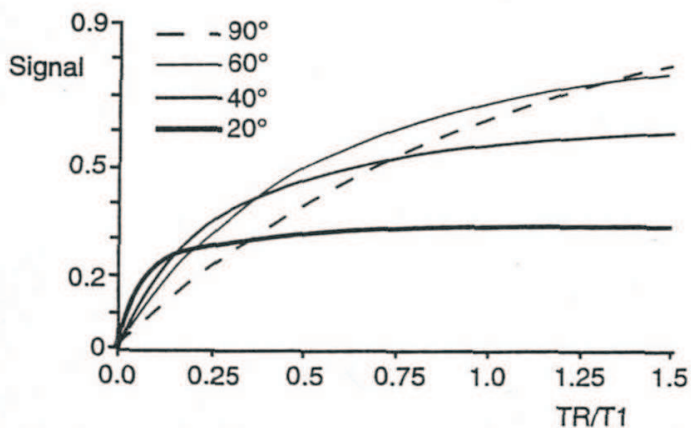
Figure 3.10: For long repetition times, larger flip angles produce a greater signal. As the TR is decreased, however, the shallow flip angles yield more signal. This is because, at shorter TRs, the magnetization does not have the time to recover fully between repeated RF excitation pulses.

not from zero, but from a negative initial value. Omitting the 180°
pulse, the MR signal decays at the rate $T_2^\star$.

FLASH, as most of the popular MR imaging strategies, requires
repeated excitations, any excitation in fact allows to acquire a
line of the **k** space; in this technique, steps are taken to destroy
any residual transverse magnetization prior to each excitatory RF
pulse. In this way, only longitudinal magnetization is incorporated
into the *steady state*. In FLASH, after the signal is collected in the
form of a gradient echo, a gradient pulse called *spoiler* is used to
destroy any remaining transverse magnetization. From there, the
magnetization recovers longitudinally at the tissue T_1 rate and the
degree of recovery is the same with each cycle and thus reaches a
steady state. The short TR in FLASH necessitates the use of a
spoiler; without it, some transverse magnetization would remain
at the beginning of the next RF pulse.

- *Diffusion weighted Segmented Echo-Planar Imaging (EPI).*
  An altogether different approach to scan time reduction is afforded
  by echo-planar imaging (EPI) as put forward by Mansfield (1977).
  In EPI all of the spatial encoding is performed following a single ex-
  citation pulse (i.e., the TR is infinite, see Fig. 3.11). To do so, the

Figure 3.11: EPI sequence.

gradient amplitude is increased up to its maximum practical limit
to minimize the time required to detect the position-dependent
frequency differences. Brief pulses of the phase-encoding gradient
are made during the readout period to encode the signal. As sug-
gested earlier, this requires rather large gradient amplitudes and
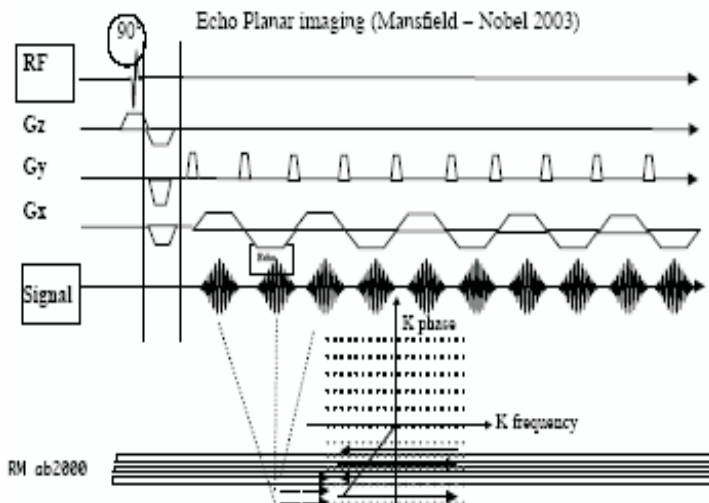rapid gradient switching to yield adequate resolution (gradient-
time product) in the brief period that the MR signal is available.
Rapid switching of the gradient field results in a time-varying mag-
netic field of significant magnitude. Because the human body is a
fair conductor, this varying magnetic field can cause current flows
in the body, resulting ultimately in neural stimulation (Reilly,
1989; Cohen et al., 1990; Budinger et al., 1991). It is possible to
build safe whole body gradient sets with amplitudes to 2.5 G/cm
and 0.5 msec switching times and head gradients to about 5 G/cm
with 0.25 msec switching times. Therefore, complete MR images
may be acquired in as little as 20 msec with EPI, with spatial res-
olution on the order of 1 mm. Compared to FLASH-style imaging,
EPI has much more flexible contrast, as its imaging speed depends
on modifications to the spatial-encoding procedure, not to the RF
pulse sequence that determines the signal behavior. In practice,
this means that it is practical with EPI to obtain images with ei-
ther RF spin echoes, or with gradient echoes, so that the degree of
T_2 and $T_2^\star$ weighting may be varied freely and somewhat indepen-
dently. It is also an order of magnitude or so faster and recovers
the MR signal more efficiently than FLASH scanning.
One of the largest problems in using echo planar imaging is the
level of image distortion due to susceptibility, that is observed.
This can make some structures hard to detect using EPI. In or-
der to improve the quality images, an approach that can be taken
is to use a technique which is a hybrid of EPI and 2DFT, called
interleaved or segmented EPI. This technique acquires the image
in two or more FIDs, thereby trading some of the speed of EPI to
gain some of the image quality of 2DFT. Interleaved EPI was pro-
posed by McKinnon, as a way of implementing EPI on a standard
clinical scanner, which did not have the necessary fast ramping
gradients. It also has benefits however for scanners which can

carry out conventional EPI, ranging from reducing distortion, improving linewidth, to increasing signal to noise.

Interleaved EPI acquires all the data points required to make up the image in several FIDs. The easiest way to picture how this is done is to look at the **k**-space coverage diagram (see Fig. 3.12) for a two shot interleaved EPI sequence (see Fig. 3.13). The first interleave covers the whole of **k**-space in alternate lines, and then the second pass fills in the lines between. The same principle holds for any number of interleaves, up until the technique essentially becomes a 2DFT experiment. The technique is some-
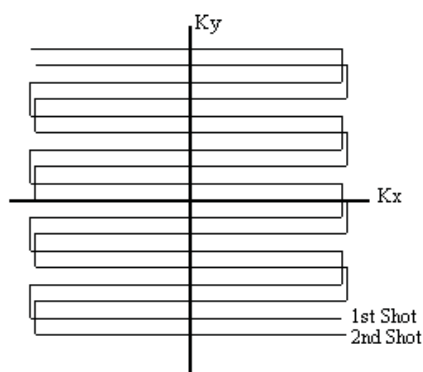
Figure 3.12: **k**-space coverage diagram for a two shot interleaved EPI sequence.

times referred to as segmented EPI, since **k**-space is covered in two or more segments. It seems appropriate to refer to the kind of technique shown in Figure 3.12 as interleaved EPI, since the two shots are indeed interleaved on reconstruction, and to refer to other multi-shot techniques as segmented EPI. The parameter *EPI Factor* is used to specify the number of **k**-space profiles collected per excitation.

In order to measure the rate of molecular flow, some kind of phase encoding that is flow sensitive can be applied. This is done by applying a magnetic field gradient along the direction in which flow is to be measured. A large gradient dephases the spins depending on their position along the gradient. This gradient is then reversed, which will completely rephase any stationary spins. Spins
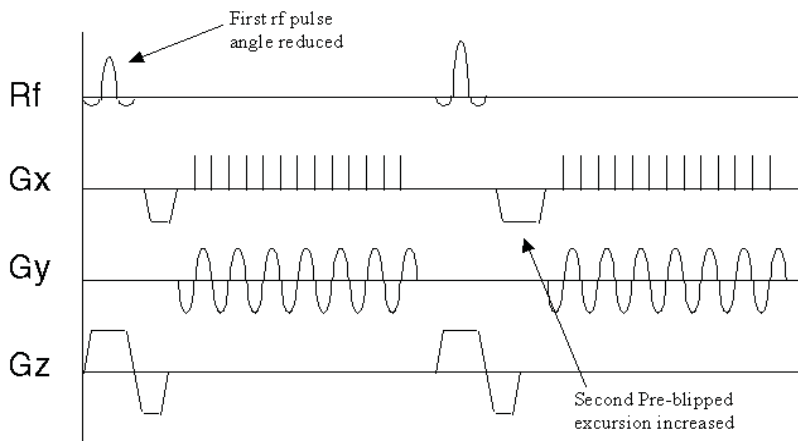
Figure 3.13: Pulse sequence diagram for a two shot interleaved EPI experiment.

that have moved however will not be completely rephased because such movement alters the magnetic field experienced by the spins so that the phase acquired during the refocusing gradient is not exactly opposite to that acquired during the defocusing gradient. (see Fig. 3.14). If the flow is coherent within a voxel, when the spins are imaged the phase difference can be calculated, and by varying the time between the forward and reverse gradients the flow can be calculated. Diffusion is measured in a similar way, but as diffusion is a random process we expect to see a smooth attenuation of the intensity of the refocused signal as the diffusion contribution increases, following the equation:

$$S = S_0 e^{-bADC}, \tag{3.18}$$

where S_0 is the signal intensity in the absence of a gradient, ADC is the apparent diffusion coefficient averaged on TE time, which generally decreases as the molecular mass increases, and the $b-factor$ is the parameter by which the images are contrasted in diffusion; relaxation has been ignored. Following the equation:

$$b = \gamma^2 g^2 \delta^2 (\Delta - \delta/3), \tag{3.19}$$

the $b-factor$ depends on the time between the two gradient pulses (Δ), on the duration (δ) and strength (g) of the gradient pulses
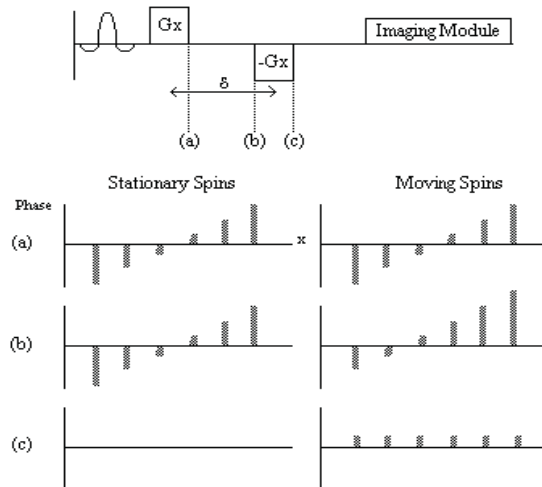
Figure 3.14: Flow encoded imaging. (a) Spins are dephased with a gradient in the x direction. (b) After a time δ the gradient is applied in the opposite direction. (c) Spins that are stationary will be completely rephased, whereas spins that have moved along x in the time δ will be left with a residual phase shift.

and on the nuclear gyromagnetic factor of interest (γ). Indeed, for a given pair of gradient pulses spins diffuse during the delay between the two pulses which determines the attenuation of the echo. Moreover, the stronger the gradient the more rapidly the phase varies across the sample and thus the more rapidly the echo will be attenuated.

3.3.1 The internal gradient (G_i)

In spongy bone, the susceptibility mismatch between the solid matrix and interstitial liquid bone marrow ($\Delta\chi = \chi_{marrow} - \chi_{bone} \simeq 3 * 10^{-6} \gg |\Delta\chi|_{brain}$) [54] generates internal gradients with magnitude depending on the geometry and orientation of the trabeculae with respect to the static magnetic field direction and scales with the magnetic field strength. The interface separating two materials of different magnetic susceptibility gives rise to an induced local magnetic field B_{ind} which produces heterogeneities in the static magnetic field B_0 generating the so called internal gradient G_i. For surfaces with complex geome-

tries the calculation of B_{ind} is difficult but it is possible to demonstrate the following relation [54]:

$$B_{ind} \propto \Delta\chi B_0 A cos(\alpha), \tag{3.20}$$

where $\Delta\chi$ is the susceptibility difference between the two materials, A the surface separating the materials and α the angle between the static field and a vector at a 90° angle to the surface. The signal loss given at a TE for a gradient echo experiment can be described by:

$$S(TE) \propto S(0)exp\left(-\frac{TE}{T_2^\star}\right), \tag{3.21}$$

with $T_2^\star$ (see eqn. 3.22) depending on the local magnetic field heterogeneities $\gamma\Delta B$ (due to the static field and G_i) and on T_2 spin-spin relaxation time or true T_2 (linked to the intrinsic coherence loss of the spin system):

$$\frac{1}{T_2^\star} = \frac{1}{T_2} + \gamma\Delta B. \tag{3.22}$$

The use of GE-type sequence ensures the so called *static dephasing regime*, that is when the NMR signal decay due to the magnetic moment dephasing resulting from the local differences in the nuclear frequencies occurs faster than the diffusion phenomena and which implies that diffusion effects are negligible [55]. Vice-versa by using SE-type sequence [56] the diffusion of bone marrow molecules in the local magnetic field gradient becomes an important factor; molecules interchange their positions resulting in a small phase difference between their nuclear magnetic moments and this generates an irreversible signal loss [57]. In this case of signal loss, as function of the TE in a SE experiment:

$$S(TE) \propto exp(-\frac{TE}{T_2}) = exp\left[-\left(\frac{TE}{T_2^{true}}\right) - \frac{1}{12}(\gamma G_i * TE)^2 ADC * TE\right], \tag{3.23}$$

where ADC is the apparent diffusion coefficient and:

$$\frac{1}{T_2} = \frac{1}{T_2^{true}} + \frac{1}{12}(\gamma G_i * TE)^2 ADC. \tag{3.24}$$

Thus, in SE measurements the additional decay of the echo amplitude is due to diffusion of fluid molecules in the local magnetic field gradient

G_i. As a consequence, bone marrow T_2 and $T_2^\star$ relaxation times are directly related to the density of the surrounding solid-state network and its spatial geometry. The resulting more rapid loss of coherence becomes greater as long as the concentration of solid network in the surrounding homogeneous liquid spin system increases. On the contrary the increase in trabecular spacing reduces the spatial field inhomogeneity and thus prolongs the spin-spin relaxation due to the additional decay of the echo amplitude and $T_2^\star$. This behavior is substantial for $T_2^\star$ and reduced for T_2. In systems like spongy bone, it is possible to quantify mean G_i from the attenuation of the SE signal as a function of different TEs. Furthermore, a measure of the apparent diffusion coefficient (ADC) and/or a measure of T_2^{true} are needed to reduce the number of unknown parameters and improve the fit quality. In all in vitro and in vivo experiments reported in this work, the ADC was measured and inserted in equation 3.24 to extract G_i and T_2^{true} using a fitting procedure.

Experimental results and new perspectives

Chapter 4

^{1}H NMR Spectroscopy of bone marrow

4.1 State of the art

Lipids are increasingly believed to play an important role in the pathogenesis of osteoporosis [58] and other conditions, such as hypertension and coronary artery disease [59,60]. Epidemiologically, osteoporotic postmenopausal women are at significantly greater risk for cardiovascular disease than age-matched controls [61], with higher serum lipid levels having been identified in both diseases [62]. In adult bone marrow, adipocytes are the most abundant stromal cell phenotype and are believed to influence both hematopoiesis and osteogenesis [63]. Adipocytes and osteoblasts share a common progenitor (mesenchymal stem cells) in the bone marrow, such that increased adipogenesis may be associated with decreased osteoblastogenesis. Accumulating evidence suggests that a reciprocal relationship may exist between these two processes [64]. However, the molecular mechanism underlying this reciprocal relationship is not yet fully understood.

Under high-resolution analytical conditions, signals from protons adjacent to double bonds are easily resolved, and it is a relatively simple matter to assess fat composition by ^{1}H NMR spectroscopy. At 7 T, for example, 10 resonances can be resolved (see Table 4.1). Six resonances contribute equivalent information about triglyceride composition (see Fig. 4.1): the CH_3 methyl protons (at ∼0.90 ppm), the CH_2 methylene protons α- (at ∼2.25 ppm) and β- (at ∼1.59 ppm) to

the carbonyl, and the glycerol backbone CH and CH_2 protons. Hence, there are only four additional informative resonances to consider: 1) bulk CH_2 methylene protons (at ~1.3 ppm); 2) allylic CH_2 protons, α-to a double bond, at 2.03 ppm; 3) diallylic (also called bis-allylic) CH_2 protons at 2.77 ppm; and 4) olefinic, double bond $-CH=CH-$ protons at 5.31 ppm.   Extension of this analysis method to low magnetic fields

Signal	Chemical shift (ppm)	Functional group
1	0.82-0.94	$-CH_3$ (terminal methyl protons (saturated, oleic and linoleic))
2	0.94-1.03	$-CH_3$ (terminal methyl protons (linolenic))
3	1.20-1.43	$-(CH_2)_n-$ (methylene protons (saturated))
4	1.55-1.69	$-OCO-CH_2-CH_2-$ (β-methylene protons (carbonyl))
5	1.93-2.13	$-CH_2-CH=CH-$ (allyl methylene protons)
6	2.25-2.36	$-OCO-CH_2-$ (α-methylene protons)
7	2.73-2.87	$=HC-CH_2-CH=$ (divinyl methylene protons)
8	4.10-4.35	$-CH_2OCOR$ (methylene protons (glyceryl))
9	5.23-5.29	CHOCOR (proton on carbon atom 2 of glyceryl group)
10	5.29-5.43	$-CH=CH-$ (olefinic protons)

Table 4.1: ^1H NMR spectral peaks assignment of bone marrow fat: chemical shift ranges and functional groups [65–67].

gives rise to the overlapping lipid peaks, due to the worst chemical shift resolution.

At 1.5 or 3 T, only four resonances can be resolved by the application of prior knowledge (labeled 1, 3, 5, 10 in Table 4.1, see Fig. 4.2). Water (4.65 ppm) and lipid (1.3 ppm) peak amplitudes can be measured to determine marrow fat content Mfc, which is defined as the relative fat signal amplitude in terms of a percentage of total signal amplitude (water and fat) and calculated according to the following equation:

$$Mfc = \frac{I_{fat}}{I_{fat} + I_{wat}} \cdot 100 \qquad (4.1)$$

where I_{fat} and I_{wat} are the peak amplitudes of fat and water, respectively. Many ^1H MR spectroscopic studies focused to measure the Mfc of the lumbar spine and to its correlation with bone mineral density
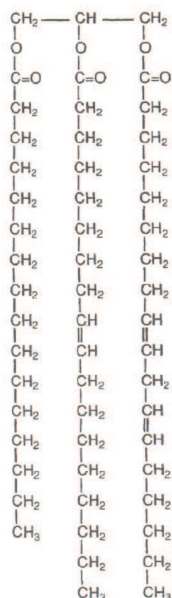
Figure 4.1: Chemical structure of a triglyceride with three different fatty acids.

and age of the subjects: a mild significant negative correlation or no correlation was observed between $T\text{-}score$ or BMD and vertebral Mfc [68–72] and a significant positive correlation between age and vertebral Mfc [72,73]. Moreover, Yeung *et al* and Griffith *et al* obtained a significantly higher vertebral marrow fat content for the osteoporotic group than for the normal bone density group [68, 71], whereas Schellinger *et al* observed that in an abnormal group, which consisted of subjects with MR imaging evidence of vertebral bone weakness, the Mfc was higher than that in a control subject group, for the same age decade [70, 73]. The relation between Mfc and vertebral bone weakness could be explained by three considerations [73]. First, trabecular rarefication with thinning, which is commonly reported as the main cause of bone weakness in osteoporosis, results in open spaces among the trabecular mesh and some have suggested that there is compensatory filling of these spaces with fatty marrow [74–81]. Therefore, increased vertebral fat content could mirror bone loss. Second, marrow composition may affect elasticity of the bone superstructure [82]; red marrow is said to
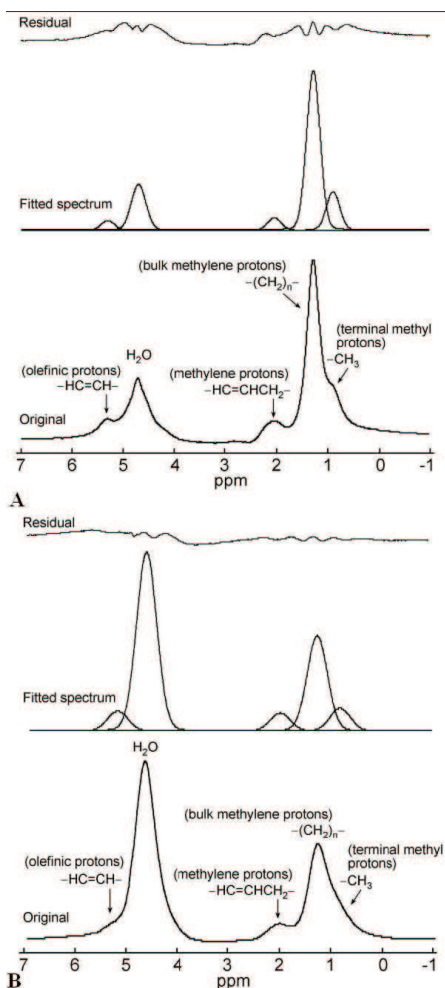
Figure 4.2: ^{1}H-MRS performed on the L3 vertebral body of a 72-year-old woman with osteoporosis ($T\text{-}score = 2.8$) and a 40-year-old premenopausal woman. **A**: Spectrum (bottom trace) acquired from a woman with osteoporosis shows a relatively intense lipid peak from bulk methylene protons compared to the water peak (4.65 ppm), indicating increased marrow fat content. The middle trace shows the fitted spectrum using prior knowledge, and the top trace is the residual spectrum. **B**: Spectrum acquired from a premenopausal woman shows a relatively intense water peak compared to bulk methylene protons [68].

contribute to hydrostatic strengthening, whereas fatty marrow is associated with greater compressibility of vertebrae. Fatty marrow would cause hydrostatic weakening of a vertebra. Third, bone marrow relates to the regulation of bone turnover. Nuttal *et al* [83] have reported that bone-marrow stromal cells can undergo adipogenesis or osteoblastogenesis. There is a reciprocal relationship between adipocytes and osteoblast phenotypes; excessive expression of one versus the other may have significance in the context of osteoporosis. Thus, a decrease in osteoblastogenesis in bone marrow may result in increased adipogenesis. Predominance of fatty marrow therefore could be a result of increased adipogenesis and have a negative effect on osteogenesis. They therefore recognized a therapeutic opportunity for treatment of bone loss by pharmacologic inhibition of bone marrow fat.

The purpose of our study was to investigate the marrow fat content and its correlation with *T-score* parameter and age of the subjects, in an anatomical region rich of yellow marrow, such as the calcaneus.

4.2   Materials and methods

Twelve postmenopausal healthy females (mean age 59 ± 5 years and mean *T-score* -1.20 ± 0.52), thirty-seven postmenopausal osteopenic females (mean age 62 ± 7 years and mean *T-score* -2.66 ± 0.39) and twenty-eight postmenopausal osteoporotic females (mean age 66 ± 6 years and mean *T-score* -3.92 ± 0.49), participated to this study. The inclusion criteria were 1) any preexisting bone disease (such as tumor, metastases, or metabolic disorder), 2) absence of documented calcaneal abnormality, 3) absence of drug therapy known to affect bone density, and 4) absence of implants contraindicated for MR examination. Six premenopausal females (mean age 29 ± 3 years) were also recruited as young control subjects. The ethics committee of our institution (Santa Lucia Foundation) approved the study and written consent was obtained from all subjects prior to examination. The normal, osteopenic or osteoporotic status of each postmenopausal subject was assessed with QCT lumbar vertebral BMD measurements according to the criteria described in section 2.3 (normal with *T-score* ≥ -1.8, osteopenia with $-3.3 < T$-

$score < -1.8$, osteoporosis with T-$score \leq -3.3$).

The images were obtained by using a circular polarized volume head-coil for radiofrequency (RF) transmission and reception, on a Siemens Allegra MR-scanner operating at 3.0 T (Siemens Medical System, Erlangen, Germany). Control imaging experiments were performed on a phantom constituted by water (1 l), salt (5 g), Agar (15 g), Cr (7.06 g) and Lac (3.6 g) to check the RF head coils. Each volunteer was placed in the supine position with the right foot placed in the RF coil, as shown from the axial localizer image reported in Fig. 4.3.

Single voxel spectroscopy with TE=22 ms, TR=5 s, NS=32
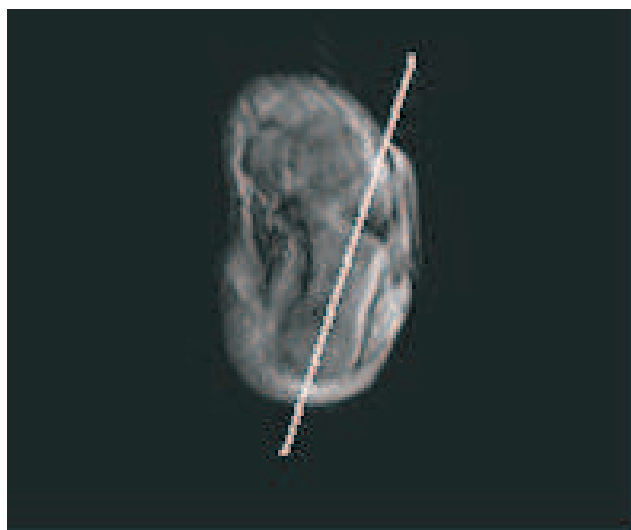
Figure 4.3: Axial localizer of the right foot with the white line indicating location of oblique sagittal FLASH and MCSE images in the calcaneus. See the next chapters.

was used to obtain bone marrow proton spectra. The voxel size of 15x15x15 mm was positioned at the center of the calcaneus. All spectra were analyzed by LCModel method. The LCModel method analyzes an in vivo spectrum as a Linear Combination of Model in vitro spectra from individual metabolite solutions, like for the analysis of the brain metabolites, or it simulates the metabolites of interest, like for the analysis of lipid spectra (our case) [84]. A nearly model-free constrained regularization method automatically accounts for the baseline

and lineshape in vivo without imposing a restrictive parameterized form on them. LCModel is automatic (non-interactive) with no subjective input. Approximately maximum-likelihood estimates of the metabolite absolute concentrations and their uncertainties (Cramér-Rao lower bounds) are obtained.

As is possible to observe in Fig. 4.4, the spectra from yellow bone marrow of calcaneus, but also of femur and other locations in the limbs of adults, are dominated from signals of fatty acids (for hematopoietic marrow like in the pelvis and in the spine, instead, considerable water signals occur in the spectra, see Fig. 4.2) because this type of marrow contains fat cells filled with triglycerides mainly. For lipid spectra,

Conc.	%SD	/Water	Metabolite
6.45E+05	0%	6.565	L20+L13+L09
5.92E+05	0%	6.019	Lip09+Lip13
5.65E+05	0%	5.747	Lip13
2.67E+04	3%	0.272	Lip09
5.37E+04	1%	0.547	Lip20
2.98E+04	1%	0.303	Lip53
1.28E+05	0%	1.303	Lip53+Water
9.83E+04	1%	1.000	Water

LCModel (Version 6.2-0) Copyright: S.W. Provencher. Ref.: Magn. Reson. Med. 30:672-679 (1993).
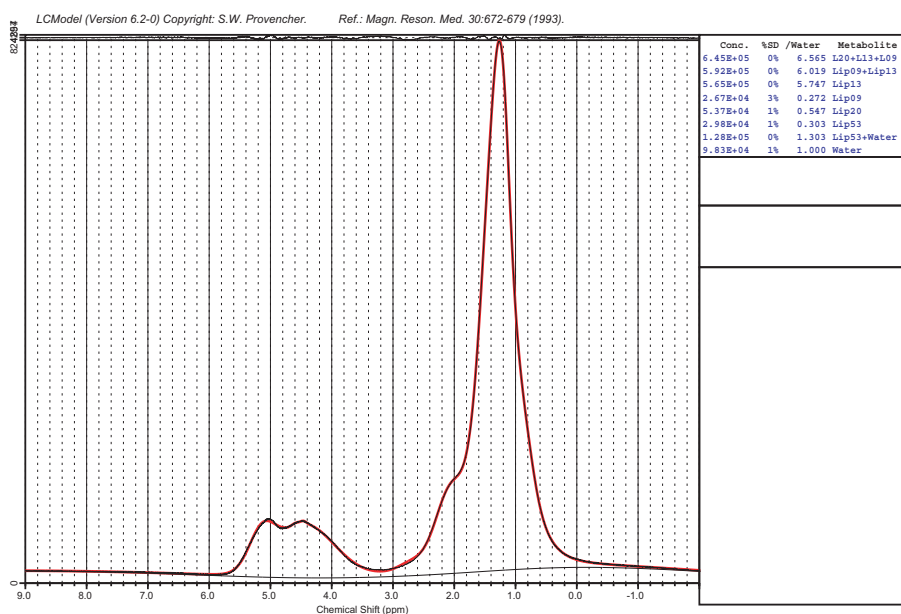
Figure 4.4: Localized spectrum in the bone marrow of the calcaneus of a 66-years-old women with *T-score* -2.5, acquired at 3.0 T and analyzed by LCModel method. The metabolite absolute concentrations, their uncertainties and their ratios with water absolute concentration are reported for every metabolite on the right side. The residuals (calculated from the data values minus the fit values), are plotted at the top of the plot.

LCModel measures the concentrations of the four lipid peaks (Lip09,

Lip13, Lip20 and Lip53 at about 0.9, 1.3, 2.0 and 5.3 ppm and labeled 1, 3, 5, 10 respectively in Table 4.1) and of the water peak (at about 4.65 ppm) as resonance areas of the metabolite (the term "resonance area" is used instead of "peak area", since LCModel attempts to resolve overlapping signals, even when they form only one combined peak). The calcaneal marrow fat content Mfc, defined as the relative fat signal amplitude in percentage of total signal amplitude (water and fat), was calculated for all subjects, according to the equation 4.1 where I_{wat} is the water peak concentration and I_{fat} is the concentration sum of the Lip09, Lip13 and Lip20 peaks, as calculated by LCModel, because Lip09 is difficult to resolve from Lip13 and Lip20, therefore the concentration sums Lip09+Lip13+Lip20 is more accurate. Mfc values were averaged across all subjects for each bone density group (normal, osteopenia and osteoporosis, labeled 1, 2 and 3 respectively) and for the control group (labeled C) and their standard deviations were calculated.

       The mean values of T-$score$, Age and Mfc variables were compared among the three bone density groups and between the control and normal group with the one-way analysis of variance test (one-way ANOVA). Pearson correlation coefficients (r) were calculated to assess the linear relationship between pairs of variables for all postmenopausal subjects and for all subjects of each bone density group. A p value of less than 0.05 was considered to indicate a statistically significant difference.

4.3   Results and discussion

       The results reported in Tab. 4.2 and in the graphs in Fig. 4.5 show that our three bone density groups are significantly well separated in T-$score$ values and their mean Age values have an increasing trend as bone density decreases. Age differences are statistically significant between osteopenia and osteoporosis groups only ($p < 0.01$), therefore we can rule out age differences as a possible confounding factor in this study for the normal-osteopenia comparisons. Conversely, mean Mfc values don't point out any statistically significant difference with bone density changes, neither between the control and normal group.

       For paired data of all postmenopausal subjects, we obtained a low significant negative correlation between T-$score$ and Age ($r =$
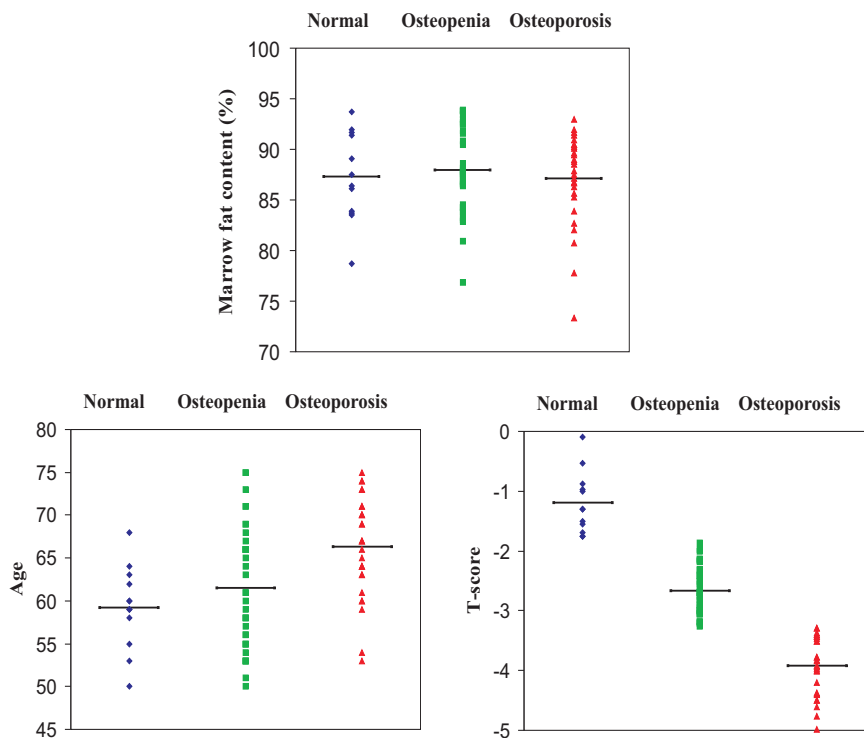
Figure 4.5: Graphs show calcaneal marrow fat content, Age and $T\text{-}score$ for three bone density groups (normal bone density, osteopenia, and osteoporosis). Mean Age values are characterized by an increasing trend and mean $T\text{-}score$ values are characterized by a decreasing trend as bone density decreases, while mean Mfc values have no trend. Horizontal bar = mean value for each group (see Tab. 4.2). (Normal: ♦-blue, osteopenia: ■-green, osteoporosis: ▲-red).

Parameter	Ranking (1-2-3)	C (n = 6)	1 (n = 12)	2 (n = 37)	3 (n = 28)	p value (C vs 1)	p value (1 vs 2)	p value (2 vs 3)	p value (1 vs 3)
T-score	D	–	-1.20 ± 0.52	-2.66 ± 0.39	-3.92 ± 0.49	–	***	***	***
Age	U	29 ± 3	59 ± 5	62 ± 7	66 ± 6	***	ns	**	**
Mfc (%)	N	87.43 ± 4.05	87.30 ± 4.44	87.98 ± 4.18	87.11 ± 4.51	ns	ns	ns	ns

Table 4.2: The mean values of *T-score*, *Age* and *Mfc* variables, with their standard deviations are reported for the control group (the only one without *T-score*) and for each bone density group. The comparison of these values among the three bone density groups and between the control and normal group, by *p* values obtained with the one-way analysis of variance test (one-way ANOVA), and their ranking trends among the three bone density groups are also reported. Notes: 1. Data are mean $\pm$ 1 standard deviation; 2. U (upward ranking); D (downward ranking); N (no ranking); 3. C (Control group); 1 (Normal); 2 (Osteopenia); 3 (Osteoporosis); 4. ns ($p \geq 0.05$); * ($p < 0.05$); ** ($p < 0.01$); *** ($p < 0.001$).

Figure 4.6: *T-score*, *Age* and *Mfc* paired values of all postmenopausal subjects are plotted and examined by linear correlation with their coefficients of determination (R^2).

Parameter	T-score	Age	Mfc
T-score	1	$-0.425 ** (2)$	0.080
Age		1	0.102
Mfc			1

Table 4.3: Pearson correlation coefficient test results (r) between pairs of variables (among *T-score*, *Age* and *Mfc* variables) for all postmenopausal subjects. Notes: 1. Data are Pearson correlation coefficients (r); 2. $*$ $(p < 0.05)$; $**$ $(p < 0.01)$; 3. (1) little $(0 \leq r \leq 0.29)$, (2) low $(0.3 \leq r \leq 0.49)$, (3) moderate $(0.5 \leq r \leq 0.69)$, (4) high $(0.7 \leq r \leq 0.89)$, (5) very high $(0.9 \leq r \leq 1)$.

-0.425, $p < 0.01$), but no significant correlation between *T-score* and *Mfc* and between *Age* and *Mfc* (see Tab. 4.3 and Fig. 4.6). Any significant correlation in each bone density group was also observed for paired data of the three variables.

   Our results partly agree with literature findings, for the absence of correlation between *T-score* and *Mfc*, but partly disagree for the absence of statistically significant correlation between *Age* and *Mfc*, and for the absence of any statistically significant trend of mean *Mfc* values with bone density changes. These disagreements can be ascribed to the different anatomical region chosen, and in particularly to the different kind of bone marrow investigated.

As previous described, in calcaneus a predominance of fatty marrow (*Mfc* ranges from about 83% to 98% [72]) exists, whereas in vertebra there is a predominance of hematopoietic marrow rich of water (*Mfc* ranges from about 27% to 70% [72]). In our results, *Mfc* ranges from about 80% to 94%, in good agreement with Liney *et al* results [72]; this small range hampers to obtain a linear correlation between *Age* and *Mfc* [72] and to point out the probable skill of *Mfc* to detect bone density changes. Moreover, in this situation it's very hard to discriminate the little compensatory filling, as suggested before, of the intertrabecular spaces created by osteoporosis with fatty marrow, from the high marrow fat content of calcaneus. However, the *Mfc* information obtained, will be need for the analysis in the next chapters.

Chapter 5

Bone marrow diffusion

5.1   State of the art

As previous underlined, osteoporosis is a disease that predisposes to bone fracture and it is clinically diagnosed by means of bone mineral density (BMD).

The poor correlation between fracture prevalence and BMD diagnosis suggests that other factors besides low BMD contribute to bone fragility; in effect, with osteoporosis, in addition to low BMD, the bone microarchitecture is rearranged or disrupted, the amount and the variety of proteins in bone is altered and the bone marrow quality also is altered. Many factors associated with increased individual susceptibility to osteoporosis have been identified, but the actual pathophysiology of osteoporosis, however, remains unclear.

The MR imaging techniques developed for better understanding of osteoporosis are MR relaxometry and high-resolution MR imaging; these are based on the study of trabecular bone. Although MR imaging techniques employ no radiation compared to DXA and QCT, one feature common all these techniques is the focus on measuring the structural end-point of bone loss. They provide no information on the physiological or functional changes associated with osteoporosis. Other MR imaging techniques can enable investigation of two aspects of bone physiology that may provide insight to the pathogenesis of osteoporosis: marrow fat content and marrow diffusion.

Apparent diffusion coefficients derived from MR diffusion imaging has been used successfully in differentiating between benign and malignant

acute vertebral body compression fractures [85, 86]. Based on the altered cellular composition of the bone marrow induced by malignant cell proliferation, measurable changes in the random motion of water molecules within bone tissues can be detected. Evidence obtained from an in vivo MR spectroscopy study has shown that changes in the proportion of bone marrow fat may be associated with bone weakening [73]. However, it is unclear whether changes in the bone marrow composition associated with osteoporosis and their effect on marrow water diffusion may also be detected by means of MR diffusion imaging; moreover, the relationship between ADC in vivo and T-$score$ is not clear.

Many MR studies focused to measure the ADC of the lumbar spine and to its correlation with bone mineral density and with Mfc: Yeung *et al* [87] demonstrated vertebral diffusion restriction in patients with osteoporosis, but their study was limited secondary to the small number of subjects; Griffith *et al* [71, 88] found a decreasing vertebral ADC for decreasing BMD, without statistically significant differences among the osteoporotic, osteopenic and normal bone attenuation groups, no correlation between ADC and T-$score$ and a mild positive correlation between ADC and vertebral marrow fat content; Hatipoglu *et al* [89] found a decreasing vertebral ADC for decreasing BMD with statistically significant differences only between normal and osteopenic groups and a mild positive correlation between ADC and T-$score$; Ueda *et al* [90] obtained a strong negative correlation between ADC and T-$score$ and a strong positive correlation between ADC and Mfc, at low-intermediate marrow fat content (20%-60%).
This lack of clear findings in literature, mostly for the situation with very high marrow fat content, induced us to investigate the ADC parameter and its correlation with T-$score$, Mfc and Age of the subjects, in calcaneus, in talus and in some their different regions.

5.2   Materials and methods

For each volunteer (see section 4.2), we acquired sagittal view images obtained on the same slices (5 mm thickness) and by using the same foot position. We performed a high resolution FLASH image at 3.0 T using square FOV=180 mm, matrix=512x512, TE=10

ms, TR=600 ms, BW=160 Hz/pixel and a sagittal diffusion weigh-ted segmented Echo-Planar Imaging (EPI) with TE=86 ms, TR=1.5 s, BW=1954 Hz/pixel, square FOV=192 mm, matrix=128x128, reso-lution=1.5x1.5x10 mm, epi factor=7, diffusion mode= phase (anterior-posterior direction) and *b-value*=0, 8000, of the heel of every volunteer. N data subjects were not analyzed due to motion artifacts on DWI im-ages. As a consequence, five premenopausal females (mean age 29 ± 3 years), eight postmenopausal healthy females (mean age 58 ± 4 years and mean $T\text{-}score$ -1.34 ± 0.44), twenty-five postmenopausal osteopenic females (mean age 61 ± 7 years and mean $T\text{-}score$ -2.62 ± 0.41) and twenty-two postmenopausal osteoporotic females (mean age 66 ± 6 years and mean $T\text{-}score$ -3.91 ± 0.45).

With the same images, it was possible to analyze the whole calcaneus (labeled $CALCA$) and the whole talus (labeled AT) (see Fig. 5.1). We also focused our attention on a talar region (labeled AC) close to calcaneus and on three different calcaneal sites: the subtalar (labeled ST), the tuber calcanei (labeled TC) and cavum calcanei (labeled CC) regions. The ST region is characterized by the highest trabecular den-sity because it transmits the stresses exerted by the weight of the body from the tibia, via the talus to the heel, then the trabecular density progressively decreases in TC and in CC regions. The CC region is characterized by the lowest and isotropic trabecular density [91, 92].

Apparent diffusion coefficients ADC were obtained from dif-fusion weighted segmented EPI images, substituting in the equation 3.18 the *b-values* and the respective mean signal intensities of the whole calcaneus, the whole talus and of the AC, ST, TC and CC regions, of every subjects. ADC values of each region, were averaged across all subjects for each bone density group (normal, osteopenia and os-teoporosis, labeled 1, 2 and 3 respectively) and for the control group (labeled C) and their standard deviations were calculated. ADC values from postmenopausal women were also graphed, for each region, with their averages and were plotted versus marrow fat content Mfc values obtained in the previous chapter (see section 4.3). For each region, the mean ADC values were compared among the three bone density groups and between the control and normal group with the one-way analysis of variance test (one-way ANOVA) and Pearson correlation coefficients

(r) were calculated to assess the linear relationship between pairs of variables (among *T-score*, *Age*, *Mfc* and *ADC* variables) for all post-menopausal subjects and for all subjects of each bone density group. A p value of less than 0.05 was considered to indicate a statistically significant difference.

5.3   Results and discussion

The trabecular bone structure in the calcaneus is clearly depicted in the high resolution MR image reported in Fig. 5.1. Here, the trabecular bone network appears dark while the bone marrow appears bright. The regional heterogeneity in the trabecular architecture and the trabecular bone density are also apparent from the image. The trabecular structure appears more oriented and denser in the ST region and sparser with no preferred trabecular platelets orientation in CC region. In Fig. 5.2 we have reported sagittal diffusion weighted images of the heel (the first in literature) in a normal (A), osteopenic (B) and osteoporotic (C) postmenopausal female subject.

The results reported in Tab. 5.1 and in the graphs in Fig. 5.3 show that the mean ADC values of the three bone density groups are characterized by an increasing trend as bone density decreases but these differences are statistically significant between the three groups in subtalar region only. ST region is the only one with statistically significant discrimination between normal and osteopenic group by ADC values, and CC is the best region to discriminate between osteopenic and osteoporotic group. Conversely, ADC values don't point out any statistically significant difference between the control and normal group, in each analyzed region. The mean ADC values obtained in this work are one order of magnitude lower than those reported in previous studies focused on vertebrae [87, 89, 90, 93]; this difference is due to higher marrow fat content in calcaneus compared to those in vertebrae, which restricts water molecular diffusion.

For paired data of all postmenopausal subjects, we obtained a moderate significant negative correlation between *T-score* and *ADC* in CC region ($r = -0.497$, $p < 0.01$) and a low significant negative correlation in all the other analyzed regions (see Tab. 5.2). Even if ADC

Figure 5.1: Sagittal high resolution MR image of the heel showing the investigated locations: the whole calcaneus (labeled $CALCA$), the whole talus (labeled AT), the talar region (labeled AC) close to calcaneus and the three different calcaneal sites with their large regional variation in trabecular bone density and orientation, the subtalar (labeled ST), the tuber calcanei (labeled TC) and cavum calcanei regions (labeled CC).
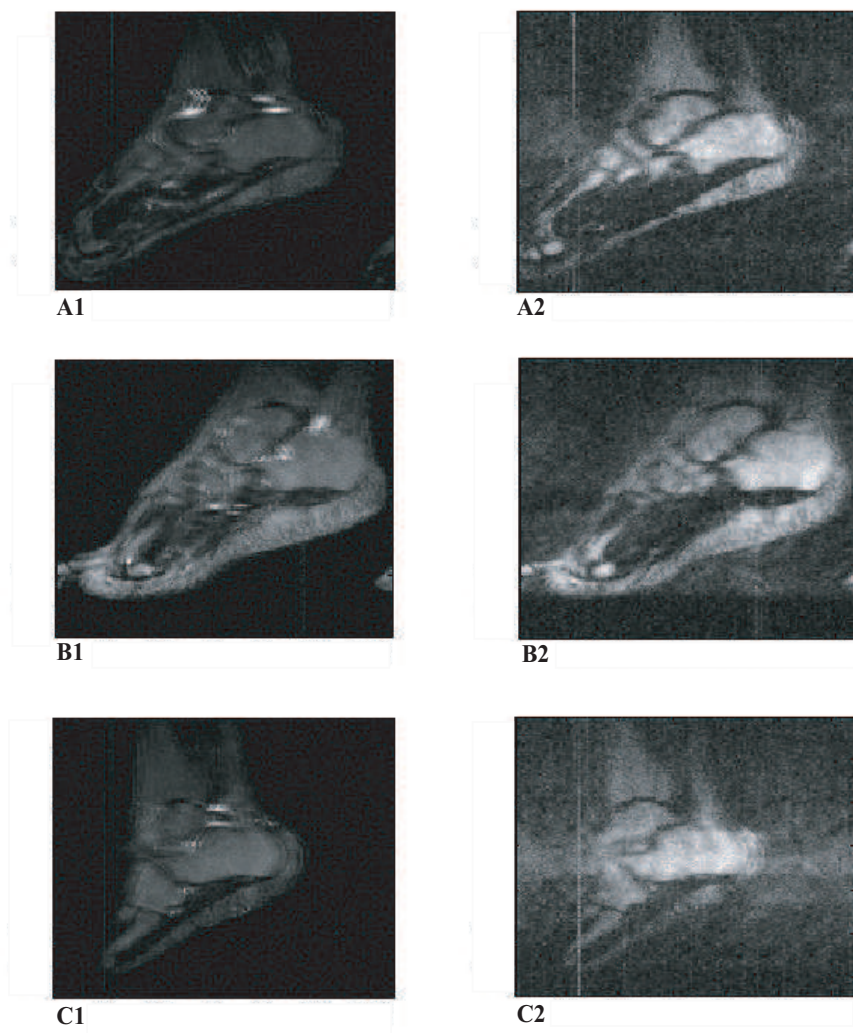
Figure 5.2: Sagittal diffusion weighted segmented Echo-Planar Imaging (EPI) of the calcaneus and talus in a 55-years-old normal female volunteer (A1 with b=0, A2 with b=8000), in a 69-years-old osteopenic female volunteer (B1 with b=0, B2 with b=8000) and in a 64-years-old osteoporotic female volunteer (C1 with b=0, C2 with b=8000) at 3.0 T.
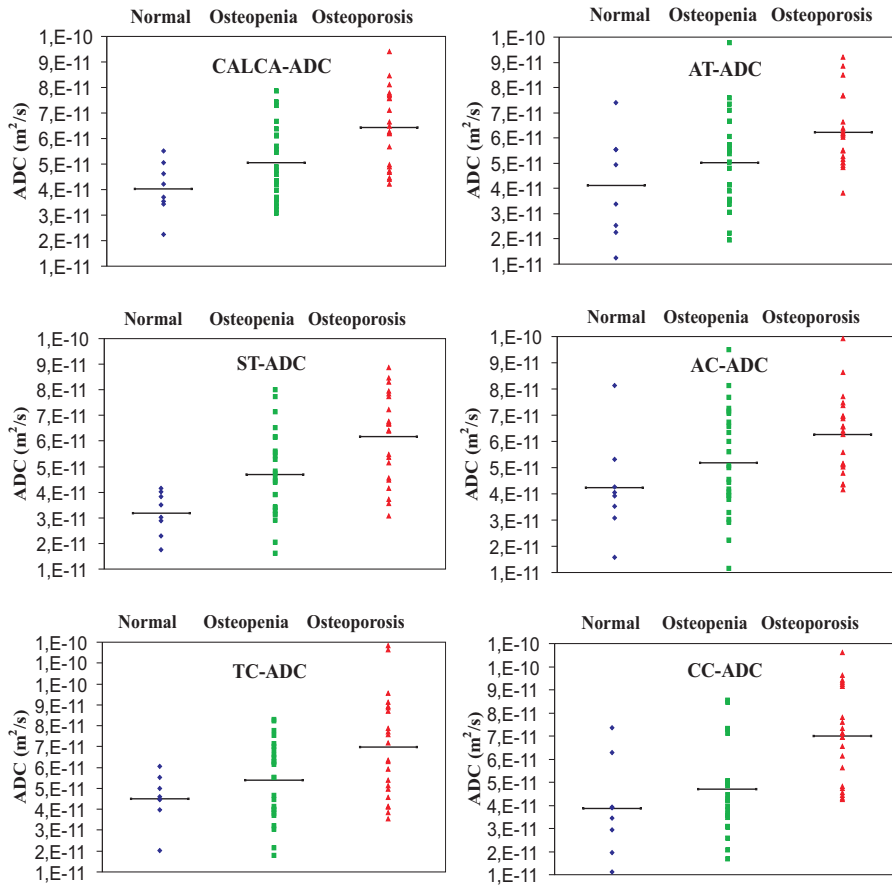
Figure 5.3: Graphs show *ADC* values, for three bone density groups (normal bone density, osteopenia, and osteoporosis), in the whole calcaneus (*CALCA*), the whole talus (*AT*) and in the *ST*, *AC*, *TC* and *CC* regions. Mean *ADC* values increase as bone density decreases; *ST* region is the only one with statistically significant discrimination between normal and osteopenic group, *CC* is the best region to discriminate between osteopenic and osteoporotic group. Horizontal bar = mean value for each group (see Tab. 5.1). (Normal: ♦-blue, osteopenia: ■-green, osteoporosis: ▲-red).

Site-Parameter	Ranking (1-2-3)	C ($n = 6; 5^\star$)	1 ($n = 12; 8^\star$)	2 ($n = 37; 25^\star$)	3 ($n = 28; 22^\star$)	p value (C vs 1)	p value (1 vs 2)	p value (2 vs 3)	p value (1 vs 3)
T-score	D	—	-1.20 ± 0.52	-2.66 ± 0.39	-3.92 ± 0.49	—	***	***	***
Age	U	29 ± 3	59 ± 5	62 ± 7	66 ± 6	***	ns	ns	ns
Mfc (%)	N	87.43 ± 4.05	87.30 ± 4.44	87.98 ± 4.18	87.11 ± 4.51	ns	ns	ns	ns
AC-ADC (m^2/s)	U	$(3.82 \pm 1.97)E\text{-}11$	$(4.23 \pm 1.90)E\text{-}11$	$(5.19 \pm 2.02)E\text{-}11$	$(6.25 \pm 1.50)E\text{-}11$	ns	ns	ns	**
AT-ADC (m^2/s)	U	$(4.28 \pm 2.04)E\text{-}11$	$(4.11 \pm 2.08)E\text{-}11$	$(5.02 \pm 1.87)E\text{-}11$	$(6.23 \pm 1.43)E\text{-}11$	ns	ns	*	**
ST-ADC (m^2/s)	U	$(4.05 \pm 1.51)E\text{-}11$	$(3.18 \pm 0.85)E\text{-}11$	$(4.70 \pm 1.68)E\text{-}11$	$(6.16 \pm 1.72)E\text{-}11$	ns	*	**	***
TC-ADC (m^2/s)	U	$(6.15 \pm 2.31)E\text{-}11$	$(4.51 \pm 1.20)E\text{-}11$	$(5.39 \pm 1.88)E\text{-}11$	$(6.96 \pm 2.43)E\text{-}11$	ns	ns	*	*
CC-ADC (m^2/s)	U	$(4.65 \pm 1.03)E\text{-}11$	$(3.86 \pm 2.09)E\text{-}11$	$(4.70 \pm 1.84)E\text{-}11$	$(6.99 \pm 1.98)E\text{-}11$	ns	ns	***	**
CALCA-ADC (m^2/s)	U	$(4.91 \pm 0.75)E\text{-}11$	$(4.04 \pm 1.04)E\text{-}11$	$(5.06 \pm 1.41)E\text{-}11$	$(6.42 \pm 1.51)E\text{-}11$	ns	ns	**	***

Table 5.1: The mean values of T-score, Age, Mfc and ADC variables, with their standard deviations are reported for the control group (the only one without T-score) and for each bone density group. The comparison of these values among the three bone density groups and between the control and normal group, by p values obtained with the one-way analysis of variance test (one-way ANOVA), and their ranking trends among the three bone density groups are also reported. Notes: 1. Data are mean $\pm$ 1 standard deviation; 2. U (upward ranking); D (downward ranking); N (no ranking); 3. C (Control group); 1 (Normal); 2 (Osteopenia); 3 (Osteoporosis); 4. ns ($p \geq 0.05$); * ($p < 0.05$); ** ($p < 0.01$); *** ($p < 0.001$); 5. AC (the talar region close to calcaneus); AT (the whole talus); ST (the subtalar region of calcaneus); TC (the tuber calcanei region); CC (the cavum calcanei region); $CALCA$ (the whole calcaneus); 6. $\star$ (number of subjects analyzed for ADC measures).

Parameter	T-score	Age	Mfc	AC-ADC
T-score	1	$-0.425**(2)$	0.080	$-0.316*(2)$
Age		1	0.102	0.155
Mfc			1	-0.148
AC-ADC				1
Parameter	T-score	Age	Mfc	AT-ADC
T-score	1	$-0.425**(2)$	0.080	$-0.376**(2)$
Age		1	0.102	0.214
Mfc			1	-0.163
AT-ADC				1
Parameter	T-score	Age	Mfc	CALCA-ADC
T-score	1	$-0.425**(2)$	0.080	$-0.463**(2)$
Age		1	0.102	0.108
Mfc			1	$-0.301*(2)$
CALCA-ADC				1
Parameter	T-score	Age	Mfc	ST-ADC
T-score	1	$-0.425**(2)$	0.080	$-0.488**(2)$
Age		1	0.102	0.135
Mfc			1	-0.250
ST-ADC				1
Parameter	T-score	Age	Mfc	TC-ADC
T-score	1	$-0.425**(2)$	0.080	$-0.350**(2)$
Age		1	0.102	0.100
Mfc			1	-0.143
TC-ADC				1
Parameter	T-score	Age	Mfc	CC-ADC
T-score	1	$-0.425**(2)$	0.080	$-0.497**(3)$
Age		1	0.102	0.177
Mfc			1	-0.248
CC-ADC				1

Table 5.2: Pearson correlation coefficient test results (r) between pairs of variables (among *T-score*, *Age*, *Mfc* and *ADC* variables, in each investigated region) for all postmenopausal subjects. Notes: 1. Data are Pearson correlation coefficients (r); 2. $*$ ($p < 0.05$); $**$ ($p < 0.01$); 3. (1) little ($0 \leq r \leq 0.29$), (2) low ($0.3 \leq r \leq 0.49$), (3) moderate ($0.5 \leq r \leq 0.69$), (4) high ($0.7 \leq r \leq 0.89$), (5) very high ($0.9 \leq r \leq 1$).

parameter is able to distinguish the three bone density groups, according to WHO criteria, it has a low or moderate significant correlation with *T-score* values and this demonstrates that it doesn't depend only on the bone density but also on other factors bound to the bone quality, as previous underlined. No significant correlation between ADC and *Age* and almost never between ADC and Mfc was observed. A low significant negative correlation between Mfc and ADC was obtained in the whole calcaneus for all the postmenopausal subjects ($r = -0.301$, $p < 0.05$) and for the osteoporotic subjects ($r = -0.429$, $p < 0.05$).

Our results agree with Ueda *et al* [90] findings at low or intermediate marrow fat content (20%-60%), for the statistically significant negative correlation between ADC and *T-score* values, but disagree with Griffith *et al* [71, 88] and Hatipoglu *et al* [89] findings at intermediate-high marrow fat content (45%-80%), for the opposite trend of mean ADC values obtained with bone density changes. These different trends can be ascribed to the different marrow fat contents analyzed.
Under low or intermediate marrow fat content, water molecules seem restricted by the trabecular bone rather than fat cells, thus the change in ADC value depends on the trabecular bone architecture under this Mfc condition. Conversely, under intermediate or high marrow fat content, water molecules seem to be more restricted by the fat cell concentration than trabecular bone. When marrow fat content (80%-94%) is very high, that is in saturation condition like in calcaneal bone marrow (our case), ADC parameter becomes again sensible to the intertrabecular spaces created by trabecular bone density decreasing.

Taking into consideration the whole calcaneus and its regions only, in which it was evaluated the Mfc, in the Fig. 5.4 it is possible to notice that for low or intermediate bone density, ADC values decrease as Mfc increases and this trend is higher for osteoporotic than osteopenic group; the negative angular coefficients of the ADC regression straight lines are, in absolute values, higher in osteoporotic than in osteopenic group. Thus, for low bone density and very high Mfc values, water molecules anyway seem restricted by the fat cell concentration. In the same graphs, the straight lines of the three bone density groups, obtained by the linear regression analysis, tend to a common intermediate ADC value at highest Mfc values, probably due to a free space

saturation by fat cells.

In table 5.1, the mean ADC values of the three bone density groups overlap when considering their SDs. Thus, the large standard deviation (SD) associated with mean ADC values assessed in spongy bone tissue from healthy, osteopenic and osteoporotic individuals does not allow the clinical use of ADC on a single subject basis, but by the last considerations, we can assert that the marrow fat content evaluation might improve the diagnostic confidence of osteoporosis, by ADC assessment of the calcaneal regions in subjects with lowest Mfc values.
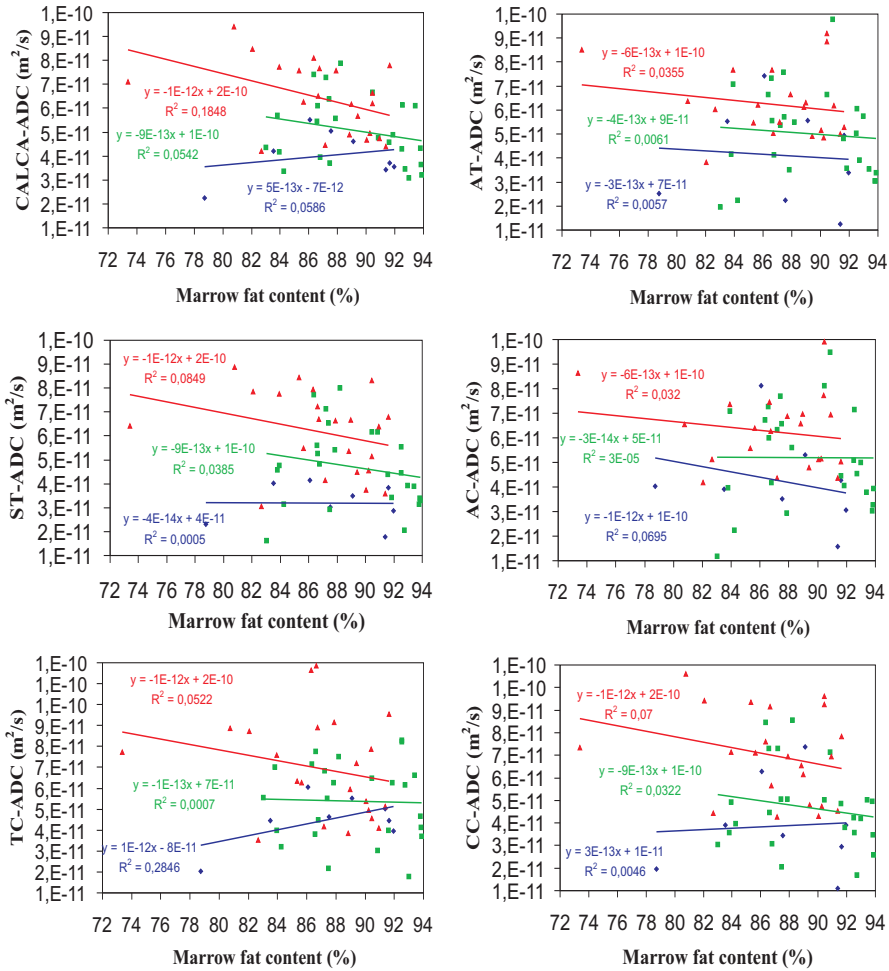
Figure 5.4: For each investigated region and for each group, *ADC* and *Mfc* values of all postmenopausal subjects are plotted and examined by linear correlation with their coefficients of determination (R^2). (Normal: ♦-blue, osteopenia: ■-green, osteoporosis: ▲-red).

Chapter 6

Internal gradient

6.1 State of the art

Magnetic resonance (MR) is a non-invasive technique which is able to provide information on the relaxation and diffusion properties of water and fat protons from soft biological tissues such as bone marrow. Therefore, when applied to the investigation of spongy bone, MR provides information on bone marrow which is strictly linked to the surrounding trabecular architecture of the bone due to the mutual interaction between the solid matrix and liquid phase [94].

In this context, the apparent transverse relaxation time $T_2^\star$ was the first MR parameter to be considered as a new surrogate marker for osteoporosis. Indeed, $T_2^\star$ probes the micro-structure of TB due to its sensitivity to the microscopic field in-homogeneities caused by magnetic susceptibility differences between the solid bone structure and the liquid bone marrow [95, 96]. The dephasing of the transverse magnetization due to susceptibility differences produces a $T_2^\star$ shortening (see eqn. 3.22 and 3.20).

Several studies have consistently reported that, in different skeletal sites such as the calcaneus, femoral neck and lumbar spine, an increase in inter-trabecular space, which typically occurs in patients with osteoporosis, prolongs the corresponding $T_2^\star$ values [3, 97, 98]. Negative correlations between $T_2^\star$ and BMD were also observed in the same different skeletal sites [6, 7] and positive correlation between $T_2^\star$ and Age in the lumbar spine of healthy subjects [97]. Moreover, Wehrli et $al.$ measured $R_2^\star$ in the calcaneus and proximal femur of 68 women of varying spinal

bone mineral density (BMD) and vertebral fracture status [3]: calcaneal $R_2^\star$, within each subject, was highly positively correlated to the femoral $R_2^\star$ and to the femoral and vertebral BMD; the strongest discriminator of vertebral deformity was $R_2^\star$ of the calcaneus, which was lower in the fracture group, consistent with lower trabecular density; among the calcaneal sites examined, the ST region best discriminated the two groups, with 77% diagnostic accuracy compared with 66% for vertebral BMD, the cavum calcanei and the tuber calcanei also had significantly reduced $R_2^\star$ in the fracture group.

However, the large standard deviation (SD) associated with average $T_2^\star$ values assessed in bone tissue from healthy, osteopenic and osteoporotic individuals does not allow the clinical use of $T_2^\star$ on a single subject basis [99]. The high inter-subject variability observed across studies is likely to be due to differences in water/fat ratios which affect $T_2^\star$ decay. Remarkably, higher values of $T_2^\star$ have been reported for fat as compared to the water component, either in vitro [100, 101] or in vivo [102]. Furthermore, several kinds of fat molecules are present in bone tissue [103], with relative concentration again varying across subjects.

In this chapter we propose an alternative way respect to $T_2^\star$ assessment, to quantify the influence of susceptibility changes in spongy bone. The strategy is based on a new MR parameter (the internal gradient G_i) that we demonstrate to be strictly associated with trabecular bone TB density and structural rearrangements. Estimation of G_i can be obtained by extraction of this parameter from the Spin-Echo (SE) decay (see the subsection 3.3.1), which is traditionally used for the investigation of porous systems [104–106]. In a SE sequence, signal refocusing is obtained by reversing the de-coherence effects of spins caused by the distribution of local fields. This method is valid only when molecular diffusion is not taken into account. Diffusion of liquid state protons in local magnetic field gradients (internal gradients G_i) results in a more than expected rapid loss of coherence from the usual spin-spin interaction and surface effects [104, 107]. In SE measurements, the additional decay of the echo amplitude is due to the diffusion of fluid molecules in the local magnetic field gradient G_i generated by the difference in magnetic susceptibility between bone marrow and solid bone plates. As a consequence, in systems like spongy bone, it is possible to assess the

intensity of G_i from the attenuation of SE decay. In spongy bone, G_i values are not only affected by differences in magnetic susceptibility between bone marrow and solid bone plates, but also between fat and water diffusion in TB marrow. Moreover, G_i depends on the orientation of the trabecular plates with respect to the external magnetic field (see the subsection 3.3.1) [96, 108]. Some previous works have focused on these G_i features in order to assess the preferential orientation of trabeculae due to loading optimization [96, 109]. Recently, a new MR approach based on the detection of spin diffusion through an internal magnetic field gradient has been proposed to characterize TB [110, 111]. This approach is based on measuring the G_i to encode diffusion weighting to extract structural information (e.g., surface-to-volume ratio of spongy-bone pores) from the resulting signal decay.

In all these situations, G_i seems to be a potential surrogate marker reflecting different structural features of TB. They include not only the solid phase density, but also other characteristics related to spongy-bone quality (as expressed by water/fat concentrations within the bone marrow).

The aim of the present work was to assess the potential ability of G_i to describe spongy bone status as related to its TB density and quality. For this purpose, using a micro-imaging probe we investigated in vitro at high magnetic field (9.4 T) G_i behavior inside each single pore of calf spongy-bone samples (extracted from a femur head) as a function of both TB density and relative fat and water-bone marrow concentrations. To test the methodological feasibility of this approach, we first quantified mean G_i in calf samples characterized by different TB densities. We then, investigated the potential suitability of G_i as a measure able to assess the TB status *in vivo*. For this purpose, using a 3T clinical scanner, we evaluated the G_i parameter, but also the $T_2^\star$ and T_2 parameters and their correlations with *T-score*, *Mfc*, *ADC* and *Age* of the subjects, in calcaneus, in talus and in some their different regions.

6.2   *In vitro* experiments

6.2.1   Materials and methods

In vitro experiments were performed using a Bruker Avance-400 high-resolution spectrometer operating at 9.4 T with a micro-imaging probe (10 mm internal diameter), equipped with a gradient unit characterized by a maximum gradient strength of 1200 mT m^{-1} and a rise time of 100 μs. XWINNMR® and ParaVision® 3.0 software were employed for data acquisition and analysis.

Five ex vivo spongy-bone samples, excised from calf femur head, were cut into pieces of approximately 20 mm high and 7 mm deep in order to fit into the micro-imaging probe bore. The long axis of each sample was located parallel to the main direction of the static magnetic field (the z-axis). The temperature of each sample was fixed to 291 K. $T_2^\star$-weighted (Gradient Echo, GE) and T_2-weighted (SE) images were obtained for initial evaluation of TB density. All samples were characterized by a non-uniform trabecular density. As shown in figure 6.1, TB density varies continuously along the height of each sample, moving from the upper to the lower zone. The upper zone, which is close to the cortical bone, is characterized by higher trabecular density and smaller spongy-bone pores (see Fig. 6.1(a)). Conversely, the lower zone is characterized by a larger inter-trabecular space (see Fig. 6.1(c)). The middle zone (located between upper and lower zones) shows intermediate characteristics of TB density (see Fig. 6.1(b)). Throughout the paper, we will refer to these three anatomical locations as follows: (a) HTD (high trabecular density; upper zone), (b) ITD (intermediate trabecular density; middle zone) and (c) LTD (lower trabecular density; lower zone). In each sample, for each considered location, we identified three 0.2 mm thickness slices to measure quantitative MR parameters. Data extracted from each of the three slices were then averaged to obtain mean values of each MR parameter in the three locations (HTD, ITD and LTD). Five analyzed samples were selected such that they were characterized by similar TB densities and similar fat-to-water ratio quantities in bone marrow. TB density and bone marrow water content (together with the relative content of different types of fat in bone marrow) are known to be dependent on age, race and skeletal
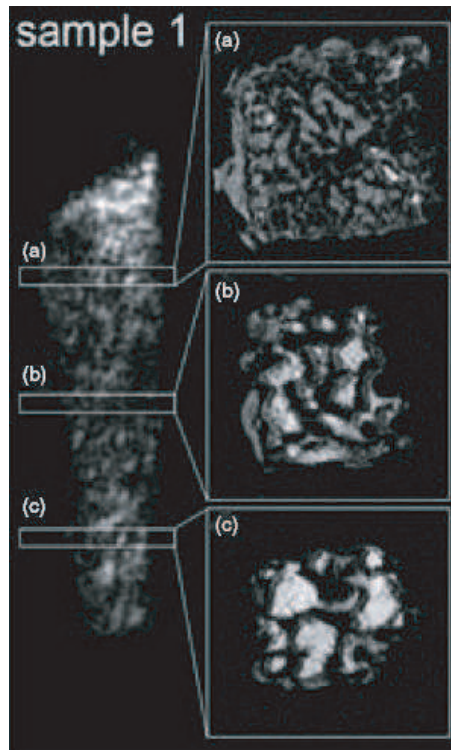
Figure 6.1: An example of the calf spongy-bone sample used for experiments in vitro [112]. GE localizer and SE images (*TE*=4.3 ms) selected perpendicularly to the static magnetic field at three different depths in the sample show a non-uniform TB density. In each experimental sample, trabeculae are closely spaced in the upper zone (a). Conversely, they show an intermediate density in the middle zone (b) and a larger inter-trabecular space in the lower zone (c).

site. To correct for these potential biases, we obtained all our samples
from 10- to 12-month-old calves of German race, bred in Germany and
butchered in Rome (Italy). In all fresh samples (analyzed immediately
after slaughter) we identified the same area of the femur head for MR
investigation.

In the first step of our experiments, a validation experiment
was performed under ideal circumstances where molecular diffusion and
T_2 information were obtained for each of the two individual spectral
components (water and fat molecules). A spectroscopic Carr-Purcell-
Meiboom-Gill (CPMG, repetition time TR=1 s, number of averaged
scans NS=8, N=64 data points, (corresponding to 64 echoes refocusing
every 2 ms from 1 to 127 ms) and a spectroscopic pulsed field gradient
stimulated echo (PGSE, TE/TR=18/3000 ms, diffusion gradient pulses
delay Δ=400 ms, diffusion gradient pulses duration δ=4.6 ms and dif-
fusion gradient strength g applied along the x-axis using 32 gradient
amplitude steps from 6 to 100 mT m^{-1}) were used to recognize and
discriminate T_2 and ADC of water and fat molecules in the samples.

A MSME (multi-slice multi-echo) imaging sequence (TR=2000
ms, field of view FOV=7 mm, matrix 256x256, slice thickness STH=0.2
mm, pixel dimensions 27x27 μm^2, NS=8) at various TEs (4.8, 6, 8, 10,
12, 14, 16, 18, 20, 24, 30, 40, 50, 60, 70, 80, 100, 120 ms) was used to
obtain the SE decay in the three regions of each sample characterized by
a different TB density. A PGSTE imaging sequence was also employed
(TE/TR=21.9/3000 ms, FOV=7 mm, matrix 256x256, Δ=40 ms, δ=4
ms, using eight b values ranging from 400 to 40000 s mm^{-2}, STH=0.2
mm, NS=8) in order to measure the ADC along the x-axis for each
of the three selected regions of the considered samples. The b value is
related to the aforementioned parameters through the known relation:
$b = \gamma^2 g^2 \delta^2 (\Delta - \delta/3)$, where g is the diffusion gradient strength. The
x-axis was arbitrarily chosen to assess molecular diffusion perpendicular
to trabeculae surfaces (see Fig. 6.1).

After the micro-imaging investigation of the bone marrow's wa-
ter and fat behavior within pores of spongy bone, we set up an equivalent
acquisition protocol at lower TEs (4.8, 10, 20, 40, 60, 80, 100 ms) and
b values (ranging from 200 to 10000 s mm^{-2}). This additional protocol
was added to obtain a protocol potentially suitable for clinical applica-

tion (i.e. lower scan time, lower b values). However, due to a reduced number of experimental points, this acquisition provides SE decays and ADCs that do not clearly discriminate between water and fat.

T_2 and ADC of water and fat components were obtained using a Levenberg-Marquardt (L-M) fit taking into account the peak area decays respectively centered at 4.7 ppm (large from 4 to 5.4 ppm) for water and at 1.3 ppm (large from 0.1 to 2.5 ppm) for fat. Due to the low resolution of bone marrow spectra in the spongy-bone samples, the olefinic fat peak at 5.3 ppm overlaps the broad water peak centered at 4.7 ppm. For this reason, we fitted the attenuation of this broad peak (from 6 to 4 ppm) versus the diffusion gradient strength or the TE value using a bi-exponential function. This took into account the olefinic and water component separately. In figure 6.2 an example of spectroscopic investigation is shown.

Two different in vitro analyzes were performed using the data extracted from the imaging experiments. In both cases we considered only the central zone of each image (i.e. excluding the image border), in order to exclude or limit the presence of air in bone marrow cavities. Indeed, this represents one of the major sources of artifacts when performing imaging on excised samples.

In the first analysis, the signal deriving from water and fat protons in T_2-weighted images was investigated as a function of each voxel location with respect to the bone-bone marrow interface. In each slice of the three considered locations, the signal nearby the boundaries between bone marrow and solid bone was identified using a software (written in Matlab) (see Fig. 6.3) written in-house.

SE signal properties and G_i behavior were then assessed in the boundary and inner regions of the trabecular pores. The inner regions of the pores were identified by subtracting the boundary regions from the whole pore area. An L-M fit was performed using the signal as a superimposition of two components: one belonging to fats and another belonging to water molecules. Each component contributes to the total signal as one exponential term of formula 3.23 (the second part of formula). The signal intensity at TE=0, T_2^{true}, G_i and the ADC of water and of fat components were obtained. Using this procedure, mean and SD values of G_i from water and fat were respectively derived. Wa-
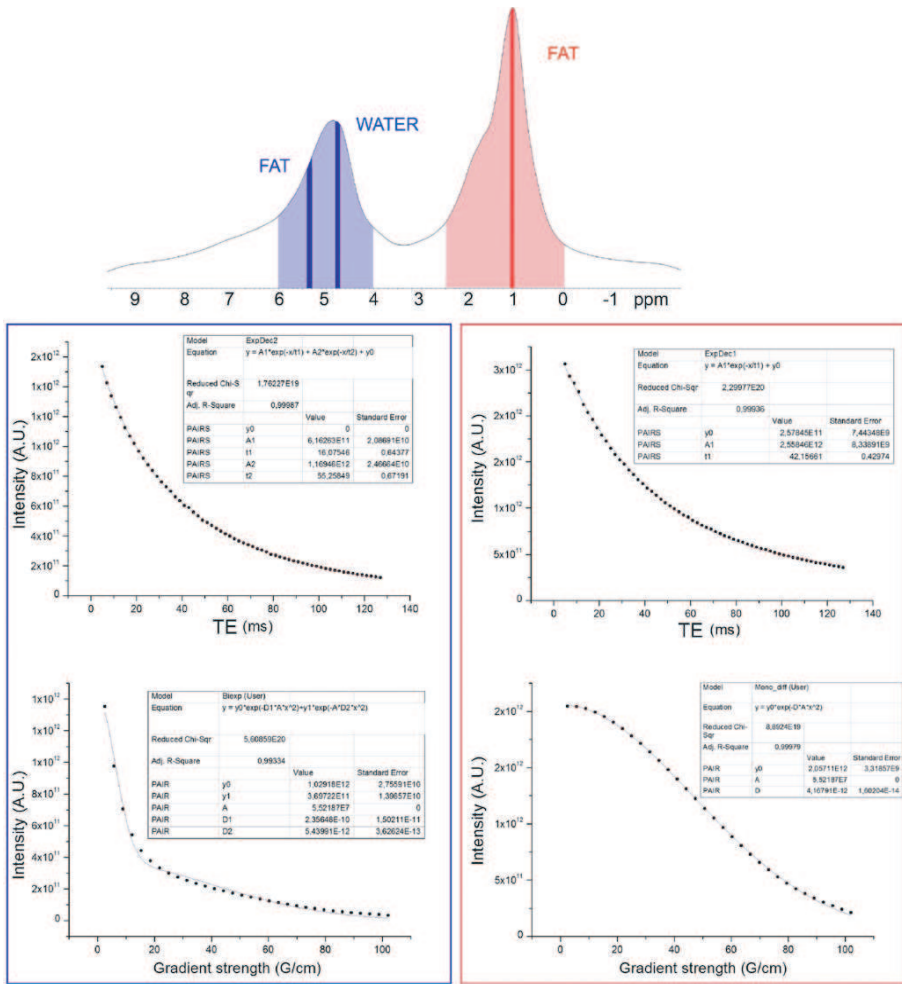
Figure 6.2: An example of the fitting procedure used in spectroscopic validation experiments to obtain T_2 and ADC of water and fat components [112]. The broad peak on the left side of the spectrum is characterized by two different components: water centered at 4.7 ppm and olefinic fat centered at 5.3 ppm. Peak attenuation versus gradient strength or TE value was fitted using a bi-exponential function which took into account olefinic and water components separately. Conversely, the attenuation of fat peak at 1.3 ppm (on the right side of the spectrum) was fitted using monoexponential functions.
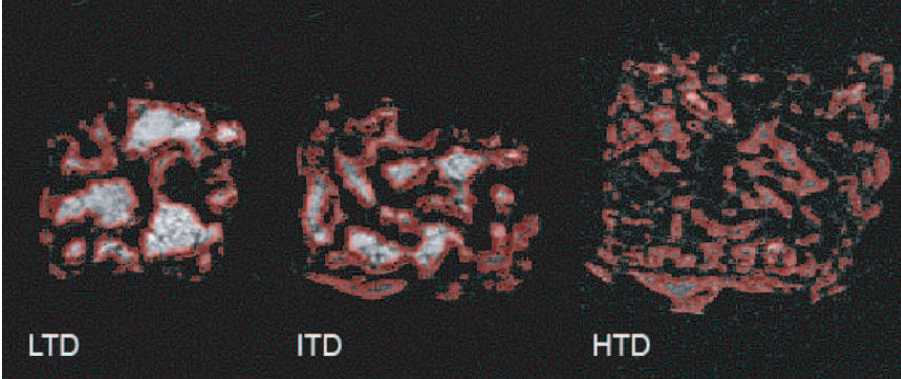
Figure 6.3: Example of selection of a three pixel wide boundary region in three considered locations, respectively, characterized by lower (LTD), intermediate (ITD), and higher trabecular density (HTD) [112]. The red mask, which represents the boundary region, is superimposed over SE images obtained at TE=4.3 ms.

ter ADC and fat ADC were measured from diffusion-weighted images, while T_2^{true} values were considered a free parameter in the fit.

Conventional T_2 relaxation times of water and fat components were also evaluated from the same images, executing a bi-exponential L-M fit of water and fat components, in accordance with formula 3.23 (the first part of formula). This analysis was repeated at different widths (measured in voxels) from the boundary region of each pore. The mean values of water and fat G_i were calculated by averaging the results obtained in all pores contained in three image slices for each specific location (HTD, ITD and LTD).

In order to have a more objective quantification of TB density, we calculated the ratio between the perimeter and the area of each pore in the slices. As a result, the ratio (N_p/N_a) between the number of voxels defining each pore perimeter (N_p) and the number of voxels constituting the corresponding area (N_a) was obtained from all pores included in each of the slices. Then, the mean values of N_p/N_a and G_i in different bone locations (characterized by different TB densities as defined by N_p/N_a) were obtained from each sample. Moreover, mean values of both magnetization associated with water and fat extracted from the bi-exponential fit as a function of the boundary region width

were evaluated. The averages were calculated in all five samples. Pearson's correlation coefficient (r) and a paired Student's t-test were used to assess the linear correlation between G_i and TB densities and differences between water and fat magnetization as a function of boundary distances measured in voxels.

In a second experiment, G_i was derived using the signal arising from each entire slice. In this case, we aimed to identify an acquisition protocol at high magnetic field which might also be suitable for clinical application (using relatively short acquisition times, conventional sequences and a lower image resolution compared to that obtained by micro-imaging apparatus). Distinguishing water from fat components was not a priority in this case. Therefore, a monoexponential L-M fit was employed to obtain the mean ADC along the x-axis. A monoexponential L-M fit was performed using formula 3.23 (the second part of formula) and included a constant which took into account the deviation from monoexponential behavior. Mean and SD values of G_i were obtained in the three bone locations (HTD, ITD and LTD) performing an average of G_i values across the five samples together with their corresponding values of T_2^{true}. Moreover, conventional T_2 relaxation time was estimated from each slice using a monoexponential L-M fit as described by formula 3.23 (the first part of formula) plus a constant. Again, mean and SD values of T_2 were obtained in the three zones (HTD, ITD and LTD) by performing an average of T_2 values across the five samples.

6.2.2   Results and discussion

Spectroscopic T_2 and ADC mean values and their SD of water and fat components in excised bone samples are reported in table 6.1.

	$(\mathbf{T_2 \pm SD})$(ms)	$(\mathbf{ADC \pm SD})(m^2/s)$
H$_2$O at 4.7 ppm	19 ± 7	$(4.2 \pm 1.8)E\text{-}10$
Fats at 5.3 ppm	72 ± 36	$(5.0 \pm 0.6)E\text{-}12$
Fats at 1.3 ppm	65 ± 16	$(5.3 \pm 0.3)E\text{-}12$

Table 6.1: Spectroscopic evaluation of excised calf samples [112].

Data show that T_2 and ADC of the water component (centered at 4.7

(a) Water component

	Water	$(\mathbf{T}_2 \pm \mathbf{SD})$	$(\mathbf{ADC} \pm \mathbf{SD})$	$(\mathbf{G}_i \pm \mathbf{SD})$	$(\mathbf{T}_2^{true} \pm \mathbf{SD})$
	(%)	(ms)	(m^2/s)	(mT/m)	(ms)
LTD	55	17.0 ± 3.0	$(19.0 \pm 0.4)E\text{-}10$	222 ± 131	17.9 ± 1.0
ITD	47	15.0 ± 2.3	$(7.0 \pm 0.4)E\text{-}10$	282 ± 134	15.2 ± 0.5
HTD	97	14.8 ± 0.4	$(1.6 \pm 0.1)E\text{-}10$	803 ± 181	16.0 ± 0.3

(b) Fat component

	Fat	$(\mathbf{T}_2 \pm \mathbf{SD})$	$(\mathbf{ADC} \pm \mathbf{SD})$	$(\mathbf{G}_i \pm \mathbf{SD})$	$(\mathbf{T}_2^{true} \pm \mathbf{SD})$
	(%)	(ms)	(m^2/s)	(mT/m)	(ms)
LTD	45	42.3 ± 6.2	$(5.3 \pm 0.3)E\text{-}12$	760 ± 195	43.0 ± 4.8
ITD	53	39.7 ± 4.0	$(5.9 \pm 0.3)E\text{-}12$	727 ± 437	44.0 ± 5.3
HTD	3	31.6 ± 6.0	$(5.4 \pm 0.2)E\text{-}12$	904 ± 119	37.5 ± 9.8

Table 6.2: Results from one excised calf sample: (a) water component and (b) fat component [112].

ppm) are significantly lower and higher respectively than those of fat components (centered at 5.3 ppm and 1.3 ppm). This allows us to discriminate clearly between the two components (water and fat). Specifically, T_2 values of water and fat are respectively consistent with those previously reported [113]. Similarly, ADCs of fat components, which are approximately two order of magnitude lower than those of water molecules, fit well with those recently reported by other authors [114].

In table 6.2, mean values (and their SD) of T_2, ADC, G_i and T_2^{true} are reported for the water component obtained in LTD, ITD and HTD locations of one sample (performing an average of values extracted from each slice belonging to a single location). In table 6.2, the corresponding results for the fat component are reported. The water ADC showed a decreasing trend proportional to the increase of trabecular density; thus, water mobility is more restricted in regions where the trabeculae are smaller. Conversely, it is evident from table 6.2 that the fat ADC is not sensitive to increase in trabecular density. Water G_i increases proportionally with the increase in TB density, while fat G_i is characterized by an opposite trend and does not allow discrimination between LTD and ITD.

Figure 6.4 displays different types of behavior of water and fat

G_i as a function of the distance (in voxels) between the TB marrow
interface and the internal part of the trabecular pore. G_i values were
derived using a fitting procedure, while ADC values were derived from
diffusion-weighted images. According to our findings, water G_i is cha-
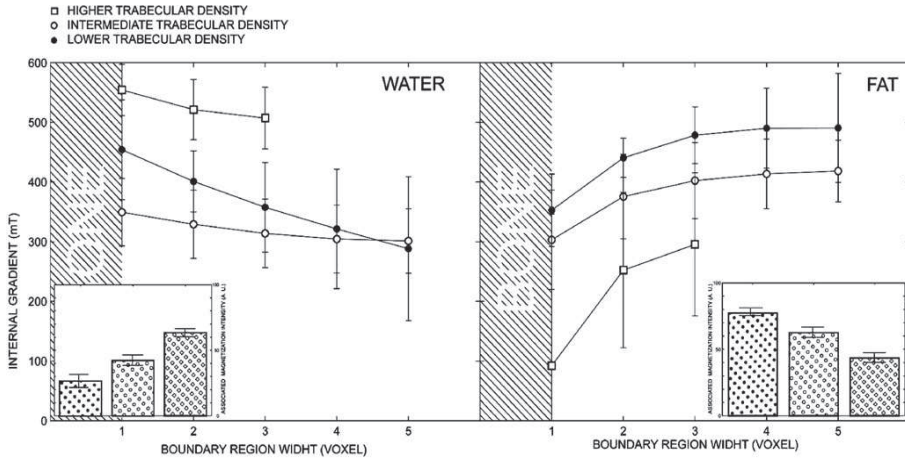

Figure 6.4: Behavior of water (left) and fat G_i (right) as a function of
increasing voxel number ranging from regions with one pixel (located
close to the bone surface) to regions constituted by five pixels (from
the bone surface to the pore center) [112]. Results are reported for
HTD (empty squares), ITD (empty circles) and LTD (filled circles). In
regions with HTD, the last two points are missing because the trabecular
interspaces were not large enough to allow a boundary region (which is
wider than three pixels) to be drawn.

racterized by a decreasing trend when moving from zones adjacent to
the trabecula to zones located in the center of the inter-trabecular space.
This behavior was observed in each of the three locations characterized
by different TB densities. When comparing G_i magnitude between the
three locations, it was otherwise evident that G_i in the HTD location
is higher than that extracted from the other two locations (ITD and
LTD). Conversely, fat compared to water G_i revealed an opposite be-
havior. In the latter case, G_i was characterized by an increasing trend
when moving from voxels adjacent to trabeculae to those located in the
center of the inter-trabecular space. In the insets of figure 6.4, mean
magnetization intensities are reported for fat and water components as

derived from the fitting procedure. Water concentration is higher in the HTD slices and decreases proportionally with the reduction of trabecular density (i.e. in ITD and in LTD).

ADC values and their magnetic susceptibility are the key parameters accounting for the different types of behavior of water and fat G_i (see Fig. 6.4 and 6.5). The water ADC is approximately two orders of magnitude higher than the fat ADC. As a consequence, water molecules compared to fat molecules are characterized by a faster motion. According to Einstein's relation $\langle r \rangle^2 = 2Dt$, which links the mean square spatial range spanned by diffusing molecules (characterized by a certain diffusion coefficient D at a diffusion time t), water spins travel a distance of the order of tenths of microns (calculated using the diffusion times Δ employed in this study). Conversely, the displacement of protons in fat lies in the sub-micron range. Moreover, water and fat are characterized by different magnetic susceptibilities: $\chi_{water} = -9.05x10^{-6}$ and $\chi_{fat} = -8.44x10^{-6}$ (SI units) [115], while bone tissue is believed to be characterized by $\chi_{bone} = -11x10^{-6}$ [116].

The G_i belonging to protons in water is sensitive to differences in magnetic susceptibility in the range of the pixel dimension. As expected, G_i shows a decreasing trend when moving from the bone-bone marrow interface to the pore center. Indeed, the difference in water-bone susceptibility represents the main source of water G_i. Conversely, protons in fat are sensitive to differences in magnetic susceptibility ranging at least from two orders of magnitude less than the pixel size. For this reason, fat G_i measured in this study cannot be attributed to the bone-bone marrow interface. Fat G_i magnitude is better explained by the difference in magnetic susceptibility between fat and water. The increasing trend of fat G_i values (when moving from the bone-bone marrow interface to the pore center) can thus be ascribed to a different rearrangement of fat molecules. In the central zone of each pore, there is a higher concentration of fat molecules characterized by a lower molecular motion than that of water molecules. As a consequence, fat G_i in the center of the pore assumes higher values than those observed nearby the bone surface. Indeed, in this latter location, there is a reduced concentration of fat molecules. This means that a correspondingly higher concentration of water molecules (characterized by faster motion) mod-

ulates fat G_i by reducing its values. This scenario fits well with the
hypothesized distribution of bone marrow filling trabecular pores, for
which we could say that 'water wets' the surface of bone pores. On the
other hand, fat molecules, due to their hydrophobic nature, are mainly
rearranged to lie in the central zone of the pore. As shown in figure 6.5,
water and fat G_i behavior in the boundary and inner regions of LTD
pores support this hypothesis. In the figure, water and fat G_i behavior
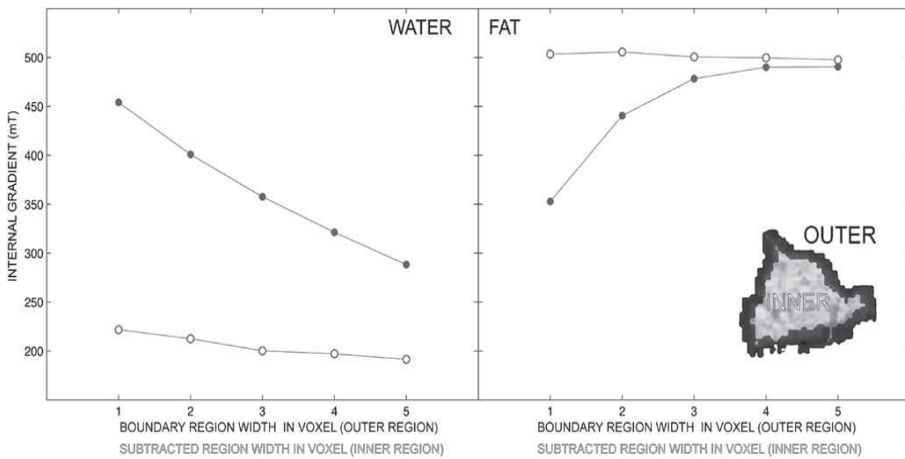

Figure 6.5: Water G_i (left) and fat G_i (right) behavior for LTD in the
boundary region (filled circles) and in the inner region (empty circles)
as a function of increasing boundary region width (which corresponds
to a decrease of the inner region width) [112]. The size of each pixel is
27 μm.

(expressed as a function of increasing pixel width) of the boundary re-
gion are compared to those measured from the inner region. G_i values
of both water and fat bone marrow components move toward an asymp-
totic value which is very close to that obtained in the central zone of
the trabecular pore.

  This observation confirms that water G_i variation is mainly due
to bone-bone marrow interface susceptibility properties. Therefore, wa-
ter G_i might be considered as a surrogate marker of the TB structure.
The asymptotic G_i values reached by the fat component were higher
when compared to those reached by the water component. Again, the
difference in the diffusion coefficient between fat and water might ex-

plain these results. As water molecules, compared to fat molecules, are associated with a faster diffusive motion during the experimental diffusion time, water spins are more dependent on motional averaging. As a consequence, the susceptibility dephasing effect which affects the SE signal of water is partially averaged. This peculiar behavior of water/fat systems has already been investigated and verified elsewhere [117]. To support the hypothesis that water concentration is higher in the boundary zone of pores, while fat is more concentrated in the central zone of pores, mean magnetization, extracted from the fit and associated with water (left) and fat (right) quantities in the first three voxels of the boundary regions, is reported in figure 6.6. Mean magnetization values
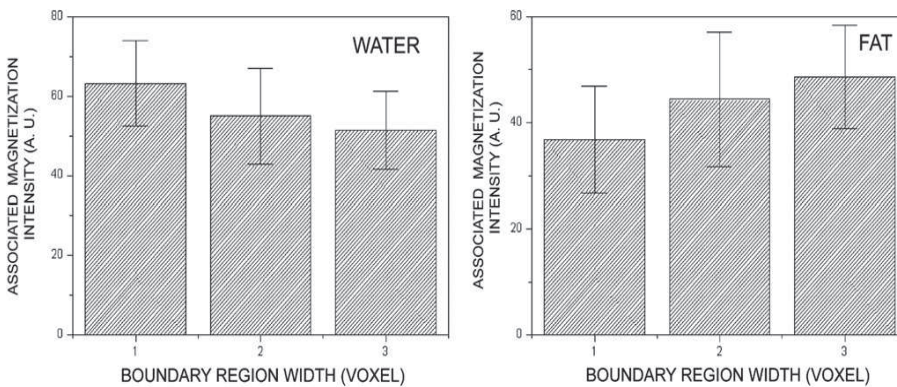
Figure 6.6: Mean magnetization values arising from the bi-exponential fit associated with water (left) and fat (right) versus boundary region width, expressed as a distance in voxels from the bone/marrow boundary [112]. The average is performed across all samples. LTD location was considered in all experimental samples.

and their corresponding SD values were obtained from all five samples belonging to different calves. Mean magnetization values associated with each voxel's zone of the boundary region are statistically different (p=0.05).

Data reported in figure 6.6 demonstrate that in each pore of spongy bone, the quantities of water molecules at the bone-bone marrow interface are higher than that of fat molecules. As a consequence, in spongy bone (filled with bone marrow), the measurements of water MR parameters (such as G_i, $T_2^\star$ or ADC) best provide information on

TB density.

In figure 6.7 mean G_i values and their SD, obtained from the five samples as a function of their TB density, are reported. The graph in the inset of figure 6.7 shows a positive linear correlation between water G_i and TB densities (Pearson's correlation coefficient $r = 0.71$). The
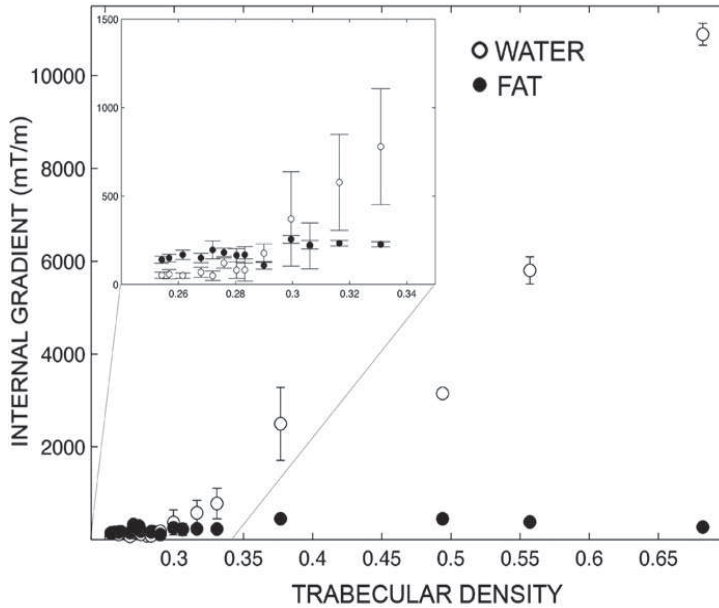
Figure 6.7: Water G_i behavior (empty circles) and fat G_i behavior (filled circles) as a function of trabecular density obtained as the ratio between the number of voxels belonging to the boundary perimeter (N_p) and the number of voxels of the whole area (N_a) [112]. The mean G_i values were calculated in a boundary region of three voxels wide. In the figure inset a zoom is displayed for TB densities ranging from 0.25 to 0.34.

large SD associated with water G_i mean values is mainly due to differences in water content between the five samples. The strong variation of water ADC is likely due to the small differences in water-fat content percentages across samples. The smaller are the ADC SDs, the larger are the SDs of G_i. Conversely, the fat ADC changes less as a function of water-fat percentage variation.

Finally, T_2, ADC, G_i and T_2^{true} mean values and their SDs obtained from the entire slice area from each of the selected locations

	$(\mathbf{T}_2 \pm \mathbf{SD})$	$(\mathbf{ADC} \pm \mathbf{SD})$	$(\mathbf{G}_i \pm \mathbf{SD})$	$(\mathbf{T}_2^{true} \pm \mathbf{SD})$
	(ms)	(m^2/s)	(mT/m)	(ms)
LTD	22.6 ± 9.7	$(4.0 \pm 0.7)E\text{-}10$	263 ± 68	30.7 ± 3.3
ITD	22.0 ± 5.7	$(3.8 \pm 1.2)E\text{-}10$	411 ± 102	28.1 ± 2.9
HTD	8.7 ± 2.8	$(5.3 \pm 1.6)E\text{-}10$	675 ± 183	8.3 ± 1.2

Table 6.3: Results obtained from excised calf samples without discriminating between water and fat [112].

(averaging on the five samples) are reported in table 6.3. G_i and T_2^{true} were extracted from the fit by function 3.23 (the second part of formula), while T_2 and ADC represent values obtained by direct measures. Results reported in table 6.3 are from an additional analysis in which we did not discriminate between fat and water components. This means that both components contribute, with different modalities, to the total fitted signal. However, the acquisition parameters chosen for this experiment were intentionally optimized to focus on the water signal (for example, b values from 0 to 10 000 s mm^{-2} were chosen to detect the typical water ADC but not the fat ADC). This means that there is only a minimal weight of the fat component in the determined results reported in table 6.3.

T_2 and ADC values did not discriminate between LTD, ITD and HTD. Conversely, T_2^{true} was characterized by a decreasing trend when moving from LTD to HTD, while G_i showed different values in the three locations with different TB densities. In bone marrow, T_2 is mainly dependent on the relative proportion of fat and water protons (which are characterized by different transverse relaxation times), as well as from the TB density. The ADC depends on the interstitial spaces between bone and fat where water diffuses. G_i assumes a higher value for higher trabecular densities, as expected by water G_i values reported in table 6.3, which are due to differences in magnetic susceptibility at the bone-water interface. Results reported in table 6.3 represent a preliminary test at high field to investigate the feasibility of including G_i measurements within clinical protocols (i.e. collection of T_2- weighted images and ADC maps). G_i would add useful information by discriminating between different TB densities.

6.3   *In vivo* experiments

6.3.1   Materials and methods

For every volunteer (see section 4.2), we acquired sagittal view images obtained on the same slices (5 mm thickness) and by using the same foot position. FLASH (Fast Low Angle Shot) images and MCSE (Multi Contrast Spin Echo) images at various *TE*s were acquired to evaluate $T_2^\star$ and T_2 respectively. The imaging parameters used for MCSE images at 3.0 T were: *TE* (echo time)=20,30,40,50,80,100 ms, *BW* (bandwidth)= 130 Hz/pixel, square *FOV* (field of view)=192 mm, matrix=256x256, resolution=0.75x0.75x5 mm^3; while for FLASH images the following parameters were used at 3.0 T: *FA* (flip angle)=30°, *TE*=5,7,10,20 ms, *BW*=260 Hz/pixel, square *FOV*=192 mm, matrix= 128x128, resolution=1.5x1.5x5 mm^3. Finally *TR* (repetition time)=1500 ms and *NS* (number of scan)=1 were used in all acquisitions.

We focused our attention on the whole calcaneus, the whole talus and on the *AC*, *ST*, *TC* and *CC* regions (see section 5.2). $T_2^\star$ and T_2 from FLASH and MCSE images, respectively were obtained by performing a mono-exponential fit of the mean intensities of every selected ROI at the different *TE*s (see formula 3.21 for $T_2^\star$ evaluation; see the first part of formula 3.23 for T_2 evaluation). From MCSE images, the equation 3.23 (the second part of formula), with four parameters to estimate (the signal intensity at *TE*=0, T_2^{true}, $\Omega = \frac{1}{12}\gamma^2 G_i^2 D$ and an additive constant), was fitted by a complex mono-exponential curve with the mean intensities of every selected ROI at the different *TE*s; with one of these estimated parameters (Ω), the internal gradient (G_i) of each ROI was calculated by substituting the correspondent measured *ADC* value (see section 5.3). A modified Levenberg-Marquardt nonlinear regression fit-type function was used.

$T_2^\star$, T_2 and G_i values of each region, were averaged across the subjects for each bone density group (normal, osteopenia and osteoporosis, labeled 1, 2 and 3 respectively) and for the control group (labeled *C*) and their standard deviations were calculated. $T_2^\star$, T_2 and G_i values from postmenopausal women were also graphed, for each region, with their averages and were plotted versus marrow fat content *Mfc* values obtained in the previous chapter (see section 4.3). For each re-

gion, the mean $T_2^\star$, T_2 and G_i values were compared among the three bone density groups and between the control and normal group with the one-way analysis of variance test (one-way ANOVA) and Pearson correlation coefficients (r) were calculated to assess the linear relationship between pairs of variables (among *T-score*, *Age*, *Mfc*, *ADC*, $T_2^\star$, T_2 and G_i variables) for all postmenopausal subjects and for all subjects of each bone density group. A p value of less than 0.05 was considered to indicate a statistically significant difference.

6.3.2 Results and discussion

Osteoporosis induces an increase in trabecular bone spacing, observable with an increase in bone marrow MR signal intensity (see Fig. 6.8), which reduces the spatial field inhomogeneity and thus considerably prolongs $T_2^\star$ and G_i (see eqn. 3.24).

The results reported in Tab. 6.4 and in the graphs in Fig. 6.9
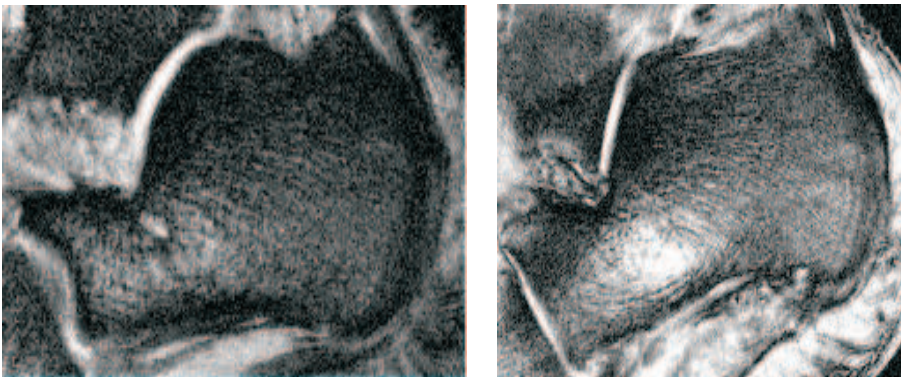
Figure 6.8: Sagittal high resolution FLASH images at 3.0 T of calcaneus of two elderly women (60-years-old and normal bone density with T-score=-0.1 on the left and 67 and osteoporotic with T-score=-4.61 on the right) showing the higher bone marrow signal intensity in osteoporotic than in normal person, due to the higher trabecular bone spacing.

show that the mean $T_2^\star$ values of the three bone density groups increase as bone density decreases and these differences are statistically significant among the three groups in *AT*, *CC* and *CALCA* regions; *AT*, *CC* and *CALCA* are the only regions with statistically significant discrimination between normal and osteopenic group and *CALCA* is the best;

TC is the only region without statistically significant discrimination between osteopenic and osteoporotic group and ST is the best region to discriminate between these groups. Our mean $T_2^\star$ values in every calcaneal region agree with literature findings [3].

As is possible to observe in Tab. 6.4 and in Fig. 6.10, the mean T_2 values have no trend as bone density decreases and there isn't any statistically significant discrimination between groups, probably due to the poor dependence of the T_2 parameter on the G_i and ADC factors (see eqn. 3.23). Moreover, we can see that in Fig. 6.11 the mean G_i values of the three bone density groups decrease as bone density decreases and these differences are statistically significant among the three groups only in AT and ST regions; AT and ST are the only regions with statistically significant discrimination between normal and osteopenic group and ST is the best; TC and CC are, instead, the only regions without statistically significant discrimination between osteopenic and osteoporotic group and ST is the best region to discriminate between these groups.

Conversely, $T_2^\star$, T_2 and G_i values almost always don't point out any statistically significant difference between the control and normal group, in every analyzed region.

Observing the results in Tab. 6.4, mean $T_2^\star$ and G_i values also differ among calcaneal regions, in each group, being respectively highest and intermediate in the cavum calcanei (the lowest trabecular bone density region), lowest and highest in the subtalar (the highest trabecular bone density region) and intermediate and lowest values in the tuber calcanei regions, thus these parameters (especially the $T_2^\star$ parameter) give us information on local trabecular bone density. By their values, they moreover locate higher trabecular bone density in the whole talus than in the whole calcaneus and, instead, higher trabecular bone density in ST than in AC region.

For paired data of all postmenopausal subjects, we obtained a moderate significant negative correlation between T-$score$ and $T_2^\star$ in AC, AT, $CALCA$ and ST regions ($-0.564 \leq r \leq -0.515$, $p <$ 0.01) and a low significant negative correlation in all the other analyzed regions (see Tab. 6.5 and 6.6); almost never significant correlation between T-$score$ and T_2; a moderate significant positive correlation be-

Figure 6.9: Graphs show $T_2^\star$ values, for three bone density groups (normal bone density, osteopenia, and osteoporosis), in the whole calcaneus ($CALCA$), the whole talus (AT) and in the ST, AC, TC and CC regions. Mean $T_2^\star$ values increase as bone density decreases; AT, CC and $CALCA$ are the only regions with statistically significant discrimination between normal and osteopenic group and $CALCA$ is the best; TC is the only region without statistically significant discrimination between osteopenic and osteoporotic group and ST is the best region to discriminate between these groups. Horizontal bar = mean value for each group (see Tab. 6.4). (Normal: ◆-blue, osteopenia: ■-green, osteoporosis: ▲-red).
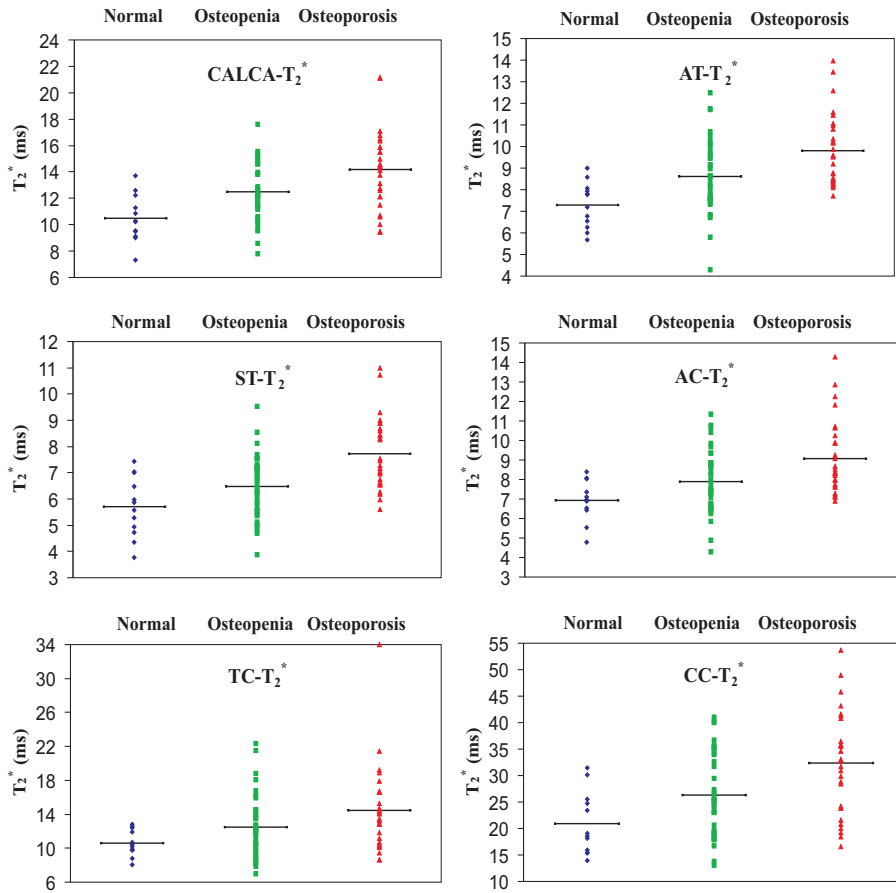
Figure 6.10: Graphs show T_2 values, for three bone density groups (normal bone density, osteopenia, and osteoporosis), in the whole calcaneus ($CALCA$), the whole talus (AT) and in the ST, AC, TC and CC regions. Mean T_2 values have no trend as bone density decreases and there isn't any statistically significant discrimination between groups. Horizontal bar = mean value for each group (see Tab. 6.4). (Normal: ♦-blue, osteopenia: ■-green, osteoporosis: ▲-red).
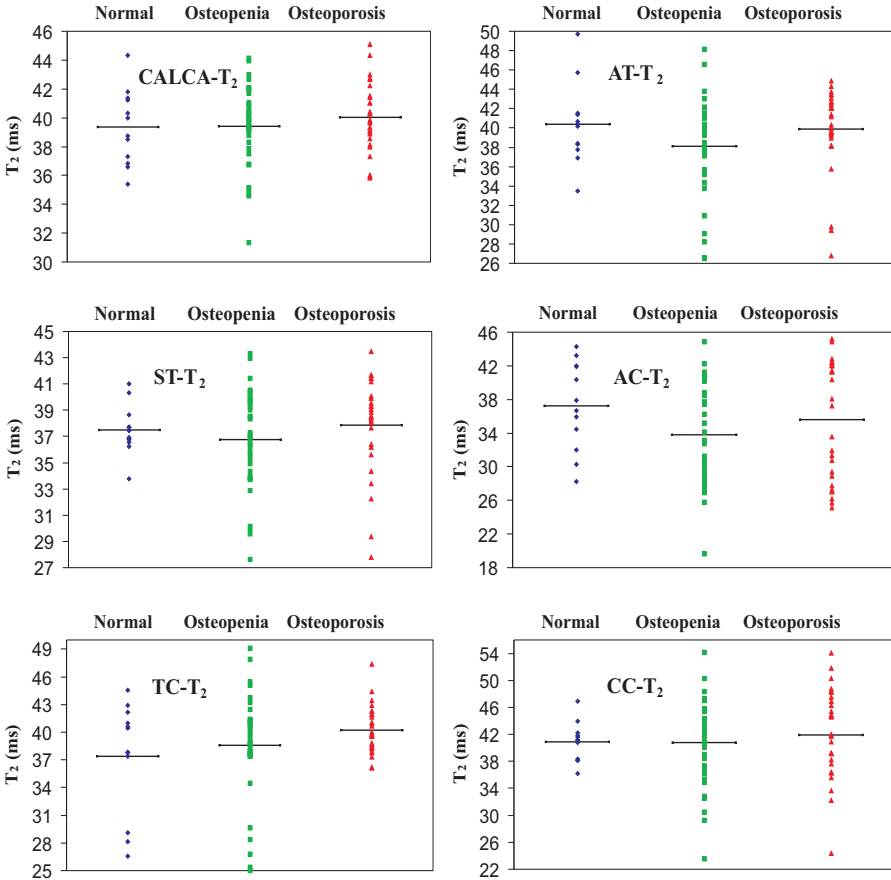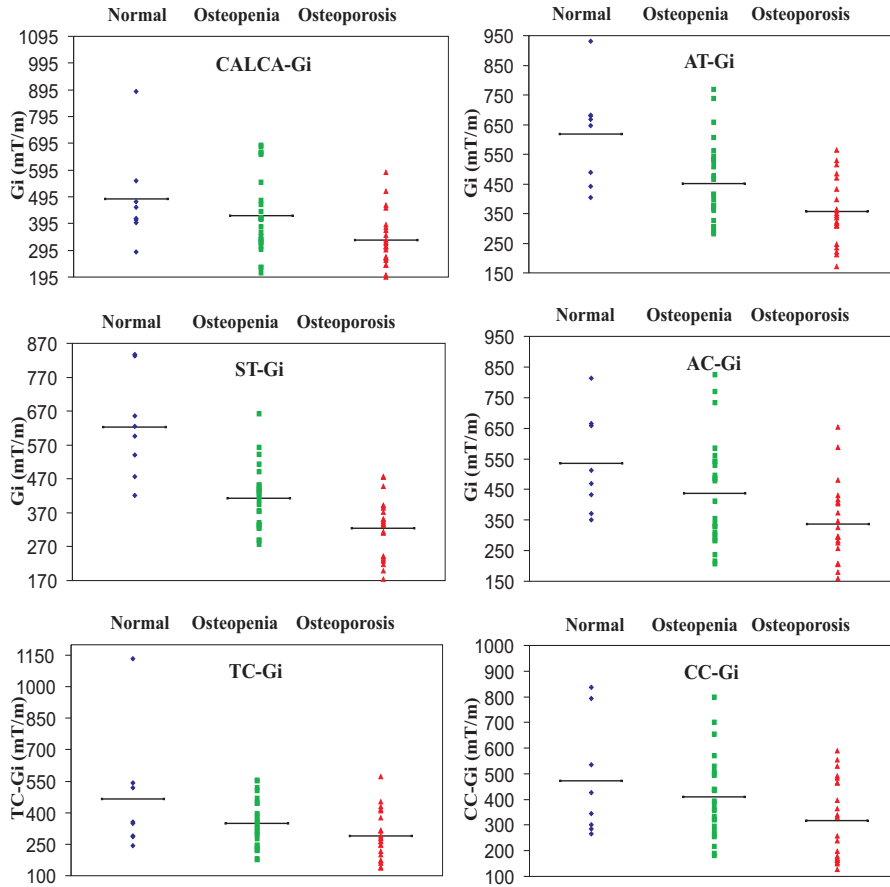
Figure 6.11: Graphs show G_i values, for three bone density groups (normal bone density, osteopenia, and osteoporosis), in the whole calcaneus ($CALCA$), the whole talus (AT) and in the ST, AC, TC and CC regions. Mean G_i values decrease as bone density decreases; AT and ST are the only regions with statistically significant discrimination between normal and osteopenic group and ST is the best; TC and CC are the only regions without statistically significant discrimination between osteopenic and osteoporotic group and ST is the best region to discriminate between these groups. Horizontal bar = mean value for each group (see Tab. 6.4). (Normal: ◆-blue, osteopenia: ■-green, osteoporosis: ▲-red).

Site-Parameter	Ranking (1-2-3)	C (n = 6; 5*)	1 (n = 12; 8*)	2 (n = 37; 25*)	3 (n = 28; 22*)	p value (C vs 1)	p value (1 vs 2)	p value (2 vs 3)	p value (1 vs 3)
AC-T$_2^\star$ (ms)	U	6.94 ± 0.93	6.92 ± 1.04	7.89 ± 1.63	9.08 ± 1.90	ns	ns	**	**
AC-T$_2$ (ms)	N	31.02 ± 4.55	37.26 ± 5.28	33.77 ± 6.07	35.63 ± 7.04	*	ns	ns	ns
AC-G$_i$ (mT/m)	D	502.84 ± 204.49	534.12 ± 163.06	437.20 ± 171.94	337.25 ± 129.43	ns	ns	*	**
AT-T$_2^\star$ (ms)	U	6.88 ± 1.02	7.30 ± 1.05	8.61 ± 1.68	9.81 ± 1.67	ns	*	**	***
AT-T$_2$ (ms)	N	31.45 ± 4.15	40.37 ± 4.19	38.13 ± 5.00	39.88 ± 4.50	**	ns	ns	ns
AT-G$_i$ (mT/m)	D	502.04 ± 250.67	617.75 ± 169.72	450.88 ± 138.86	356.56 ± 110.47	ns	**	*	***
ST-T$_2^\star$ (ms)	U	5.31 ± 0.79	5.70 ± 1.15	6.49 ± 1.18	7.72 ± 1.36	ns	ns	***	***
ST-T$_2$ (ms)	N	35.79 ± 2.72	37.50 ± 1.90	36.76 ± 3.72	37.85 ± 3.67	ns	ns	ns	ns
ST-G$_i$ (mT/m)	D	562.92 ± 166.69	623.07 ± 151.66	413.51 ± 93.05	325.17 ± 87.19	ns	***	**	***
TC-T$_2^\star$ (ms)	U	10.41 ± 1.72	10.62 ± 1.52	12.51 ± 3.67	14.48 ± 5.04	ns	ns	*	*
TC-T$_2$ (ms)	N	38.20 ± 5.75	37.37 ± 6.09	38.59 ± 5.54	38.25 ± 2.54	ns	ns	ns	ns
TC-G$_i$ (mT/m)	D	355.31 ± 130.97	464.56 ± 291.30	348.61 ± 114.61	287.90 ± 114.16	ns	*	**	*
CC-T$_2^\star$ (ms)	U	25.74 ± 6.99	20.97 ± 5.96	26.36 ± 7.83	32.37 ± 9.66	ns	*	**	**
CC-T$_2$ (ms)	N	43.44 ± 6.40	40.86 ± 2.91	40.82 ± 6.30	41.96 ± 6.71	ns	ns	ns	ns
CC-G$_i$ (mT/m)	D	550.24 ± 190.82	473.16 ± 228.59	409.03 ± 158.26	317.19 ± 156.11	ns	ns	*	*
CALCA-T$_2^\star$ (ms)	U	11.07 ± 1.16	10.47 ± 1.78	12.48 ± 2.15	14.18 ± 2.98	ns	**	*	***
CALCA-T$_2$ (ms)	N	40.03 ± 1.95	39.36 ± 2.60	39.39 ± 2.75	40.03 ± 2.37	ns	ns	ns	ns
CALCA-G$_i$ (mT/m)	D	459.96 ± 54.26	486.20 ± 179.73	425.13 ± 147.27	333.84 ± 100.08	ns	ns	*	**

Table 6.4: The mean values of $T_2^\star$, T_2 and G_i variables, with their standard deviations are reported for the control group and for each bone density group. The comparison of these values among the three bone density groups and between the control and normal group, by p values obtained with the one-way analysis of variance test (one-way ANOVA), and their ranking trends among the three bone density groups are also reported. Notes: 1. Data are mean ± 1 standard deviation; 2. U (upward ranking); D (downward ranking); N (no ranking); 3. C (Control group); 1 (Normal); 2 (Osteopenia); 3 (Osteoporosis); 4. ns ($p \geq 0.05$); * ($p < 0.05$); ** ($p < 0.01$); *** ($p < 0.001$); 5. AC (the talar region close to calcaneus); AT (the whole talus); ST (the subtalar region of calcaneus); TC (the tuber calcanei region); CC (the cavum calcanei region); $CALCA$ (the whole calcaneus); 6. * (number of subjects analyzed for G_i measures).

Parameter	T-score	Age	Mfc	AC-$T_2^\star$	AC-T_2	AC-ADC	AC-G_i
T-score	1	$-0.425**(2)$	0.080	$-0.515**(3)$	0.015	$-0.316*(2)$	$0.390**(2)$
Age		1	0.102	0.170	0.145	0.155	-0.122
Mfc			1	0.180	-0.064	-0.148	0.124
AC-$T_2^\star$				1	-0.005	0.124	-0.266
AC-T_2					1	-0.244	$0.580**(3)$
AC-ADC						1	$-0.714**(4)$
AC-G_i							1

Parameter	T-score	Age	Mfc	AT-$T_2^\star$	AT-T_2	AT-ADC	AT-G_i
T-score	1	$-0.425**(2)$	0.080	$-0.564**(3)$	-0.129	$-0.376**(2)$	$0.501**(3)$
Age		1	0.102	$0.252*(1)$	0.158	0.214	-0.235
Mfc			1	-0.006	-0.126	-0.163	0.180
AT-$T_2^\star$				1	$0.331**(2)$	0.026	-0.161
AT-T_2					1	-0.127	$0.351*(2)$
AT-ADC						1	$-0.724**(4)$
AT-G_i							1

Parameter	T-score	Age	Mfc	CALCA-$T_2^\star$	CALCA-T_2	CALCA-ADC	CALCA-G_i
T-score	1	$-0.425**(2)$	0.080	$-0.555**(3)$	-0.141	$-0.463**(2)$	$0.318*(2)$
Age		1	0.102	0.133	-0.005	0.108	-0.194
Mfc			1	0.126	0.006	$-0.301*(2)$	-0.048
CALCA-$T_2^\star$				1	0.184	0.245	0.033
CALCA-T_2					1	0.153	0.059
CALCA-ADC						1	$-0.541**(3)$
CALCA-G_i							1

Table 6.5: Pearson correlation coefficient test results (r) between pairs of variables (among T-$score$, Age, Mfc, $T_2^\star$, T_2, ADC and G_i variables, in AC, AT and $CALCA$ regions) for all postmenopausal subjects. Notes: 1. Data are Pearson correlation coefficients (r); 2. $*$ ($p < 0.05$); $**$ ($p < 0.01$); 3. (1) little ($0 \leq r \leq 0.29$), (2) low ($0.3 \leq r \leq 0.49$), (3) moderate ($0.5 \leq r \leq 0.69$), (4) high ($0.7 \leq r \leq 0.89$), (5) very high ($0.9 \leq r \leq 1$).

Parameter	T-score	Age	Mfc	ST-T$_2^\star$	ST-T$_2$	ST-ADC	ST-G$_i$
T-score	1	$-0.425**(2)$	0.080	$-0.552**(3)$	-0.002	$-0.488**(2)$	$0.635**(3)$
Age		1	0.102	0.196	-0.067	0.135	$-0.306*(2)$
Mfc			1	0.102	0.033	-0.250	0.110
ST-T$_2^\star$				1	-0.028	0.183	-0.217
ST-T$_2$					1	0.023	-0.051
ST-ADC						1	$-0.661**(3)$
ST-G$_i$							1

Parameter	T-score	Age	Mfc	TC-T$_2^\star$	TC-T$_2$	TC-ADC	TC-G$_i$
T-score	1	$-0.425**(2)$	0.080	$-0.403**(2)$	$-0.265*(1)$	$-0.350**(2)$	$0.305*(2)$
Age		1	0.102	0.167	0.066	0.100	-0.175
Mfc			1	0.095	0.135	-0.143	-0.050
TC-T$_2^\star$				1	$0.296**(2)$	0.249	-0.121
TC-T$_2$					1	0.048	0.168
TC-ADC						1	$-0.615**(3)$
TC-G$_i$							1

Parameter	T-score	Age	Mfc	CC-T$_2^\star$	CC-T$_2$	CC-ADC	CC-G$_i$
T-score	1	$-0.425**(2)$	0.080	$-0.427**(2)$	-0.011	$-0.497**(3)$	$0.341*(2)$
Age		1	0.102	0.192	-0.005	0.177	-0.183
Mfc			1	0.150	0.142	-0.248	0.109
CC-T$_2^\star$				1	$0.268*(1)$	0.177	0.066
CC-T$_2$					1	-0.051	$0.317*(2)$
CC-ADC						1	$-0.603**(3)$
CC-G$_i$							1

Table 6.6: Pearson correlation coefficient test results (r) between pairs of variables (among T-score, Age, Mfc, T_2, $T_2^\star$, ADC and G_i variables, in ST, TC and CC regions) for all postmenopausal subjects. Notes: 1. Data are Pearson correlation coefficients (r); 2. $*$ ($p < 0.05$); $**$ ($p < 0.01$); 3. (1) little ($0 \leq r \leq 0.29$), (2) low ($0.3 \leq r \leq 0.49$), (3) moderate ($0.5 \leq r \leq 0.69$), (4) high ($0.7 \leq r \leq 0.89$), (5) very high ($0.9 \leq r \leq 1$).

tween T-*score* and G_i in AT and ST regions ($0.501 \leq r \leq 0.635$, p < 0.01) and a low significant positive correlation in all the other analyzed regions. Even if $T_2^\star$ and G_i parameters are able to distinguish the three bone density groups, according to WHO criteria, they have a low or moderate significant correlation with T-*score* values and this demonstrates that they don't depend only on the bone density but also on other factors bound to the bone quality, as previous asserted. No significant correlation between the three parameters ($T_2^\star$, T_2 and G_i) and Mfc and almost never significant correlation between them and *Age* (only a positive little for $T_2^\star$ in AT and a negative low for G_i in ST) was observed. A high significant negative correlation between Mfc and G_i was obtained in TC region ($r = -0.776$, $p < 0.05$) and in the whole calcaneus for the normal postmenopausal subjects ($r = -0.733$, $p < 0.05$) and in the whole calcaneus for the control group ($r = -0.88$, $p < 0.05$). Moreover, a high significant negative correlation between G_i and ADC was obtained in AC and AT regions and a moderate in all the other regions.

In Fig. 6.12 it is possible to notice that for low bone density, $T_2^\star$ values increase as Mfc increases; for high bone density, $T_2^\star$ values almost always instead decrease as Mfc increases.
Taking into consideration the whole calcaneus and its regions only, in which it was evaluated the Mfc, in the Fig. 6.13 it is possible to notice that for high bone density, G_i values decrease as Mfc increases; for low bone density, G_i values instead increase as Mfc increases. Thus, for high bone density, as the marrow fat content increases, the linked trabecular bone density and the spatial magnetic field inhomogeneities decreases, so the G_i decreases; for low bone density, G_i parameter seems to become more sensible to the local magnetic susceptibility differences between the solid matrix of trabecular bone and the interstitial liquid bone marrow, because as the bone marrow fat component increases, these local differences and therefore the local G_i increase (see subsection 6.2.2). In the same graphs, the straight lines of the three bone density groups, obtained by the linear regression analysis, tend to a common intermediate G_i value at highest Mfc values.

In table 6.4, the mean $T_2^\star$ values of the three bone density groups overlap when considering their SDs; the mean G_i values almost

always have the same behavior, only its values of the normal and os-
teoporotic groups in ST region don't overlap. Thus, as aforementioned,
the large standard deviation associated with mean $T_2^\star$ and G_i values as-
sessed in spongy bone tissue from healthy, osteopenic and osteoporotic
individuals does not allow the clinical use of $T_2^\star$ and G_i on a single
subject basis. According to our experimental results, $T_2^\star$ turned out to
be affected by the marrow fat content, a parameter that shows a huge
spread across different subjects. Some authors have suggested introduc-
ing corrections to account for variations in marrow composition [69].
However, to our knowledge, no-clinical studies involving these correc-
tions have been published so far. As for the ADC parameter, by the
last considerations, we instead can assert that the marrow fat content
evaluation might improve the diagnostic confidence of osteoporosis, by
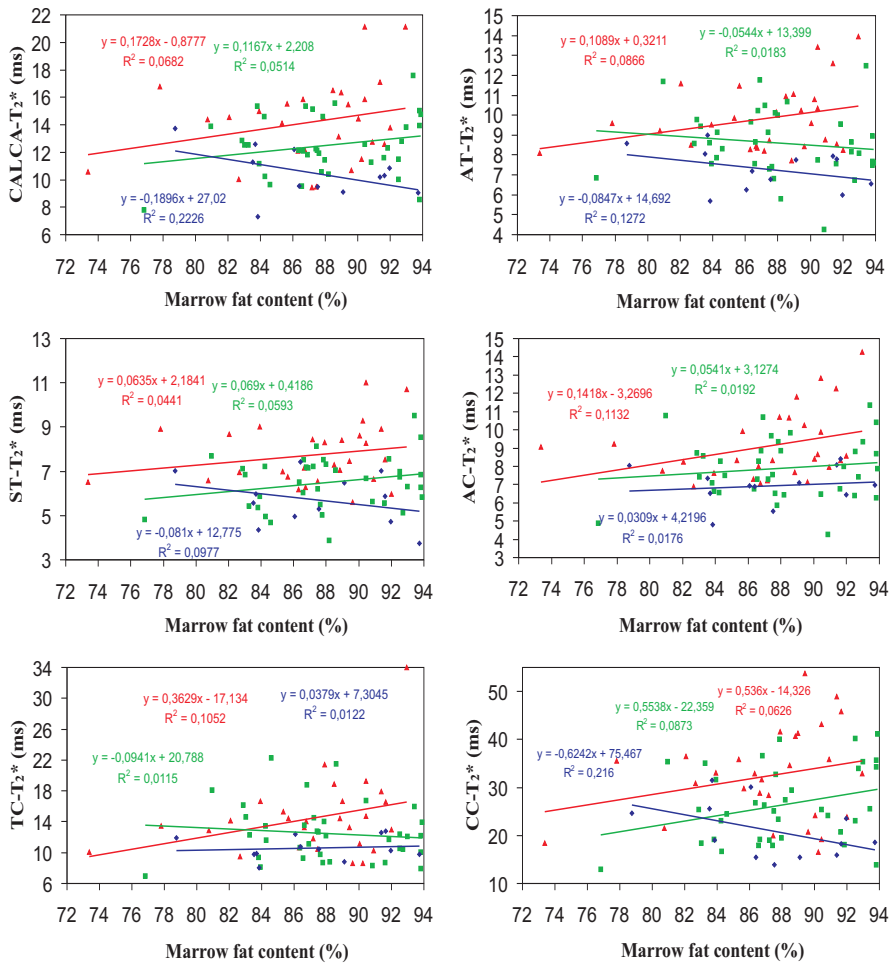G_i assessment of the calcaneal regions in subjects with lowest Mfc val-
ues.

Figure 6.12: For each investigated region and for each group, $T_2^\star$ and Mfc values of all postmenopausal subjects are plotted and examined by linear correlation with their coefficients of determination (R^2). (Normal: ◆-blue, osteopenia: ■-green, osteoporosis: ▲-red).

Figure 6.13: For each investigated region and for each group, G_i and Mfc values of all postmenopausal subjects are plotted and examined by linear correlation with their coefficients of determination (R^2). (Normal: ◆-blue, osteopenia: ■-green, osteoporosis: ▲-red).
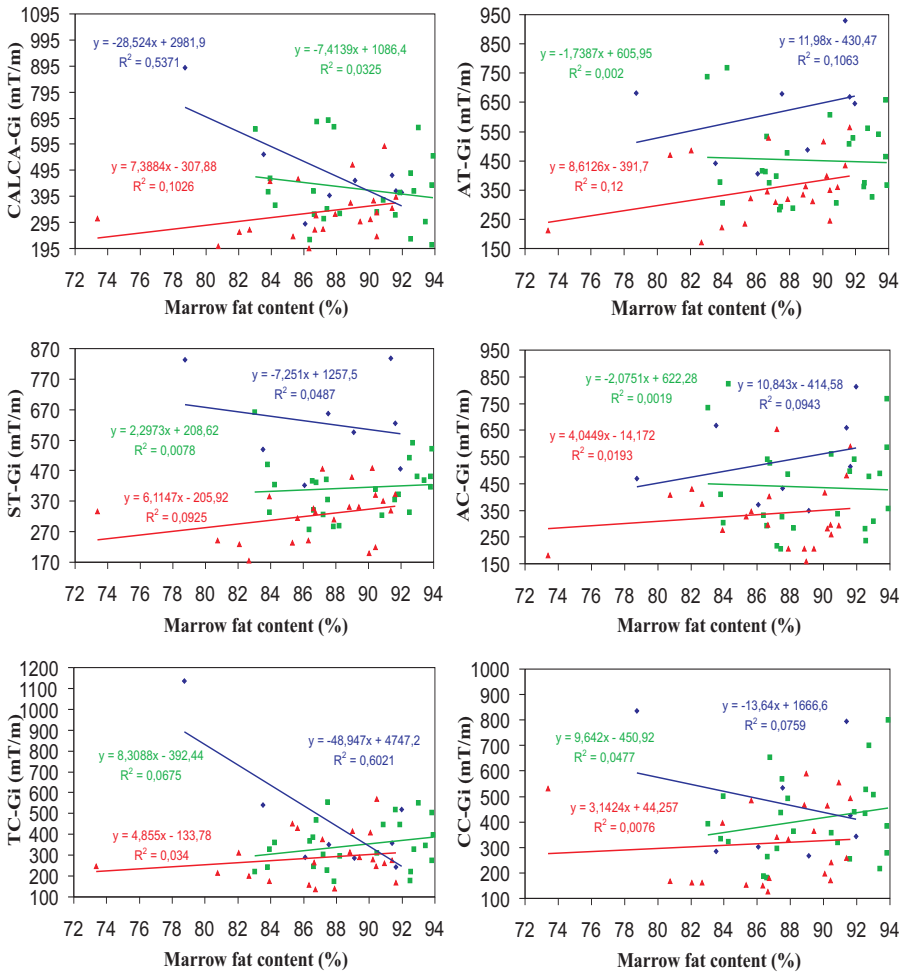
Chapter 7

The best Site-Parameter

In this chapter, analyzing the obtained results, we want to compare the potential ability of $T_2^\star$, T_2, ADC and G_i parameters to discriminate among healthy, osteopenic and osteoporotic individuals; then, by this evaluation we want to indicate the best parameter and the best heel spongy bone site by which to obtain the best discrimination.
Moreover, by a deeper analysis than the simple linear correlation, we want to identify the site-parameter couple which best classifies the subjects in the same way of T-$score$.

7.1 $T_2^\star$, T_2, ADC, G_i comparisons

To make the right comparisons, we summarize in table 7.1 the results obtained in tables 5.1 and 6.4 and associate to each site-parameter a discrimination code abc with a relative to the comparison of 1-2 groups (normal vs osteopenia), b for 2-3 groups (osteopenia vs osteoporosis), c for 1-3 groups (normal vs osteoporosis), where 0 means that the two group averages are not statistically significant ($p \geq 0.05$) and 1 means that they are significant ($p < 0.05$).

As aforementioned, observing the table 7.1 the mean values of $T_2^\star$, T_2, ADC and G_i variables are statistically significant among the three bone density groups (that is a 111 discrimination code) only in AT region for $T_2^\star$ and G_i, in ST region for ADC and G_i, in CC and $CALCA$ regions for $T_2^\star$; in particular, G_i variable assessed in ST region turns out to be the best site-parameter to discriminate among the three bone density groups with a $p < 0.001$ between normal and osteopenic

Site-Parameter	p value (1 vs 2)	p value (2 vs 3)	p value (1 vs 3)	Discrimination code 1-2-3
T-score	$* * *$	$* * *$	$* * *$	111
Age	ns	$**$	$**$	011
Mfc	ns	ns	ns	000
AC-T$_2^\star$	ns	$**$	$**$	011
AC-T$_2$	ns	ns	ns	000
AC-ADC	ns	ns	$**$	001
AC-G$_i$	ns	$*$	$**$	011
AT-T$_2^\star$	$*$	$**$	$* * *$	111
AT-T$_2$	ns	ns	ns	000
AT-ADC	ns	$*$	$**$	011
AT-G$_i$	$**$	$*$	$* * *$	111
ST-T$_2^\star$	ns	$* * *$	$* * *$	011
ST-T$_2$	ns	ns	ns	000
ST-ADC	$*$	$**$	$* * *$	111
ST-G$_i$	$* * *$	$**$	$* * *$	111
TC-T$_2^\star$	ns	ns	$*$	001
TC-T$_2$	ns	ns	ns	000
TC-ADC	ns	$*$	$*$	011
TC-G$_i$	ns	ns	$*$	001
CC-T$_2^\star$	$*$	$**$	$**$	111
CC-T$_2$	ns	ns	ns	000
CC-ADC	ns	$* * *$	$**$	011
CC-G$_i$	ns	ns	$*$	001
CALCA-T$_2^\star$	$**$	$*$	$* * *$	111
CALCA-T$_2$	ns	ns	ns	000
CALCA-ADC	ns	$**$	$* * *$	011
CALCA-G$_i$	ns	$*$	$**$	011

Table 7.1: The discrimination codes, achieved by the comparisons of the mean values of *T-score*, *Age*, Mfc, $T_2^\star$, T_2, ADC and G_i variables among the three bone density groups, by p values obtained with the one-way analysis of variance test, are reported for each investigated region. Notes: 1. 1 (Normal); 2 (Osteopenia); 3 (Osteoporosis); 2. ns ($p \geq 0.05$); $*$ ($p < 0.05$); $**$ ($p < 0.01$); $* * *$ ($p < 0.001$); 3. AC (the talar region close to calcaneus); AT (the whole talus); ST (the subtalar region of calcaneus); TC (the tuber calcanei region); CC (the cavum calcanei region); $CALCA$ (the whole calcaneus); 4. 0 means that the two averages are not statistically significant, 1 means that they are.

and between normal and osteoporotic groups and a $p < 0.01$ between osteopenic and osteoporotic groups.

Analyzing only the couple comparisons of the groups, $T_2^\star$ values from ST region and ADC values from CC region allow a better discrimination between osteopenic and osteoporotic subjects ($p < 0.001$), while G_i values from ST region, as just asserted, allow a better discrimination between normal and osteopenic subjects ($p < 0.001$).

If we investigate the ANOVA results for each variable, independently from the analyzed regions, we can see in table 7.2 that $T_2^\star$ has the highest absolute discrimination percentage (50%, that corresponds to have the 111 discrimination code in three regions among the six analyzed regions), the highest normal-osteopenia discrimination percentage (50%, that corresponds to have the 1*bc* discrimination code in three regions among the six analyzed regions), the highest or the highest ex-aequo osteopenia-osteoporosis discrimination percentage (83.3%, that corresponds to have the *a*1*c* discrimination code in five regions among the six analyzed regions), the highest or the highest ex-aequo normal-osteoporosis discrimination percentage (100%, that corresponds to have the *ab*1 discrimination code in six regions among the six analyzed regions).

If we instead analyze the ANOVA results for each region, independently

(%)	$T_2^\star$	T_2	ADC	G_i
Absolute discrimination	50.0	0.0	16.7	33.3
Discrimination 1-2	50.0	0.0	16.7	33.3
Discrimination 2-3	83.3	0.0	83.3	66.7
Discrimination 1-3	100.0	0.0	100.0	100.0

Table 7.2: ANOVA results for each variable, independently from the analyzed regions: absolute discrimination percentage; normal-osteopenia (1-2) discrimination percentage; osteopenia-osteoporosis (2-3) discrimination percentage; normal-osteoporosis (1-3) discrimination percentage.

from the analyzed parameters, we can see in table 7.3 that AT and ST regions have the highest absolute discrimination percentage (50%, that corresponds to have the 111 discrimination code for two parameters among the four analyzed parameters), the highest normal-osteopenia

(%)	AC	AT	ST	TC	CC	CALCA
Absolute discrimination	0.0	50.0	50.0	0.0	25.0	25.0
Discrimination 1-2	0.0	50.0	50.0	0.0	25.0	25.0
Discrimination 2-3	50.0	75.0	75.0	25.0	50.0	75.0
Discrimination 1-3	75.0	75.0	75.0	75.0	75.0	75.0

Table 7.3: ANOVA results for each region, independently from the analyzed parameters: absolute discrimination percentage; normal-osteopenia (1-2) discrimination percentage; osteopenia-osteoporosis (2-3) discrimination percentage; normal-osteoporosis (1-3) discrimination percentage.

discrimination percentage (50%, that corresponds to have the $1bc$ discrimination code for two parameters among the four analyzed parameters), the highest or the highest ex-aequo osteopenia-osteoporosis discrimination percentage (75%, that corresponds to have the $a1c$ discrimination code for three parameters among the four analyzed parameters), the highest or the highest ex-aequo normal-osteoporosis discrimination percentage (75%, that corresponds to have the $ab1$ discrimination code for three parameters among the four analyzed parameters).

7.2   Classification indexes

To identify the site-parameter couple which best classifies the subjects in the same way of *T-score*, we use the classification indexes. Nevertheless, contrary to *T-score* with its cut-off values defined by WHO, we haven't any standardized threshold values for each investigated parameter by which discriminate the subjects among the three bone density groups, by using the parameter value. However, it is possible to make some considerations.

Let's order the subjects by *T-score* decreasing values and define their classification basing on *T-score* values, then, considering a region of analysis, let's order the same subjects by parameter increasing or decreasing values, in accord with the trends outlined by the *ranking* parameter in tables 5.1 and 6.4 or by theoretical forecasts for *no ranking* cases (for example by G_i decreasing values or by T_2 increasing values).

It's not senseless to assert that if *T-score* and the analyzed parameter misure similar something, it's possible to redefine the classification of the subjects basing on parameter values, taking into account that the first 12 are normal, the second 37 are osteopenic, and the last 28 are osteoporotic subjects. Thus, every subject will have two classifications: by *T-score* value and by parameter value. Now, let's consider the first one method (*T-score*) like true ('gold standard') and the second one method (parameter) to test. By creating a 3x3 matching matrix, it's possible to calculate the classification indexes, that are the accord percentage between the two kinds of classifications (% *accord*) and, for every group, the sensibility (*Sens*), the specificity (*Spec*) and the positive (*PV+1*) and negative (*PV-1*) predictive value of the classification method to test; in each group, the sensibility and the specificity will have the same values of the positive predictive value and of the negative predictive value respectively, because, as defined, the number of normal, osteopenic and osteoporotic subjects are the same for the two methods. Let's perform this procedure to calculate the classification indexes for Age, Mfc, $T_2^\star$, T_2, ADC and G_i parameters in every analyzed region.

From graphs in Fig. 7.1 and 7.2 of the obtained results, we can notice that the sensibility and the positive predictive value for normal subjects show the highest variableness in every region, among the analyzed parameters; in particular, G_i parameter almost always shows the highest sensibility and positive predictive value for normal subjects.

Grouping in table 7.4 the highest index values and the relative site-parameter couples, we can see that the highest and considerable accord percentage (62.96%) with *T-score* method was obtained with *AT-G_i* couple; the highest sensibility (62.50%), specificity (93.62%), positive and negative predictive values to detect the normal subjects were obtained with *ST-G_i* couple; the highest sensibility (60.00% for osteopenic and 68.18% for osteoporotic subjects), specificity (66.67% for osteopenic and 78.79% for osteoporotic subjects), positive and negative predictive values to detect the osteopenic and to detect the osteoporotic subjects were obtained with *CC-ADC* couple.

The maximum and very high specificity and negative predictive value (93.62%), among the three groups, were obtained with *ST-G_i* couple for normal subjects; thus G_i quantification from the subtalar

Classification index	Maximum value (%)	Site-Parameter	
% accord	62.96	AT-G_i	-
Sens1	62.50	AT-G_i	ST-G_i
Sens2	60.00	AT-G_i	CC-ADC
Sens3	68.18	CC-ADC	-
Spec1	93.62	ST-G_i	-
Spec2	66.67	CC-ADC	-
Spec3	78.79	AT-G_i	CC-ADC
PV+1	62.50	AT-G_i	ST-G_i
PV-1	93.62	ST-G_i	-
PV+2	60.00	AT-G_i	CC-ADC
PV-2	66.67	CC-ADC	-
PV+3	68.18	CC-ADC	-
PV-3	78.79	AT-G_i	CC-ADC

Table 7.4: The highest index percentage values and the relative site-parameter couples are reported. Notes: 1. 1 (Normal); 2 (Osteopenia); 3 (Osteoporosis); 2. Sens (sensibility); Spec (specificity); PV+ (positive predictive value); PV- (negative predictive value); 3. AT (the whole talus); ST (the subtalar region of calcaneus); CC (the cavum calcanei region).

region of calcaneus might represent a non invasive screening investigation to identify those subjects for whom a further bone mineral density assessment, by X-ray techniques, is indicated. Indeed, for example, if this quantification identifies an individual as a not normal subject, there will be a probability of about 94% that the individual really will be an osteopenic or osteoporotic subject.
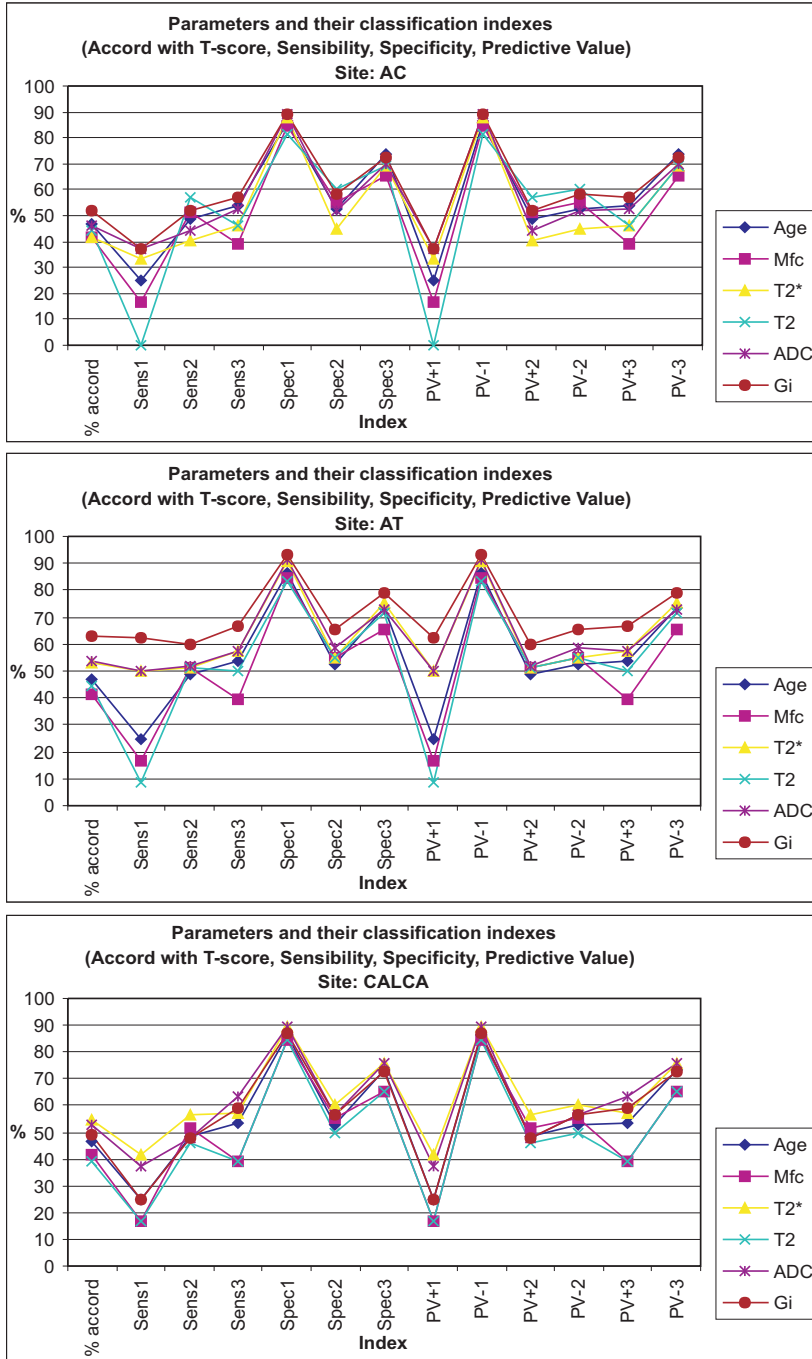
Figure 7.1: For AC, AT and $CALCA$ regions, the classification indexes of Age, Mfc, $T_2^\star$, T_2, ADC and G_i parameters are reported: the accord percentage between the two kinds of classifications (% *accord*) and, for every group, the sensibility (*Sens*), the specificity (*Spec*) and the positive (*PV+1*) and negative (*PV-1*) predictive value of the classification method to test.
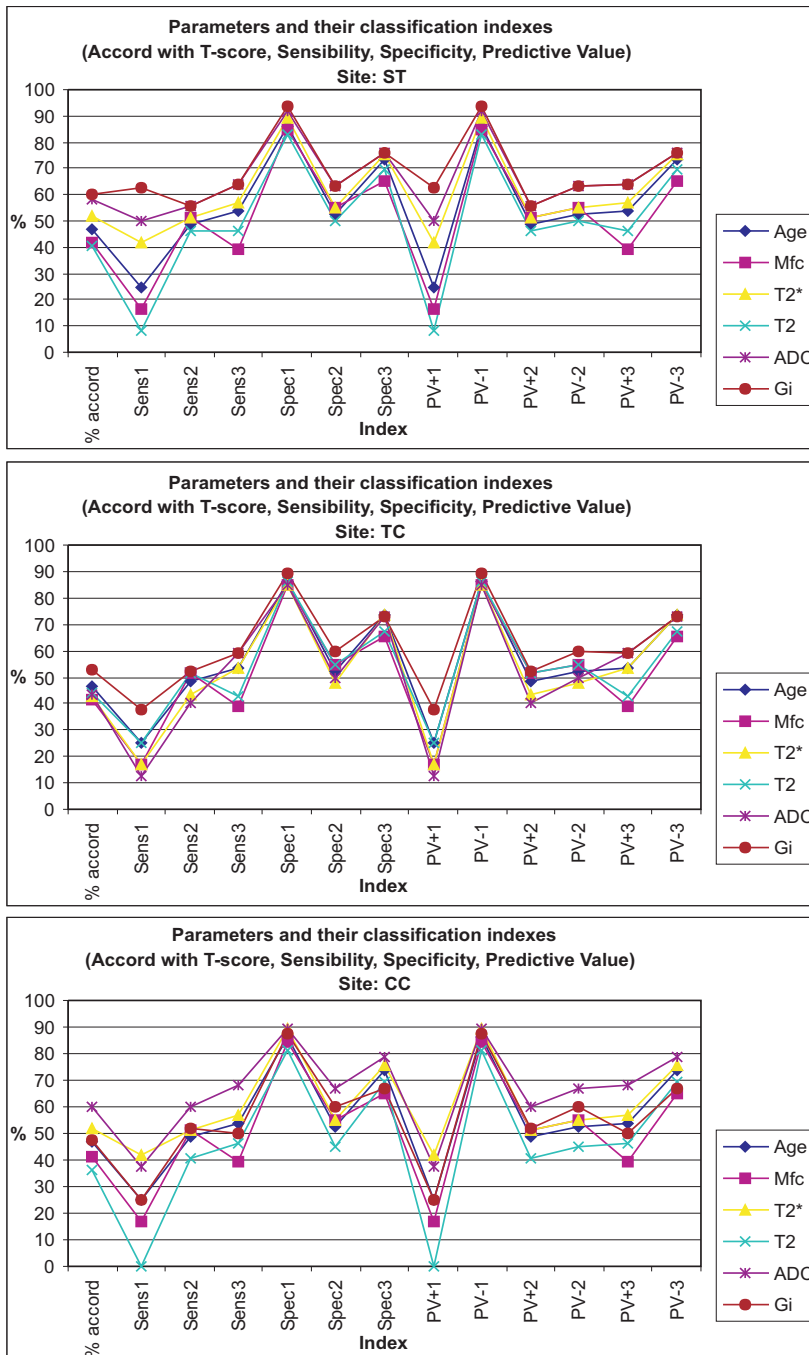
Figure 7.2: For *ST*, *TC* and *CC* regions, the classification indexes of *Age*, *Mfc*, $T_2^\star$, T_2, *ADC* and G_i parameters are reported: the accord percentage between the two kinds of classifications (% *accord*) and, for every group, the sensibility (*Sens*), the specificity (*Spec*) and the positive (*PV+1*) and negative (*PV-1*) predictive value of the classification method to test.

Conclusions

In the present work, the whole experimental results are organized into three chapters, corresponding to three connected research lines, and into a last chapter of analysis and comparison of the results obtained in the first three chapters. This study used quantitative MR techniques at 3T to investigate spongy bone tissue of postmenopausal women in different heel locations: the whole calcaneus ($CALCA$), the whole talus (AT), the talar region close to calcaneus AC, the subtalar region of calcaneus ST, the tuber calcanei region TC and the cavum calcanei region CC. The choice of the heel was mainly due to three reasons: the established correlation between vertebral body fracture and poor trabecular bone density in calcaneus spongy bone, the high heterogeneity of the trabecular bone network in calcaneus and talus and the negligible problems linked to claustrophobic symptoms.

The first chapter gives information about the marrow fat content in calcaneus, by means of ^{1}H Magnetic Resonance Spectroscopy measures; Mfc ranges in a small gap (from about 80% to 94%) that hampers to point out the probable skill of Mfc to detect bone density changes. Moreover, in this situation it's very hard to discriminate the little compensatory filling of the inter-trabecular spaces created by osteoporosis with fatty marrow, from the high marrow fat content of calcaneus.

The results regarding marrow water molecular diffusion analysis, reported in the second chapter, show that the mean ADC values of the three bone density groups (normal, osteopenia and osteoporosis) increase as bone density decreases but these differences are statistically significant between the three groups only in subtalar region of calcaneus. These mean ADC values are one order of magnitude lower than those reported in previous studies analyzing vertebrae; this difference is

due to higher marrow fat content in calcaneus than in vertebra, which restricts the water molecular diffusion.

Our *ADC* results agree with literature findings at low or intermediate marrow fat content (20%-60%), for the statistically significant negative correlation between *ADC* and *T-score* values. Conversely, *ADC* results disagree with literature findings at intermediate-high marrow fat content (45%-80%), for the opposite trend of mean *ADC* values obtained with bone density changes. These different trends can be ascribed to the different marrow fat contents analyzed. Thus, resuming also the literature findings, we can assert that when low or intermediate marrow fat content occurs, water molecules are restricted by the trabecular bone rather than fat cells, thus the change in *ADC* value depends on the trabecular bone architecture. Conversely, when intermediate or high marrow fat content occurs, water molecules are more restricted by the fat cell concentration than by trabecular bone. For very high marrow fat content (80%-94%), as in saturation condition, *ADC* parameter becomes again sensible to the intertrabecular spaces created by trabecular bone density decreasing.

The third chapter gives information about parameters related to NMR Relaxometry ($T_2^\star$ and T_2) and to a new MR parameter (the internal gradient G_i) that we demonstrate to be strictly associated with trabecular bone density and structural rearrangements.

In vitro experiments on calf spongy-bone samples (extracted from a femur head) showed a high positive linear correlation between water G_i and trabecular bone density. Moreover, water *ADC* increases with the decrease in trabecular bone density at low/moderate Mfc. Finally, these *in vitro* experiments demonstrated that in the central zone of each pore there is a higher concentration of fat molecules, due to their hydrophobic nature, characterized by a lower molecular motion than that of water molecules, while water molecules wet the surface of bone pores. The results of *in vivo* experiments show that the mean $T_2^\star$ values (which agree with literature findings) of the three bone density groups increase as bone density decreases and these differences are statistically significant between the three groups in *AT*, *CC* and *CALCA* regions; the mean T_2 values have no trend as bone density decreases, probably due to the poor dependence of the T_2 parameter on the G_i and *ADC* fac-

tors; the mean G_i values of the three bone density groups decrease as bone density decreases and these differences are statistically significant among the three groups only in AT and ST regions.

Mean $T_2^\star$ and G_i values also differ, in each group, among calcaneal regions with different trabecular bone density, thus these parameters give us information on local trabecular bone density. By their values, they moreover locate higher trabecular bone density in the whole talus than in the whole calcaneus and, instead, higher trabecular bone density in ST than in AC region.

Even if ADC and G_i parameters are able to distinguish the three bone density groups, according to WHO criteria, they have a low or moderate significant correlation with $T\text{-}score$ values and this demonstrates that they don't depend only on the bone density but also on other factors bound to the bone quality. Mean ADC values of the three bone density groups overlap when considering their SDs; the mean G_i values almost always have the same behavior, only its values of the normal and osteoporotic groups in ST region don't overlap. Thus, the large standard deviation associated with mean ADC and G_i values assessed in spongy bone tissue from healthy, osteopenic and osteoporotic individuals does not allow the clinical use of ADC and G_i on a single subject basis. Nevertheless, taking into consideration the whole calcaneus and its regions only, in which it was evaluated the Mfc, it is possible to notice that in the graphs of the ADC and G_i values versus Mfc values, the straight lines of the three bone density groups, obtained by the linear regression analysis, tend to a common intermediate ADC and G_i value respectively, at highest Mfc values. Thus, we can assert that the marrow fat content evaluation might improve the diagnostic confidence of osteoporosis, by ADC and G_i assessment of the calcaneal regions in subjects with lowest Mfc values.

Finally, in the last chapter we identify the site-parameter couples which best classify the subjects in the same way of $T\text{-}score$, through the classification indexes. The highest sensibility (62.50%), specificity (93.62%), positive and negative predictive values to detect the normal subjects were obtained with $ST\text{-}G_i$ couple; the highest sensibility (60.00% for osteopenic and 68.18% for osteoporotic subjects), specificity (66.67% for osteopenic and 78.79% for osteoporotic subjects), positive

and negative predictive values to detect the osteopenic and to detect the osteoporotic subjects were obtained with CC-ADC couple.

In all these results, G_i seems to be a potential surrogate marker reflecting different structural features of trabecular bone density. They include not only the solid phase density, but also other characteristics related to spongy bone quality (as expressed by marrow fat content).

Analyzing the future developments of this work, G_i quantification from the subtalar region of calcaneus might represent a non invasive screening investigation to identify those subjects for whom a further bone mineral density assessment, by X-ray techniques, is indicated. Measures of $T_2^\star$, ADC, and G_i from the ST and CC calcaneal regions (as a function of the bone marrow fat content) obtained on large populations, could allow the definition of their cut-off values for normality and osteopenia.

Through analysis of many clinical risk factors, it'll be possible to make new definitions of the osteoporosis general diagnostic categories for women and men, based on the value of a parameter opportunely related to the values of $T_2^\star$, ADC, G_i and Mfc parameters, and also to obtain a graph of the values of this new parameter versus the age, by which it'll be easy to classify the person with respect to the age (New Gold Standard).

This innovative method will be more effective than the current diagnostic methods, because it is a not invasive technique that includes quantitative information about trabecular bone density by MR relaxometry and information on the physiological and functional changes by MR spectroscopy and water diffusion in bone marrow, connected with fracture risk factor.

Bibliography

[1] Prevention and management of osteoporosis. In *WHO Technical Report Series*, 921 (World Health Organization, Geneva, 2003).

[2] J. A. Kanis. Osteoporosis III: diagnosis of osteoporosis and assessment of fracture risk. *Lancet*, **359**, 1929 (2002).

[3] F. W. Wehrli, L. Hilaire, M. F. Seara, B. R. Gomberg, H. K. Song, B. Zemel, L. Loh and P. J. Snyder. Quantitative magnetic resonance imaging in the calcaneus and femur of women with varying degrees of osteopenia and vertebral deformity status. *J Bone Miner Res*, **17**, 2265 (2002).

[4] G. E. Gold, E. Han, J. Stainsby, G. Wrigth, J. Brittain and C. Beaulieu. Musculoskeletal MRI at 3.0 T: Relaxation times and image contrast. *AJR*, **183**, 343 (2004).

[5] F. W. Wehrli, P. K. Saha, B. R. Gomberg, H. K. Song, P. J. Snyder, M. Benito, A. Wright and R. Weening. Role of magnetic resonance for assessing structure and function of trabecular bone. *Topics in Magnetic Resonance Imaging*, **13(5)**, 335 (2002).

[6] T. B. Brismar. MR relaxometry of lumbar spine, hip, and calcaneus in healthy premenopausal women: relationship with dual energy X-ray absorptiometry and quantitative ultrasound. *Eur Radiol*, **10(8)**, 1215 (2000).

[7] C. Kang, M. Paley, R. Ordidge and R. Speller. *In vivo* MRI measurements of bone quality in the calcaneus: a comparison with DXA and ultrasound. *Osteoporosis Int*, **9**, 65 (1999).

[8] A. Gefen and R. Seliktar. Comparison of the trabecular architecture and isostatic stress flow in the human calcaneus. *Medical Engineering & Physics*, **26**, 119 (2004).

[9] Assessment of fracture risk and its application to screening for postmenopausal osteoporosis. In *WHO Technical Report Series*, 843 (World Health Organization, Geneva, 1994).

[10] S. Adamo, P. Carinci, M. Molinaro, G. Siracusa, M. Stefanini and E. Ziparo. *Istologia di V. Monesi*, vol. II. V ed. (Piccin, Italia, 1999).

[11] J. B. Kerr. *Atlas of Functional Histology* (Mosby International Limited, 2001).

[12] P. G. Robey and A. L. Boskey. The biochemistry of bone. In R. Marcus, D. Feldman and J. Kelsey, eds., *Osteoporosis*, 95–183 (Academic Press, San Diego, 1996).

[13] P. Garnero and P. D. Delmas. Biochemical markers of bone turnover, applications for osteoporosis. *Endocrinology and Metabolism Clinics of North America*, **27**, 303 (1998).

[14] J. T. Triffitt. The stem cell of the osteoblast. In J. P. Bilezikian, L. G. Raisz and G. A. Rodan, eds., *Principles of bone biology*, 39–50 (Academic Press, San Diego, 1996).

[15] J. Caverzasio and J. P. Bonjour. Characteristics and regulation of Pi transport in osteogenic cells for bone metabolism. *Kidney International*, **49**, 975 (1996).

[16] P. J. Nijweide. The osteocyte. In J. P. Bilezikian, L. G. Raisz and G. A. Rodan, eds., *Principles of bone biology*, 115–126 (Academic Press, San Diego, 1996).

[17] S. L. Teitelbaum, M. M. Tondravi and F. P. Ross. Osteoclast biology. In R. Marcus, D. Feldman and J. Kelsey, eds., *Osteoporosis*, 61–94 (Academic Press, San Diego, 1996).

[18] R. Baron. Molecular mechanism of bone resorption: therapeutic implications. *Revue du Rhumatisme (English Edition)*, **63**, 633 (1996).

[19] S. C. Manolagas and R. L. Jilka. Bone marrow, cytokines, and bone remodelling: emerging insights into the pathophysiology of osteoporosis. *New England Journal of Medicine*, **332**, 305 (1995).

[20] T. J. Martin and N. Udagawa. Hormonal regulation of osteoclast function. *Trends in Endocrinology and Metabolism*, **9**, 6 (1998).

[21] M. C. Horowitz. Cytokines and estrogen in bone: anti-osteoporotic effects. *Science*, **260**, 626 (1993).

[22] T. Suda. Modulation of osteoclast differentiation and function by the new members of the tumor necrosis factor receptor and ligand families. *Endocrine Reviews*, **20**, 345 (1999).

[23] E. Canalis. Skeletal growth factors. In R. Marcus, D. Feldman and J. Kelsey, eds., *Osteoporosis*, 261–279 (Academic Press, San Diego, 1996).

[24] G. A. Rodan. Coupling of bone resorption and formation during bone remodelling. In R. Marcus, D. Feldman and J. Kelsey, eds., *Osteoporosis*, 289–299 (Academic Press, San Diego, 1996).

[25] A. E. Broadus. Mineral balance and homeostasis. In M. J. Favus, ed., *Primer on the metabolic bone disease and disorders of mineral metabolism*, 3rd ed., 57–63 (Lippincott-Raven, Philadelphia, 1996).

[26] S. Christakos. Vitamin d gene regulation. In J. P. Bilezikian, L. G. Raisz and G. A. Rodan, eds., *Principles of bone biology*, 435–446 (Academic Press, San Diego, 1996).

[27] H. M. Kronenberg. Parathyroid hormone: mechanism of action. In M. J. Favus, ed., *Primer on the metabolic bone disease and disorders of mineral metabolism*, 3rd ed., 68–70 (Lippincott-Raven, Philadelphia, 1996).

[28] W. S. Snyder, M. H. Cook, E. S. Nasset and al. Report of the task group on reference man. *Pergamon*, 79 (1974).

[29] J. L. Emery and G. F. Follett. Regression of bone-marrow haemopoiesis from the terminal digits in the foetus and infant. *Br J Haematol*, **10**, 485 (1964).

[30] M. Hashimoto. The distribution of active marrow in the bones of normal adults. *Kyushu J Med Sci*, **11**, 103 (1960).

[31] J. P. Bonjour and R. Rizzoli. Bone acquisition in adolescence. In R. Marcus, D. Feldman and J. Kelsey, eds., *Osteoporosis*, 465–476 (Academic Press, San Diego, 1996).

[32] J. P. Bonjour. Peak bone mass. *Osteoporosis International*, **1**, 7 (1994).

[33] P. N. Sambrook. Genetic determinants of bone mass. In R. Marcus, D. Feldman and J. Kelsey, eds., *Osteoporosis*, 477–482 (Academic Press, San Diego, 1996).

[34] J. P. Bourguignon. Delayed puberty and hypogonadism. In J. Bertrand, R. Rappaport and P. C. Sizonenko, eds., *Pediatric endocrinology, physiology, pathophysiology, and clinical aspects*, 404–429 (Williams and Wilkins, Baltimore, 1993).

[35] H. Heath. Primary hyperparathyroidism, hyperparathyroid bone disease, and osteoporosis. In R. Marcus, D. Feldman and J. Kelsey, eds., *Osteoporosis*, 885–897 (Academic Press, San Diego, 1996).

[36] P. J. Meunier. Calcium, vitamin D and vitamin K in the prevention of fractures due to osteoporosis. *Osteoporosis International*, **9(suppl. 2)**, 48 (1999).

[37] J. P. Bonjour. Protein intake, IGF-1 and osteoporosis. *Osteoporosis International*, **7(suppl. 3)**, 36 (1997).

[38] W. E. Bacon. International comparison of hip fracture rates in 1988-1989. *Osteoporosis International*, **6**, 69 (1996).

[39] M. L. Bouxsein, E. R. Myers and W. C. Hayes. Biomechanics of age-related fractures. In R. Marcus, D. Feldman and J. Kelsey, eds., *Osteoporosis*, 373–393 (Academic Press, San Diego, 1996).

[40] M. T. Cuddihy. Forearm fractures as predictors of subsequent osteoporotic fractures. *Osteoporosis International*, **9**, 469 (1999).

[41] G. S. Cooper. Genetic studies of osteoporosis: what have we learned. *Journal of Bone and Mineral Research*, **14**, 1646 (1999).

[42] E. Seeman. The effects of tobacco and alcohol use on bone. In R. Marcus, D. Feldman and J. Kelsey, eds., *Osteoporosis*, 577–597 (Academic Press, San Diego, 1996).

[43] L. A. Lehmann, R. E. Alvarez, A. Macovski, W. R. Brody, N. J. Pelc, S. J. Riederer and al. Generalized image combinations in dual KVP digital radiography. *Med Phys*, **8**, 659 (1981).

[44] G. M. Blake, J. F. Griffith, D. K. W. Yeung, P. C. Leung and I. Fogelman. Effect of increasing vertebral marrow fat content on BMD measurement, T-score status and fracture risk prediction by DXA. *Bone*, **44**, 459 (2009).

[45] C. F. Nijeh and G. M. Blake. Calcaneal quantitative ultrasound devices: water-coupled. In C. F. Nijeh, D. Hans, T. Fuerst, C. C. Gluer and H. K. Genant, eds., *Quantitative ultrasound: assessment of osteoporosis and bone status*, 109–124 (Martin Dunitz, London, 1999).

[46] C. E. D. DeLaet. Bone density and risk of hip fracture in men and women: cross sectional analysis. *British Medical Journal*, **315**, 221 (1997).

[47] K. Engelke, J. E. Adams, G. Armbrecht, P. Augat, C. E. Bogado, M. L. Bouxsein, D. Felsenberg, M. Ito, S. Prevrhal, D. B. Hans and E. M. Lewiecki. Clinical use of quantitative computed tomography and peripheral quantitative computed tomography in the management of osteoporosis in adults: The 2007 ISCD official positions. *Journal of Clinical Densitometry: Assessment of Skeletal Health*, **11**, 123 (2008).

[48] D. Marshall, O. Johnell and H. Wedel. Meta-analysis of how well measures of bone mineral density predict occurrence of osteoporotic fractures. *British Medical Journal*, **312**, 1254 (1996).

[49] R. M. Bracewell. *The Fourier Transform and its Applications* (McGraw-Hill, New York, 1965).

[50] P. T. Callaghan. *Principles Of Nuclear Magnetic Resonance Microscopy* (Clarendon Press, Oxford, 1991).

[51] K. Huang. *Meccanica Statistica* (Zanichelli, 2001).

[52] J. Crank. *The Mathematics of Diffusion* (Clarendon Press, Oxford, 1957).

[53] D. L. Bihan. *Diffusion and Perfusion Magnetic Resonance Imaging* (Raven Press, 1995).

[54] S. N. Hwang and F. W. Wehrli. The calculation of the susceptibility-induced magnetic field from 3D NMR images with applications to trabecular bone. *Journal of Magnetic Resonance*, **109 (B)**, 126 (1995).

[55] A. Dmitriy, D. A. Yablonskiy and E. M. Haacke. Theory of NMR signal behavior in magnetically inhomogeneous tissues: The static dephasing regime. *Magn Reson Med*, **32**, 749 (1994).

[56] E. L. Hahn. Spin echoes. *Phys Rev*, **80**, 580 (1950).

[57] T. C. Farrar and E. D. Becker. *Pulse and Fourier Transform NMR. Introduction to Theory and Methods* (Academic Press, London, 1971).

[58] F. Parhami, A. Garfinkel and L. L. Demer. Role of lipids in osteoporosis. *Arterioscler Thromb Vasc Biol*, **20**, 2346 (2000).

[59] Y. Chi and R. K. Gupta. Alterations in membrane fatty acid unsaturation and chain length in hypertension as observed by ^{1}H NMR spectroscopy. *Am J Hypertens*, **11**, 340 (1998).

[60] C. Noula, P. Bonzom, A. Brown, W. A. Gibbons, J. Martin and A. Nicolaou. ^{1}H-NMR lipid profiles of human blood platelets; links with coronary artery disease. *Biochim Biophys Acta*, **1487**, 15 (2000).

[61] P. von der Recke, M. A. Hansen and C. Hassager. The association between low bone mass at the menopause and cardiovascular mortality. *Am J Med*, **106**, 273 (1999).

[62] S. I. McFarlane, R. Muniyappa, J. J. Shin, G. Bahtiyar and J. R. Sowers. Osteoporosis and cardiovascular disease: brittle bones and boned arteries, is there a link? *Endocrine*, **23**, 1 (2004).

[63] J. M. Gimble, C. E. Robinson, X. Wu and K. A. Kelly. The function of adipocytes in the bone marrow stroma: an update. *Bone*, **19**, 421 (1996).

[64] S. Verma, J. H. Rajaratnam, J. Denton, J. A. Hoyland and R. J. Byers. Adipocytic proportion of bone marrow is inversely related to bone formation in osteoporosis. *J Clin Pathol*, **55**, 693 (2002).

[65] Y. Miyake, K. Yokomizo and N. Matsuzaki. Determination of unsaturated fatty acid composition by high-resolution nuclear magnetic resonance spectroscopy. *J Am Oil Chem Soc*, **75**, 1091 (1998).

[66] M. D. Guillen and A. Ruiz. ^{1}H nuclear magnetic resonance as a fast tool for determining the composition of acyl chains in acylglycerol mixtures. *Eur J Lipid Sci Technol*, **105**, 502 (2003).

[67] M. D. Guillen and A. Ruiz. Rapid simultaneous determination by proton NMR of unsaturation and composition of acyl groups in vegetable oils. *Eur J Lipid Sci Technol*, **105**, 688 (2003).

[68] D. K. W. Yeung, J. F. Griffith, G. E. Antonio, F. K. H. Lee, J. Woo and P. C. Leung. Osteoporosis is associated with increased marrow fat content and decreased marrow fat unsaturation: a proton MR spectroscopic study. *JMRI*, **22**, 279 (2005).

[69] F. W. Wehrli, J. A. Hopkins and al. Cross-sectional study of osteopenia with quantitative MR imaging and bone densitometry. *Radiology*, **217**, 527 (2000).

[70] D. Schellinger, C. S. Lin, J. Lim, H. G. Hatipoglu, J. C. Pezzullo and A. J. Singer. Bone marrow fat and bone mineral density on proton MR spectroscopy and dual-energy X-ray absorptiometry. *AJR*, **183**, 1761 (2004).

[71] G. F. Griffith and al. Vertebral marrow fat content and diffusion and perfusion indexes in women with varying bone density: MR evaluation. *Radiology*, **241**, 831 (2006).

[72] G. P. Liney, C. P. Bernard, D. J. Manton, L. W. Turnbill and C. M. Langton. Age, gender and skeletal variation in bone marrow

composition: a preliminary study at 3.0 Tesla. *J Magn Reson Imaging*, **26**, 787 (2007).

[73] D. Schellinger, C. S. Lin, H. G. Hatipoglu and D. Fertikh. Potential value of vertebral proton MR spectroscopy in determining bone weakness. *AJNR*, **22**, 1620 (2001).

[74] T. Ikeda and K. Sakurai. Influence of bone marrow fat on the determination of bone mineral content by QCT. *Nippon Igaku Hoshasen Gakkai Zasshi*, **54**, 886 (1994).

[75] M. S. Dunnill, J. A. Anderson and R. Whitehead. Quantitative histolological studies on age changes in bone. *J Pathol Bacteriol*, **94**, 275 (1967).

[76] P. Lang, P. Steiger, K. Faulkner, C. Gluer and H. K. Genant. Osteoporosis: current techniques and recent developments in quantitative bone densitometry. *Radiol Clin N Am*, **29**, 49 (1991).

[77] M. Funke, L. Kopka, R. Vosshenrich and al. Broadband ultrasound attenuation on the diagnosis of osteoporosis: correlation with osteodensitometry and fracture. *Radiology*, **194**, 77 (1995).

[78] G. C. Dooms, M. R. Fisher, H. Hricak, M. Richardson, L. E. Crooks and H. K. Genant. Bone marrow imaging: magnetic resonance studies related to age and sex. *Radiology*, **155**, 429 (1985).

[79] I. Pykett and B. R. Rosen. Nuclear magnetic resonance: in vivo proton chemical shift imaging. *Radiology*, **149**, 197 (1983).

[80] B. L. Riggs, H. W. Wahner, L. J. I. Melton, L. S. Richelson, H. L. Judd and K. P. Offord. Rates of bone loss in the appendicular and axial skeleton of women: evidence of substantial vertebral bone loss before menopause. *J Clin Invest*, **77**, 1487 (1986).

[81] B. L. Riggs and L. J. Melton. Involutional osteoporosis. *N Engl J Med*, **314**, 1676 (1986).

[82] L. Kazarian and G. Graves. Compressive strength characteristics of the human vertebral column. *Spine*, **2**, 1 (1977).

[83] M. E. Nuttall and J. M. Gimble. Is there a therapeutic opportunity to either prevent or treat osteopenic disorders by inhibiting marrow adipogenesis? *Bone*, **27**, 177 (2000).

[84] S. W. Provencher. Magnetic resonance in medicine. *Bone*, **30**, 672 (1993).

[85] J. H. Chan, W. C. Peh, E. Y. Tsui and al. Acute vertebral body compression fractures: discrimination between benign and malignant causes using apparent diffusion coefficients. *Br J Radiol*, **75**, 207 (2002).

[86] A. M. Herneth, M. O. Philipp, J. Naude and al. Vertebral metastases: assessment with apparent diffusion coefficient. *Radiology*, **225**, 889 (2002).

[87] D. K. W. Yeung, S. Y. S. Wong, J. F. Griffith and E. M. C. Lau. Bone marrow diffusion in osteoporosis: evaluation with quantitative MR diffusion imaging. *JMRI*, **19**, 222 (2004).

[88] G. F. Griffith, D. K. Yeung, G. E. Antonio and al. Vertebral bone mineral density, marrow perfusion, and fat content in healthy men and men with osteoporosis: dynamic contrast-enhanced MR imaging and MR spectroscopy. *Radiology*, **236**, 945 (2005).

[89] H. G. Hatipoglu, A. Selvi, D. Ciliz and E. Yuksel. Quantitative and diffusion MR imaging as a new method to assess osteoporosis. *Am J Neuroradiol*, **28**, 1934 (2007).

[90] Y. Ueda, T. Miyati, N. Ohno, Y. Motono, M. Hara, Y. Shibamoto, H. Kasai, H. Kawamitsu and K. Matsubara. Apparent diffusion coefficient and fractional anisotropy in the vertebral bone marrow. *Journal of Magnetic Resonance Imaging*, **31**, 632 (2010).

[91] X. Ouyang and al. *Analysis of high resolution* MRI *images of calcaneus: gray-level thresholding and trabecular quantification* (Society of Magnetic Resonance Third Scientific Meeting, Nice, 1995).

[92] J. C. Lin, M. Amling, D. C. Newitt, K. Selby, S. K. Srivastav, G. Delling, H. K. Genant and S. Majumdar. Heterogeneity of tra-

becular bone structure in the calcaneus using magnetic resonance imaging. *Osteoporosis International*, **8**, 16 (1998).

[93] D. Ballon, J. Dyke, L. H. Schwartz and al. Bone marrow segmentation in leukemia using diffusion and T_2 weighted echo planar magnetic resonance imaging. *NMR Biomed*, **13**, 321 (2000).

[94] F. W. Wehrli, H. K. Song, P. K. Saha and A. Wright. Quantitative MRI for the assessment of bone structure and function. *NMR Biomed*, **19**, 731 (2006).

[95] S. Majumdar, D. Thomasson, A. Shimakawa and H. K. Genant. Quantitation of the susceptibility difference between trabecular bone and bone marrow: experimental studies. *Magn Reson Med*, **22**, 111 (1991).

[96] H. Chung, F. W. Wehrli, J. L. Williams and S. D. Kugelmass. Relationship between NMR transverse relaxation, trabecular bone architecture, and strength. *Proc Natl Acad Sci USA*, **90**, 10250 (1993).

[97] F. W. Wehrli, J. C. Ford, M. Attie, H. Kressel and F. Kaplan. Trabecular structure: preliminary application of MR interferometry. *Radiology*, **179**, 615 (1991).

[98] T. M. Link, S. Majumdar, P. Augat and al. Proximal femur: Assessment of osteoporosis with $T_2^\star$ decay characteristics at MR imaging. *Radiology*, **209**, 531 (1998).

[99] S. Capuani, M. Rebuzzi, F. Fasano, G. E. Hagberg, M. D. Mario, V. Vinicola and B. Maraviglia. $T_2^\star$ relaxometry and ^{1}H-MRS at 3T applied to healthy and osteoporotic subjects: preliminary data supporting a new procedure to evaluate bone fracture risk. *Proc Intl Soc Mag Reson Med*, **16**, 2534 (2008).

[100] H. K. Hussain, T. L. Chenevert, F. J. Londy, V. Gulani, S. D. Swanson, B. J. McKenna, H. D. Appelman, S. Adusumilli, J. K. Greenson and H. S. Conjeevaram. Hepatic fat fraction: MR imaging for quantitative measurement and displayearly experience. *Radiology*, **237**, 1048 (2005).

[101] D. P. O'Regan, M. F. Callaghan, M. Wylezinska-Arridge, J. Fitz-patrick, R. P. Naoumova, J. V. Hajnal and S. A. Schmitz. Liver fat content and $T_2^\star$: simultaneous measurement by using breath-hold multiecho MR imaging at 3.0 T feasibility. *Radiology*, **247**, 550 (2008).

[102] J. Weis, L. Johansson, F. Ortiz-Nieto and H. Ahlstrom. Assessment of lipids in skeletal muscle by high-resolution spectroscopic imaging using fat as the internal standard: comparison with water referenced spectroscopy. *Magn Reson Med*, **59**, 1259 (2008).

[103] J. Ren, I. Dimitrov, A. D. Sherry and C. D. Malloy. Composition of adipose tissue and marrow fat in humans by ^{1}H NMR at 7 Tesla. *J Lipid Res*, **49**, 2055 (2008).

[104] A. T. Watson and C. T. P. Chang. Characterizing porous media with NMR methods. *Prog Nucl Magn Reson Spectrosc*, **31**, 343 (1997).

[105] R. C. Wilson and Hurlimann. Relationship between susceptibility induced field inhomogeneities, restricted diffusion, and relaxation in sedimentary rocks. *J Magn Reson*, **183**, 1 (2006).

[106] J. Kuntz, P. Palmas, V. Level and D. Canet. Restricted diffusion and exchange of water in porous media: average structure determination and size distribution resolved from the effect of local field gradient on the proton NMR spectrum. *J Magn Reson*, **191**, 239 (2008).

[107] S. Capuani, C. Rossi, M. Alesiani and B. Maraviglia. Diffusion tensor imaging to study anisotropy in a particular porous system: the trabecular bone network. *Solid State Nucl Magn Reson*, **28**, 266 (2005).

[108] S. N. Hwang and F. W. Wehrli. The calculation of the susceptibility-induced magnetic field from 3D NMR images with applications to trabecular bone. *J Magn Reson*, **109**, 126 (1995).

[109] P. Mertens, J. Machann, B. Mueller-Bierl, G. Steidle, M. E. Belle-mann and F. Schick. Magnetic field distribution in the presence of

paramagnetic plates in magnetic resonance imaging: a combined numerical and experimental study. *Med Phys*, **35**, 1777 (2008).

[110] E. E. Sigmund, H. Cho, P. Chen, S. Byrnes, Y. Q. Song, X. E. Guo and T. R. Brown. Diffusion-based MR methods for bone structure and evolution. *Magn Reson Med*, **59**, 28 (2008).

[111] E. E. Sigmund, H. Cho and Y. Q. Song. High-resolution MRI of internal field diffusion-weighting in trabecular bone. *NMR Biomed*, **22**, 436 (2009).

[112] S. D. Santis, M. Rebuzzi, G. D. Pietro, F. Fasano, B. Maraviglia and S. Capuani. *In vitro* and *in vivo* MR evaluation of internal gradient to assess trabecular bone density. *Phys Med Biol*, **55**, 5767 (2010).

[113] E. Chabanova, H. E. Johnsen, L. Meldgaard-Knudsen, L. Larsen, V. Logager, S. Yingru and H. S. Thomsen. Magnetic resonace investigation of bone marrow following priming and stem cell mobilization. *J Magn Reson Imaging*, **24**, 1364 (2006).

[114] H. H. Ong, A. C. Wright, S. L. Wehrli, C. E. Joses and F. W. Wehrli. Is bone marrow diffusion too slow or too fast for susceptibility-based methods to assess trabecular bone architecture? *Proc Intl Soc Magn Reson Med*, **17**, 1941 (2009).

[115] L. S. Szczepaniak, R. L. Dobbins, D. T. Stein and J. D. McGarry. Bulk magnetic susceptibility effects on the assessment of intra-ad extramyocellular lipids *in vivo*. *Magn Reson Med*, **47**, 607 (2002).

[116] S. N. Hwang and F. W. Wehrli. Experimental evaluation of a surface charge method for computing the induced magnetic field in trabecular bone. *J Magn Reson*, **139**, 35 (1999).

[117] E. Lammentausta, T. S. Silvast, J. Narvainen, J. S. Jurvelin, M. T. Nieminen and O. H. J. Grohn. T_2, Carr-Purcell T_2 of fat and water as surrogate markers of trabecular bone structure. *Phys Med Biol*, **53**, 543 (2008).

Acknowledgements